FEDERAL UNIVERSITY OF SÃO CARLOS
EXACT AND TECHNOLOGY SCIENCES CENTER
GRADUATE PROGRAM IN CHEMICAL ENGINEERING

KAÍQUE SOUZA GONÇALVES CORDEIRO OLIVEIRA

High-performance chloride-doped polyaniline activated carbon modified with Pluronic™ template for electrochemical desalination

Carvão ativado de alto desempenho de polianilina dopada com cloreto modificada com template Pluronic™ para dessalinização eletroquímica

SÃO CARLOS

2023

KAÍQUE SOUZA GONÇALVES CORDEIRO OLIVEIRA

High-performance chloride-doped polyaniline activated carbon modified with Pluronic^{TM} template for electrochemical desalination

Carvão ativado de alto desempenho de polianilina dopada com cloreto modificada com template Pluronic^{TM} para dessalinização eletroquímica

Ph.D. thesis presented to the Graduation Program in Chemical Engineering of the Federal University of São Carlos as part of the requirements to obtain the title of Ph.D. in Chemical Engineering, in the field of Research and Development of Chemical Processes.

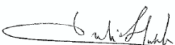Advisor: Prof. Dr. Luís Augusto Martins Ruotolo

SÃO CARLOS

2023

Folha de Aprovação

Defesa de Tese de Doutorado do candidato Kaíque Souza Gonçalves Cordeiro Oliveira, realizada em 15/02/2023.

Comissão Julgadora:

Prof. Dr. Luis Augusto Martins Ruotolo (UFSCar)

Prof. Dr. Julio José Lado Garrido (IMDEA Energía)

Prof. Dr. Ricardo Francisco Brocenschi (UFU)

Profa. Dra. Alessandra Pereira da Silva (UNIFESP)

Profa. Dra. Kamilla Malverdi Barcelos (UFES)

O Relatório de Defesa assinado pelos membros da Comissão Julgadora encontra-se arquivado junto ao Programa de Pós-Graduação em Engenharia Química.

I dedicate this thesis to God for giving me strength and support, to my parents and friends for their encouragement and to Renato for always supporting me at critical times. You were the pillar of this achievement.

ACKNOWLEDGEMENTS

(qualification and defense), and Dr. Kamilla Malverdi Barcelos (qualification and defense) for accepting the invitation and dedicating their time to contribute to the improvement of this work.

I thank also to all who directly or indirectly assisted me to complete this work. Thank you very much.

"I must endure the presence of two or three caterpillars
if I wish to become acquainted with the butterflies"
The Little Prince (Saint-Exupéry, 1943)

ABSTRACT

HIGH-PERFORMANCE CHLORIDE-DOPED POLYANILINE ACTIVATED CARBON MODIFIED WITH PLURONIC^{TM} TEMPLATE FOR ELECTROCHEMICAL DESALINATION - Activated carbon obtained from chloride-doped polyaniline (PAC/Cl) is an attractive material for brackish water desalination using capacitive deionization (CDI), due to its easy synthesis, low cost, and fast electrosorption kinetics. However, its low content of surface oxygen groups (SOGs) suppresses the salt adsorption capacity (*SAC*), despite high specific surface area. In this thesis, different strategies to improve the *SAC* and boost the kinetics of PAC/Cl electrodes were investigated by modifying the synthesis procedure. Firstly, the use of Pluronic^{TM} F127 (PLR) as a template (CTAK electrode) allowed modification of the structure and textural properties of the carbonized and activated samples, increasing the SOG content by 26% (from 4.2 to 5.3 at.%), compared to the electrode prepared in the absence of PLR (CTAK*). Consequently, the electrode hydrophobicity was reduced by 2.1-fold (from 87.4 to 40.9º) and the desalination performance was enhanced, especially using an asymmetric electrode configuration (*SAC* enhancement from 11.4 to 21.0 mg g^{-1}). Despite the slower kinetics observed using CTAK, compared to CTAK*, when the *SAC* and electrosorption/desorption kinetics were considered together, CTAK outperformed CTAK* by ~1.7-fold (from 932 to 1560 mg g^{-1} day^{-1}), in both symmetric and asymmetric configurations. As a second approach, the use of PLR combined with hydrothermal carbonization, despite leading to a 3D hierarchical framework, hindered the access to the pores, negatively impacting the process kinetics. The results showed that the use of PLR-modified PAC/Cl is a simple and effective strategy for obtaining low-cost activated carbons with distinct surface chemistry that can improve desalination performance.

Keywords: Capacitive deionization; Polyaniline activated carbon; Surface functional groups; Pluronic^{TM} templating agent; Hydrothermal carbonization.

RESUMO

CARVÃO ATIVADO DE ALTO DESEMPENHO DE POLIANILINA DOPADA COM CLORETO, MODIFICADA COM TEMPLATE PLURONIC^TM, PARA DESSALINIZAÇÃO ELETROQUÍMICA - O carvão ativado obtido a partir de polianilina dopada com cloreto (PAC/Cl) é um material atrativo para a dessalinização de água salobra via deionização capacitiva (DIC) devido à sua fácil síntese, baixo custo e rápida cinética de eletrossorção. No entanto, seu baixo teor de grupos superficiais de oxigênio (GSOs) reduz sua capacidade de adsorção de sal (CAS), apesar da sua alta área superficial específica. Nesta tese, diferentes estratégias para melhorar a CAS e aumentar a cinética de dessalinização pelos eletrodos de PAC/Cl foram investigadas modificando-se o procedimento de síntese. Primeiramente, o uso de Pluronic^TM F127 (PLR) como direcionador (eletrodo CTAK) permitiu modificar a estrutura e as propriedades texturais das amostras carbonizadas e ativadas, aumentando o teor de GSO em 26% (de 4,2 para 5,3 %at.), em comparação ao eletrodo preparado na ausência de PLR (CTAK*). Como consequência, a hidrofobicidade do eletrodo foi reduzida em 2,1 vezes (o ângulo de contato foi reduzido de 87,4 para 40,9º), melhorando a dessalinização, especialmente quando uma configuração assimétrica de eletrodo foi utilizada (CAS aumentou de 11,4 para 21,0 mg g^{-1}). Apesar da cinética mais lenta observada usando CTAK, em comparação com CTAK*, quando a CAS e a cinética de eletrossorção/dessorção foram consideradas simultaneamente, o CTAK superou o CTAK* em ~1,7 vezes (de 932 para 1560 mg g^{-1} dia^{-1}), em ambas as configurações simétrica e assimétrica. Em uma segunda abordagem, o uso de PLR combinado com carbonização hidrotérmica, apesar de levar a uma estrutura tridimensional hierárquica, dificultou o acesso aos poros, impactando negativamente a cinética do processo. Os resultados mostraram que o uso de PAC/Cl modificado com PLR é uma estratégia simples e eficaz para a obtenção de carvões ativados de baixo custo e com química de superfície apropriada, que proporciona a melhoria do processo de dessalinização.

LIST OF FIGURES

LIST OF TABLES

ABBREVIATIONS

AC	Activated carbon
AEM	Anion-exchange membrane
ATR-FTIR	Fourier Transform Infrared spectroscopy coupled with Attenuated Total Reflection detection
BBOT	2,5-Bis(5-ter-butyl-benzoxazol-2-yl)thiophene
CDI	Capacitive deionization (DIC in Portuguese)
CE	Counter electrode
CEM	Cation-exchange membrane
CHNS	Elemental analysis
CT	Thermally carbonized sample, followed by thermal treatment
CT*	Thermally carbonized sample without Pluronic, followed by thermal treatment
CTAK	Thermally carbonized sample, followed by activation using KOH
CTAK*	Thermally carbonized sample without Pluronic, followed by activation using KOH
CV	Cyclic voltammetry
ED	Electrodialysis
EDL	Electrical double layer
EIS	Electrochemical impedance spectroscopy
FDI	Faradaic deionization
GCS	Gouy-Chapman-Stern model
HRTEM	High-resolution transmission electron microscopy
HT	Hydrothermally carbonized sample, followed by thermal treatment
HTAC	Hydrothermally carbonized sample, followed by thermal treatment and activation using CO_2
HTACK	Hydrothermally carbonized sample, followed by thermal treatment and activation using CO_2 and KOH
HTAK	Hydrothermally carbonized sample, followed by thermal treatment and activation using KOH
IEM	Ion-exchange membrane
IUPAC	International Union of Pure and Applied Chemistry

MCDI	Membrane capacitive deionization
MED	Multiple-effect distillation
MSF	Multi-stage flash distillation
NMP	*n*-Methylpyrrolidone
PAC/Cl	Chloride-doped polyaniline activated carbon
PAC/PTS	*p*-Toluenesulfonic-doped polyaniline activated carbon
PAC/S	Sulfate-doped polyaniline activated carbon
PAni	Polyaniline
PEO	Polyethylene oxide
PGAC	Polyglycerol activated carbon
pH	Hydrogen potential
PLR	Pluronic^tm F127
PPO	Polypropylene oxide
PPy	Polypyrrole
PSD	Pore size distribution
PVDF	Polyvinylidene fluoride
RO	Reverse osmosis
SDG	Sustainable development goal
SOG	Surface oxygen group (GSO in Portuguese
UNESCO	United nations educational scientific and cultural organization
WE	Working electrode
XDR	X-ray diffraction
XPS	X-ray photoelectron spectroscopy

SYMBOLS

Latin letters

$\%V_{mes}$	Percentage of mesopore volume	%
$ASAR$	Average salt adsorption rate	mg g^{-1} s^{-1}
C	Capacitance	F
C_0	Initial salt concentration	mg L^{-1}
C_{min}	Minimum capacitance	F
C_S	Specific capacitance	F g^{-1}
C_t or C	Salt concentration at time t	mg L^{-1}
d_{50}	Average pore diameter	nm
E_{cell}	Cell potential in the electrosorption step	V
E_{pzc}	Potential of zero-charge	V vs reference electrode
F	Faraday constant	A s mol^{-1}
I	Electric current	A
I_D/I_G	Raman peak intensity ratio	-
k_d	Desorption rate constant	s^{-1}
k_e	Electrosorption rate constant	s^{-1}
m	Mass of activated carbon in the working electrode	g
m_E	Total mass of the active material in both electrodes	g
M_{NaCl}	Molecular weight of nacl	mg mol^{-1}
m_{rem}	Mass of ions removed from the solution	mg
$mSAC$	Maximum value of SAC	mg g^{-1}
m_{sr}	Deriving the amount of salt removed	g
N_{cycles}	Number of cycles	-
OSR	Optimized salt removal	mg g^{-1} day^{-1}
P/P_0	Relative pressure	-
Q_E	Charge efficiency	%
R_{CT}	Charge-transfer resistance	Ω
R_{Ω}	Ohmic resistance	Ω
SAC	Salt adsorption capacity (CAS in Portuguese)	mg g^{-1}
SDC	Salt desorption concentration	mg g^{-1}

SSA	Specific surface area	$m^2\ g^{-1}$
SSA_{BET}	Specific surface area calculated by Brunauer-Emmett-Teller equation	$m^2\ g^{-1}$
t	Time	s
t_d	Desorption time	s
t_e	Electrosorption time	s
t_{op}	Specified operational time	day
V	Electrolyte volume	L
V_{mes}	Mesopore volume	$cm^3\ g^{-1}$
V_{mic}	Micropore volume	$cm^3\ g^{-1}$
V_T	Total pore volume	$cm^3\ g^{-1}$
Y_{Ch}	Chemical activation yield	g AC/g char
Y_{HC}	Hydrothermal carbonization yield	g char/g PAni
Y_O	Overall yield	g AC/g PAni
Y_{PAni}	Polymerization yield	g PAni/mL aniline
Y_{Ph}	Physical activation yield	g AC/g char
Y_{TC}	Thermal carbonization yield	g char/g PAni
z	Ion valence	-
Z''	Imaginary component of the impedance spectrum	Ω
Z'	Real component of the impedance spectrum	Ω

Greek letters

$\Delta\Phi_d$	Diffuse layer potential	V *vs* reference electrode
$\Delta\Phi_{st}$	Stern layer potential	V *vs* reference electrode
η	Specific energy consumption	$J\ mg^{-1}$
θ	Contact angle	°
ν	Scan rate	$V\ s^{-1}$
ω	Angular frequency	Hz

SUMMARY

CHAPTER 1

INTRODUCTION

The worldwide demand for fresh water is rising, as reported by the United Nations [1], requiring new resources to provide it, especially in semiarid regions. Consequently, technologies for the desalination of sea and brackish water are increasing in importance. Capacitive deionization (CDI) is a competitive technology for the desalination of brackish water, due to the lower energy required to remove ions [2,3]. Typically, a low potential (1.2 V) is applied to a pair of carbon electrodes, forcing the ions to move from the solution to the electrodes, where they are stored and form an electric double layer. This behavior, similar to that observed for supercapacitor technology, enables the desalination of water, while storing energy [4,5]. The CDI performance will depend on the textural properties of the carbon material (specific surface area, *SSA*, and pore size distribution, PSD), as well as its surface chemistry [6].

Activated carbons (ACs) obtained from carbonization and activation of polyaniline (PAni) doped with large anions have been reported as promising materials for CDI applications [7–9]. This is due to the high salt adsorption capacity (*SAC*) provided by their surface chemistry and textural properties [10]. In particular, for a membraneless process, the AC obtained from *p*-toluenesulfonic-doped polyaniline (PAC/PTS) displayed a remarkable *SAC* (22.2 mg g^{-1}) after synthesis optimization [11]. On the other hand, the AC derived from chloride-doped polyaniline (PAC/Cl) had poor desalination performance (*SAC* = 5.8 mg g^{-1}), despite having a significantly higher *SSA* (2652 m^2 g^{-1}) [10]. After a thorough investigation of the electrochemical properties and functional surface groups, assessed by X-ray photoelectron spectroscopy (XPS) analysis, it was found that the poor electrosorption capacity of PAC/Cl was mainly due to the low content of surface oxygen groups (SOGs). This evidenced that although high *SSA* is a desirable property for ACs used for CDI, the presence of SOGs, especially certain oxygen groups, is a critical feature for obtaining good desalination performance [10,12,13]. SOGs are expected to improve the electrosorption process, mainly due to increased hydrophilicity [14] and shift of the potential of zero-charge (*E$_{pzc}$*) of the electrode [15].

The desalination rate is also important in determining CDI performance. It has already been shown that ACs presenting fast adsorption/desorption kinetics can eventually remove more ions during a desalination cycle, compared to a material with high *SAC* [16,17]. An interesting observation was that PAC/Cl, despite low *SAC*, displayed uptake rates 27% faster

than PAC/PTS at 1.2 V [10]. However, despite the slower kinetics, the *SAC* observed using PAC/PTS was 3.8 times higher than obtained using PAC/Cl. Hence, there is a challenge to be overcome, in order to make PAC/Cl technically feasible for application.

Another important aspect related to the choice of an AC for CDI is the production cost. In this regard, a disadvantage of PAC/PTS is the price and the large amount of p-toluenesulfonic acid used in synthesis of the polymer. In contrast, HCl is less expensive, while lower amounts of this reagent are required to produce PAC/Cl, resulting in an AC that offers substantial cost benefits. The easy synthesis and low cost of PAC/Cl make it attractive for application in CDI, however, improvements in the *SAC* and kinetics are still a challenging issue for its effective use.

In this thesis, it was demonstrated for the first time that simply tuning the synthesis of PAC/Cl is a good strategy to produce a more competitive material in terms of *SAC*, kinetics, and cost, which would be suitable for electrochemical desalination. In this sense, the aim of this research was to increase the number of surface functional groups and to develop a hierarchical pore structure looking for improvements of the *SAC* and the adsorption/desorption kinetics, respectively. The strategy used in this study was firstly to synthesize chloride-doped polyaniline, using HCl in the presence of the nonionic surfactant Pluronic^{TM} F127 (PLR). Pluronic triblock copolymers, such as P123 and F127, draw attention to the production of mesoporous carbon due to their commercial availability and tailorable morphologies [18–20]. This compound has been employed previously as a soft template, that act as pore-directing agent, due to the interest in the hydrogen/oxygen interactions that it is able to establish [20–22]. The strategy consists of filling the empty space of a template with a carbon source, followed by carbonization under an inert atmosphere and subsequent removal of the template [20]. The as-obtained polymer was then converted into activated carbon by two different carbonization procedures, either thermal or hydrothermal. Both treatments were followed by KOH activation, according to the optimized conditions determined in earlier work [10]. The thermal carbonization aimed at obtaining an AC with high SOGs content, while the hydrothermal carbonization was employed as a templating technique to achieve a hierarchical pore framework. The hypothesis adopted was that the introduction of these modifications in the synthesis methodology would enable the production of a competitive and suitable carbon for CDI applications.

CHAPTER 2

LITERATURE REVIEW

Water is the basis for life on earth. There is a growing demand in the modern world for water for human or animal consumption, agriculture, and industry. Over the past decades, energy and the environment have received a great deal of attention, and water was declared "21st century oil" by Fortune Magazine in 2000 [23]. In 2015, the United Nations endorsed the 2030 Agenda for Sustainable Development to meet 17 Sustainable Development Goals (SDGs) [24]. The SDG #6, namely "Ensure availability and sustainable management of water and sanitation for all" reflects a particular focus on protecting ecosystems and sustainable water management.

Although most of the earth's surface is made up of water (approximately 3⁄4), 97% correspond to ocean water that is unfit for human, industrial and agricultural consumption, 2% corresponds to polar ice caps and places of difficult access, leaving only 1% of drinking water for use by the global population [25,26]. According to UNESCO [27], more than 2 billion people worldwide are living in water-scarce areas and could reach 5 billion by 2050. This demand has encouraged the treatment, maintenance, and conservation of water resources. In addition, it has also stimulated the development of new technologies for the use of brackish and sea waters and industrial effluents. After being desalinated, they could contribute to supplying the demand for drinking water, for example. Beside water desalination and production of drinking water, water treatment processes can cover a range of applications, including the treatment of wastewater effluents, water softening, and the pre- and post-treatment of industrial water streams.

In this context, desalination has been increasingly considered as a promising alternative for providing drinking water in various regions of the planet. In the case of Brazil, the scarcity of surface water is notorious in the semi-arid region, however, large amounts of brackish water are present underground (~19.5 billion m³) and could be extracted without risk of depletion of water sources [28]. In addition, the long periods of drought that have taken place in the Southeast region are warning of the development of new technologies to provide drinking water to the most populous region of the country. From a social perspective, the desalination of brackish water would be strategic within the Brazilian scenario since the supply of drinking water can promote the social and economic development of regions suffering from depletion.

2.1 Desalination technologies

Desalination processes use chemical engineering technology to separate salts from feed water, generating two outlet streams: desalinated (fresh) water and discharged brine. Since each desalination process causes a decrease in entropy, energy is required in the form of heat, water pressure or electricity [29]. Figure 1 illustrates the overall desalination process diagram.
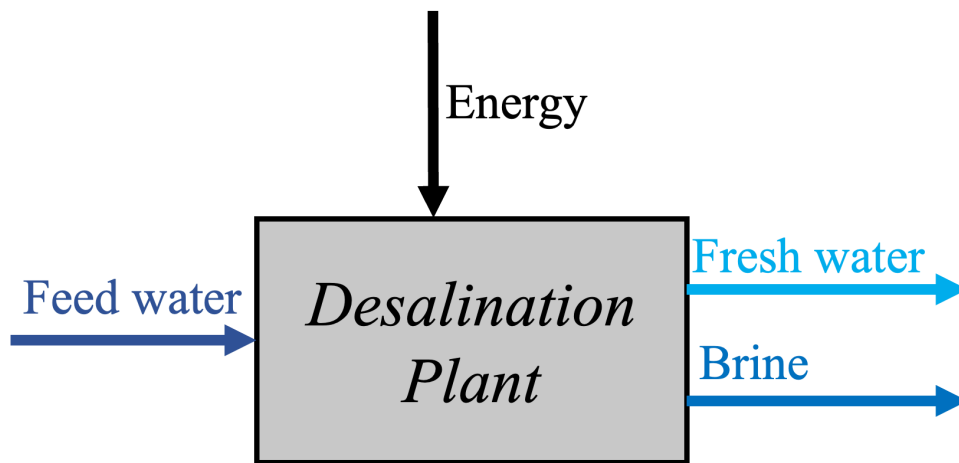
Figure 1. Process diagram for the basic principle of desalination [29]-adapted.

Many technologies are used for desalination, using thermal, membrane, biological and electrochemical methods. Thermal processes include solar distillation, vapor compression, multiple-effect distillation (MED), and multi-stage flash distillation (MSF). Reverse osmosis (RO) and electrodialysis (ED) are techniques that use membranes. Recently, other technologies have been studied, such as microbial desalination cells, membranes with nanocomposites, nanofiltration, electrochemical techniques, among others. The most used technologies in water treatment plants worldwide are RO, MSF, MED, and ED [30]. The worldwide installed capacity for the different desalination technologies, shown in Figure 2, was over 105 million m^3/day (23,000 million gal/day) in 2016. However, this number has been increasing with the growing interest of researchers looking for improvements in the area, estimating that it could reach 250 million m^3/day by 2030 [31].
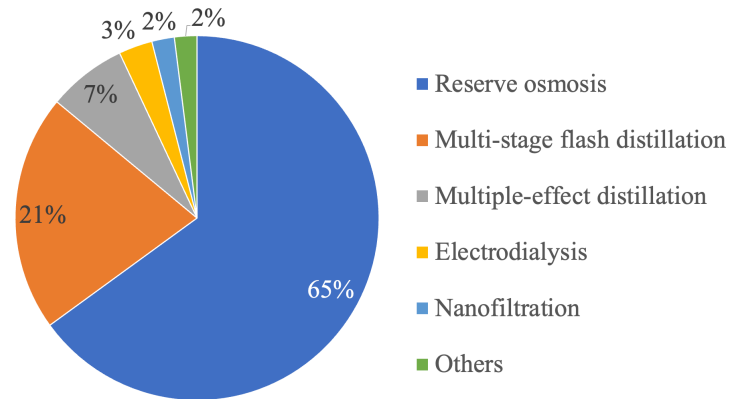
Figure 2. Worldwide installed capacity of different technologies for seawater and brackish water desalination [31].

Distillation (or thermal desalination) is the earliest of desalination technologies and include evaporation of feedwater followed by condensation to produce freshwater [32]. The MSF method is an instantaneous evaporation process in several stages using a set of successive chambers. Figure 3 shows the MSF method, in which salt water evaporates by reducing atmospheric pressure and increasing temperature in each chamber. The resulting steam is condensed separately at heat exchangers and collected as desalinized water [33]. Although distillation processes have the capacity to treat a large amount of water, it is a very expensive technique since it requires a large amount of energy to power the process, for example, for heating the seawater feed, and for the generation of vacuum in the different unit sections [34]. Distillation processes are found essentially in Middle Eastern countries, where fossil fuel is abundant, and water is scarce [35]. However, these processes are economically unviable in most countries on the planet due to the high energy consumption.
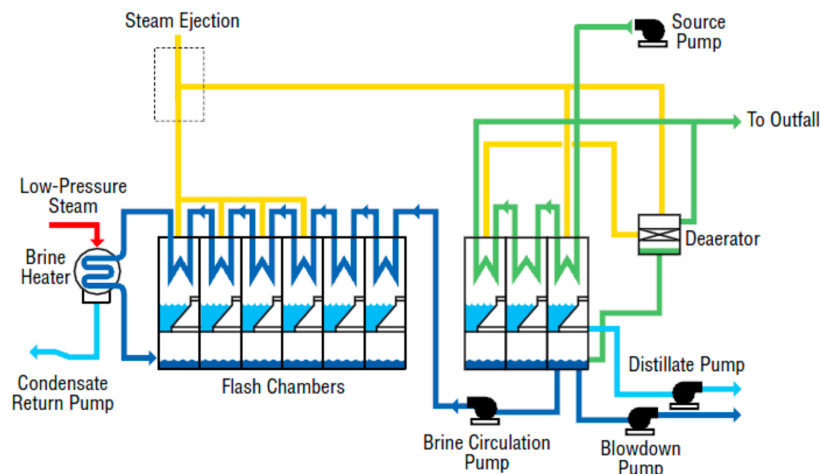
Figure 3. Schematic diagram of multi-stage flash distillation process [36].

The RO process is the most used and responsible for a large amount of desalinated water [37]. In this process, represented in Figure 4(a), the osmotic pressure is overcome by applying an external pressure, higher than the osmotic pressure of the feed water, going up to 55 - 65 bar. Thus, water flows in the opposite direction to the natural flow of osmosis, crossing filter-like semi-permeable membranes (Figure 4(b)), and retaining the passage of salts contained in the saline solution [38]. These systems can be operated in many configurations, depending on the feed water, flow rates, the desired water recovery, product concentrations, and trace substances. Regardless of the salt concentration, high pressure is required, so this method is effective in treating highly saline water, however, requires high energy demand. In the case of Brazil, despite attempts promoted by the government for desalination in the semi-arid region using RO technology, many of the installed equipment are inoperative due to lack of maintenance and difficulty in operation [39]. In addition to these inconveniences, and the high energy consumption due to the use of high-pressure pumps, RO also has other disadvantages, such as calcification and incrustation of the membranes.
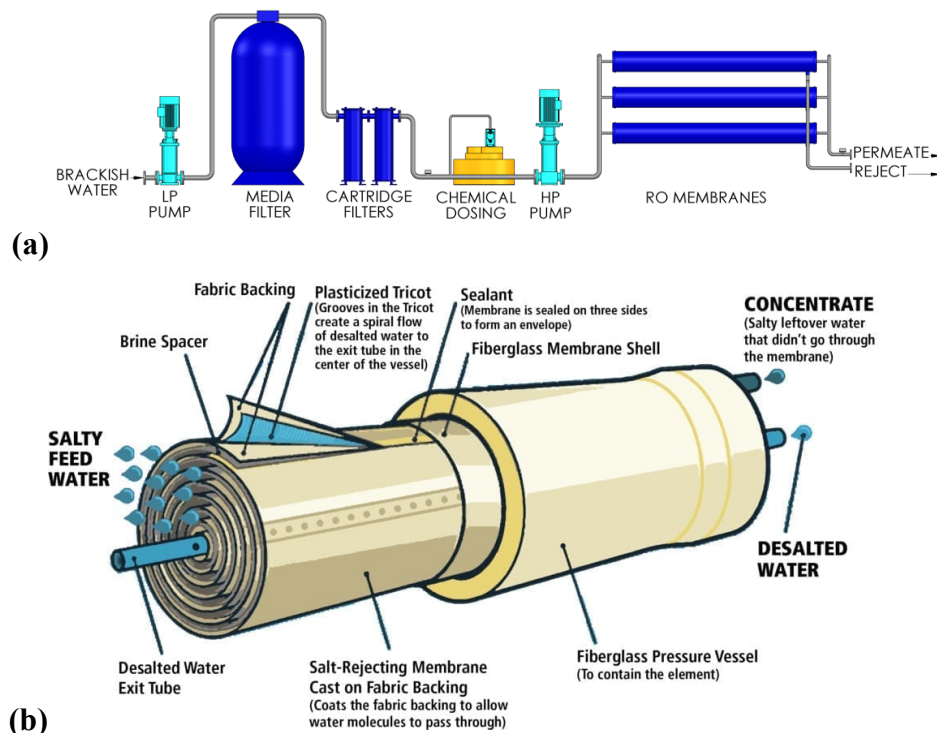
Figure 4. Reverse osmosis: **(a)** plant process flow diagram, and **(b)** membrane element inside a pressure vessel [40,41]. Note: LP and HP is the low and high pressure, respectively.

The use of electrochemical technologies for desalination is old, starting with ED. Unlike RO, this process uses ion-exchange membranes (IEM) to desalinate the water. This technology uses a series of electrically charged membranes in an alternating pattern to separate ions from a saline solution, applying an electrical potential as the driving force. Cation- and anion-exchange membranes (CEM and AEM, respectively) are alternatively oriented between the anode and the cathode, as illustrated in Figure 5. When an electric field is applied across the membranes, cations are attracted to the cathode (negative pole) and anions to the anode (positive pole). Consequently, alternating desalinated and concentrated streams are formed between the membranes. The application of this technology is limited to places where the salt levels in the water are reduced, since its energy consumption is proportional to the salt concentration [42]. Thus, its main disadvantage is the high energy consumption due to the need to supply high voltages to desalinate water with high to medium salinity. Within this context, ED has moved towards more energy efficient processes, such as capacitive (CDI) and faradaic (FDI) deionization, which have become technologically and economically promising alternatives for solving problems involving desalination and water softening [4].
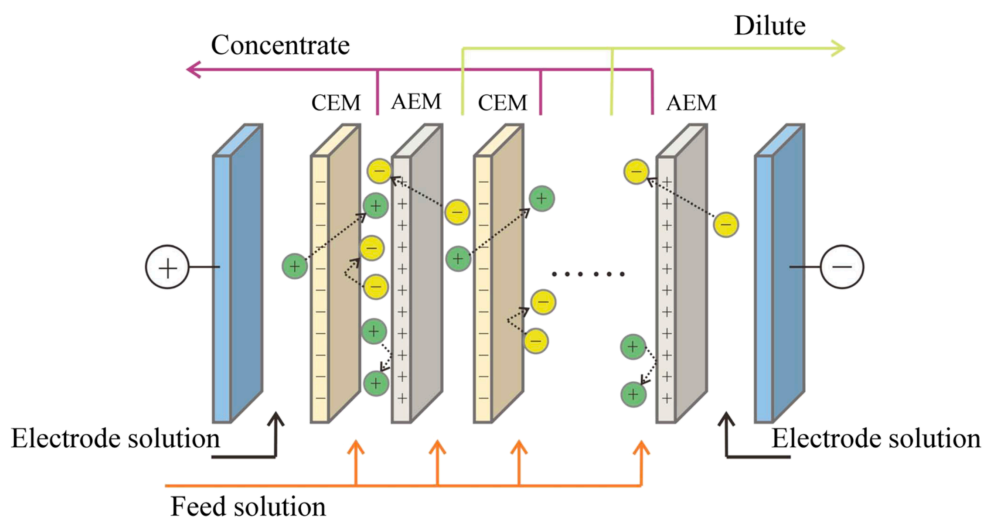
Figure 5. Schematic representation of the electrodialysis system including the cation-exchange membrane (CEM) and the anion-exchange membrane (AEM) [43].

2.2 Capacitive deionization (CDI)

Figure 6 shows possible applications of capacitive deionization. This technology has been studied mainly for application in the desalination of brackish water to obtain drinking water.

More recently, CDI has also been expanded to other water fields, such as: water softening [44,45], selective removal of contaminants (arsenic and hexavalent chromium, for example) [46,47], and recovering mineral resources from wastewater [48,49]. This process could even enable the reuse of water in industrial process, for example.
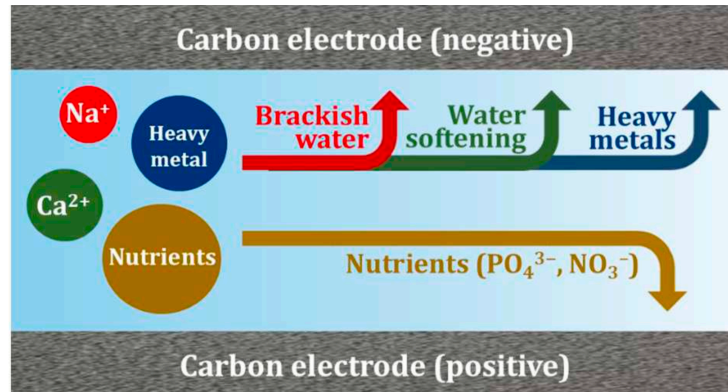
Figure 6. Schematic illustration of possible applications of capacitive deionization. Cations and anions are electrosorbed in the negatively and positively charged electrodes, respectively [50].

The CDI or electrosorption process is based on the same principles that guide the functioning of a capacitor, using carbon materials and the capacitance of the electrical double layer (EDL). However, its main purpose is to remove ions from aqueous solutions using an electrochemical flow cell. When an electric potential or a constant current is applied between two electrodes arranged in parallel, EDL is formed on the surface of the electroactive material (Figure 7(a)), essentially in the micropores. In this case, the voltage applied (potentiostatic mode) or controlled (galvanostatic mode) must be low enough to avoid redox reactions and allow the storage of ions in the EDL. The imbalance of charges on the surface induces the transport of electrically charged species (ions) to the oppositely charged electrodes. So, cations and anions will be removed from the aqueous phase and stored in the EDL formed in the negatively and positively polarized electrodes, respectively (Figure 7(b)). The Gouy-Chapman-Stern (GCS) model (Figure 7(a)) describes the distribution of ions inside the EDL [51], composed of a compact layer at the electrode (inner Helmholtz layer or Stern layer), which does not contain charge, and a charged diffuse layer.

Once saturated, the electrodes can be easily regenerated for another electrosorption cycle. Ion desorption can occur under open circuit conditions (slower process) or by reversing the applied potential (Figure 7(c)), in order to accelerate the process. However, in the latter case,

one should be careful to avoid the crossover process, in which the ions released from one electrode will again adsorbed on the opposite electrode, reducing the effectiveness of the process. This effect can be avoided by using selective membranes [4].

(a)

(b)

(c)
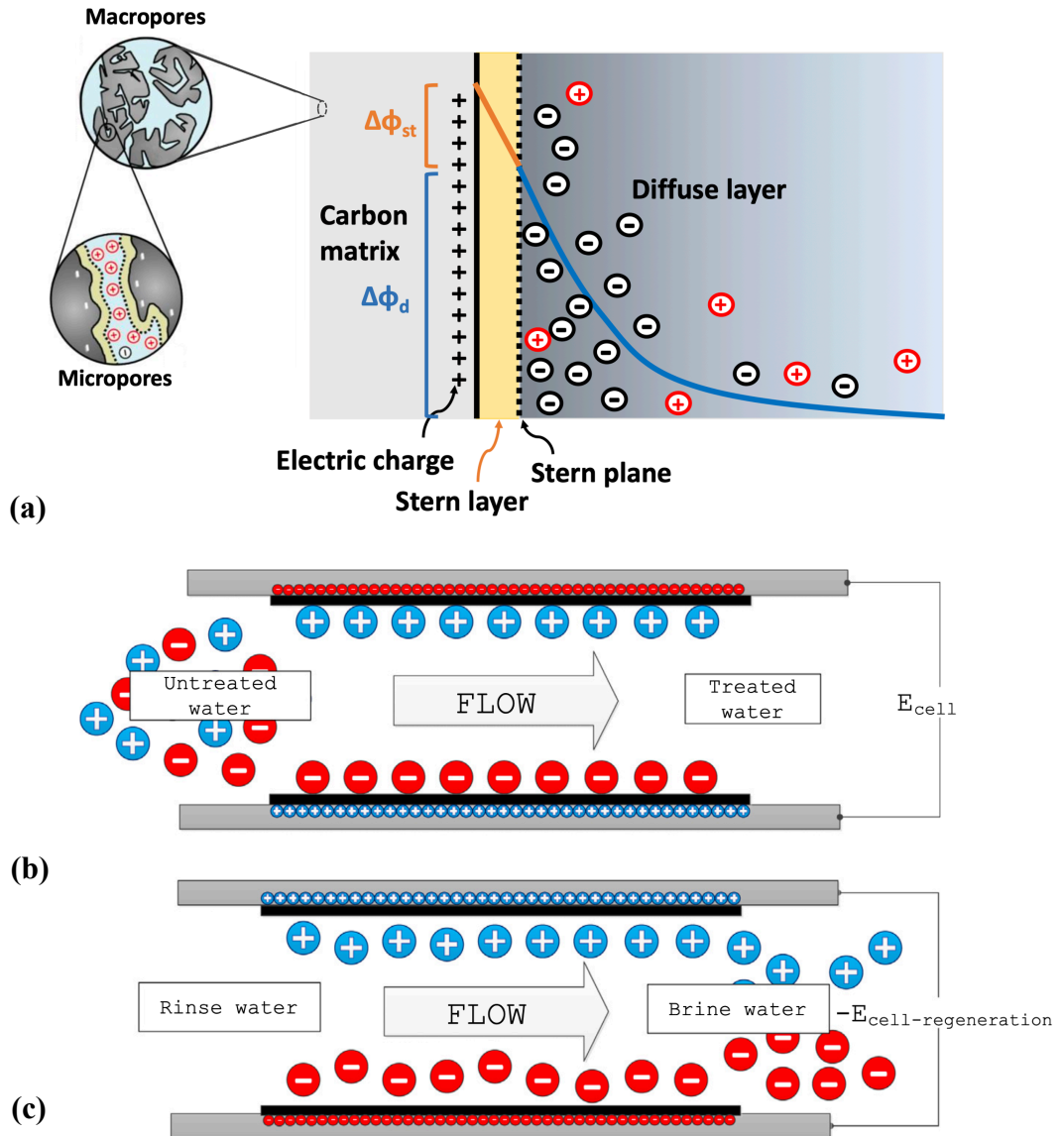
Figure 7. Schematic representations of the electric double layer according to Gouy-Chapman Stern theory [52] **(a)**, and the CDI process: electrosorption of positive and negative charges in the negative and positive electrodes, respectively **(b)**, and regeneration of the electrodes through the desorption of cations and anions into the solution [53] **(c)**. Note: $\varDelta\varPhi_d$: Diffuse layer potential; $\varDelta\varPhi_{st}$: Stern layer potential.

2.3 CDI overview

As in supercapacitors, the GCS model can be applied to describe the structure and interfacial properties between an electronic conductor and an aqueous electrolyte in CDI. The electrical capacitance of the interface can be expressed by the sum of two capacitors in series: the capacitance of the compact layer (outer Helmholtz plane), and the capacitance of the diffuse layer. Ion concentrations decrease progressively with the increasing distance from the electrode surface. The GCS model provides the basis for the formation of other models and demonstrates the importance of using the effective surface area.

Many of the variables that affect EDL thickness and capacitance also apply to the CDI field. This indicates that the efficiency of a material used for electrosorption depends on its capacitance and the electrical potential effectively used to capture counter-ions. Therefore, microporous materials with high *SSA* and high electronic conductivity have shown to be the most promising [52]. However, recent works have also demonstrated the importance of surface chemistry (presence of functional groups) on the potential of zero charge of the electrodes and, consequently, its influence on the co-ion repulsion and the performance of the electrodes used for CDI [13,54,55].

Recently, the effectiveness of CDI in terms of energy, compared to RO process, has been confirmed through a detailed analysis of many aspects that affect the process [56]. This study clarified that previously published results questioning the energy viability of CDI were wrong [57]. Additionally, the CDI process has other advantages compared to more conventional techniques (RO, MSF, and ED), such as reduced energy consumption, use of low pressures, ease of maintenance and cleaning of electrodes [58], and mainly, the possibility of recovering part of the energy used for electrosorption of ions, as it is a capacitive system [59,60]. All these characteristics make the CDI technique very attractive in terms of energy and capital costs, when compared to technologies already established and used industrially, becoming a feasible alternative for the supply of water for consumption and/or reuse.

The need to produce fresh water was a long-standing reason for the development of the capacitive deionization. The CDI approach has been documented since the 1960s, when it was known as "electrochemical demineralization" or "electrosorb process for desalting water", using porous carbon electrodes with high surface area [61]. The authors provided conceptual evidence that electrochemical desalination could be feasible. Recently, because of increasing water stress issues, and due to the advantages of CDI already mentioned, academic research interest in this technology has increased exponentially over the past 20 years, as shown in Figure

8. In recent years, this technique has been moving from the laboratory to the pilot scale, increasing commercial and industrial interest for CDI systems [60,62,63]. Most of the studies carried out in CDI concern the development of electrode materials, in particular carbonaceous materials.
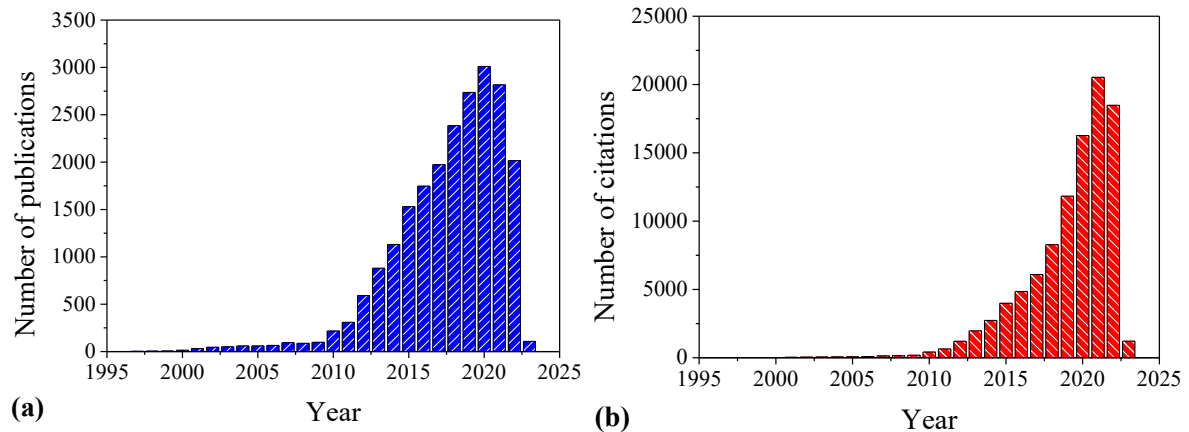
Figure 8. Number of publications **(a)** and citations **(b)** per year since 1996 based on search for "capacitive deionization" on the Web of Science (Access in January 2023).

Despite the advantages presented, the CDI technology still presents some challenges, such as the limitation in terms of electrosorption capacity at higher concentrations (seawater) and its rapid deterioration in performance with the presence of dissolved oxygen in the medium [64]. In addition, it can suffer from co-ion repulsion, responsible for decreasing the charge efficiency of the process. The latter can be eliminated or minimized by creating electrode asymmetry or using ion-selective membranes, known as MCDI.

The use of asymmetric configurations in CDI is a good strategy to improve the desalination performance and the electrode stability for long-term operation. Asymmetry can be established using electrodes with different thicknesses, sizes, masses, materials, or surface charges [17,65]. The asymmetry acts shifting the E_{PZC}, which maximizes the effective electrode potential used to electrosorb counterions and reduces the co-ion repulsion [66,67], and introducing additional attractive forces to remove the counterions from the electrolyte [23]. According to Barcelos et al. [68], the control of the potential distribution in asymmetric cells is mandatory to improve the long-term stability and suppress the carbon oxidation reactions that decrease the salt removal capacity.

Another strategy to eliminate or minimize the deleterious effect of co-ion repulsion is the use of ion-selective membranes. According to Zornitta and Ruotolo [17], a large increase in

the electrosorption capacity can be achieved by increasing the voltage from 1.2 to 1.4 V in a MCDI cell, without the occurrence of faradaic reactions. These results suggest that the applied voltage must be optimized considering the ohmic drop in the cell. Recently, Lado et al. [55] using sugarcane biowaste-derived biochars, obtained an impressive increase in *SAC* using membrane. This work clarifies that the additional cost introduced using the membrane can eventually be offset using a low-cost electrode if it presents sufficiently high ion removal capacity and kinetics. This issue is corroborated by the work recently published by Hand et al. [69], in which a techno-economic analysis of the MCDI process reveals the cost of the membrane as the main component of the total cost, including capital and operational.

2.4 CDI electrode materials

Capacitive deionization is a dynamic and complex process that depends on the textural properties (specific surface area, and pore size distribution) and surface chemistry of the electroactive material, as well as the flow patterns and concentration profiles within the CDI cell. Therefore, understanding the fundamentals involved in these aspects is of paramount importance not only for the design of the electrochemical cell, but also for the process optimization.

The electrode can be considered the central element that makes up a CDI cell and certainly one of the main factors that affect its performance. The main requirements for a good CDI electrode are: 1) high *SSA*, with adequate PSD to make the material surface accessible to ions for electrosorption in the EDL; 2) high electrical conductivity to promote rapid electrochemical response of all surface to electrosorption/desorption cycles; 3) chemical and electrochemical stability in voltage changes, 4) high wettability, 5) low contact resistance between the porous electrode and the current collector, and 6) low cost and easy scalability [52,70].

SSA is a necessary condition, but not sufficient to guarantee high values of *SAC* (expressed in mg salt per g active material). The PSD affects not only ion diffusion but also *SAC*, since many of the micropores that confer a high *SSA* may not be available for electrosorption [71]. The use of materials with adequate PSD, in addition to facilitating the diffusion and improving the kinetics of the process, is also important to avoid the EDL overlapping, which has an impact on the electrosorption capacity. As a result, the search for improvements in desalination performance begins with an understanding of the role of the properties of the materials, as well as the understanding of how the variables of preparation of

these materials influence the textural and electrochemical properties of the electrodes. In addition, it allows customization according to the desired characteristics for each application [11,55].

The higher the *SSA*, the higher the number of sites for electrosorption, having a positive impact on the *SAC*. In the case of pore size, its dimension must be bigger than that of the solvated ion to allow access to these sites [72]. Although subnanometric pores (< 1.0 nm) are eventually accessible to ions due to an ionophobic effect [73], it may result in the EDL overlapping [74], which would contribute marginally to the total electrosorption capacity. In fact, microporous materials, with pore sizes between 1.0 and 2.0 nm according to IUPAC (Figure 9), have been reported as the most suitable for electrosorption [75,76]. However, electrosorption and desorption kinetics in micropores are slower. In this sense, the search for the introduction of mesopores (pores between 2 and 50 nm) has been reported by several authors to improve the kinetics of the process, since the mesopores function as large "avenues" that facilitate the diffusion of ions to the micropores [53,74].
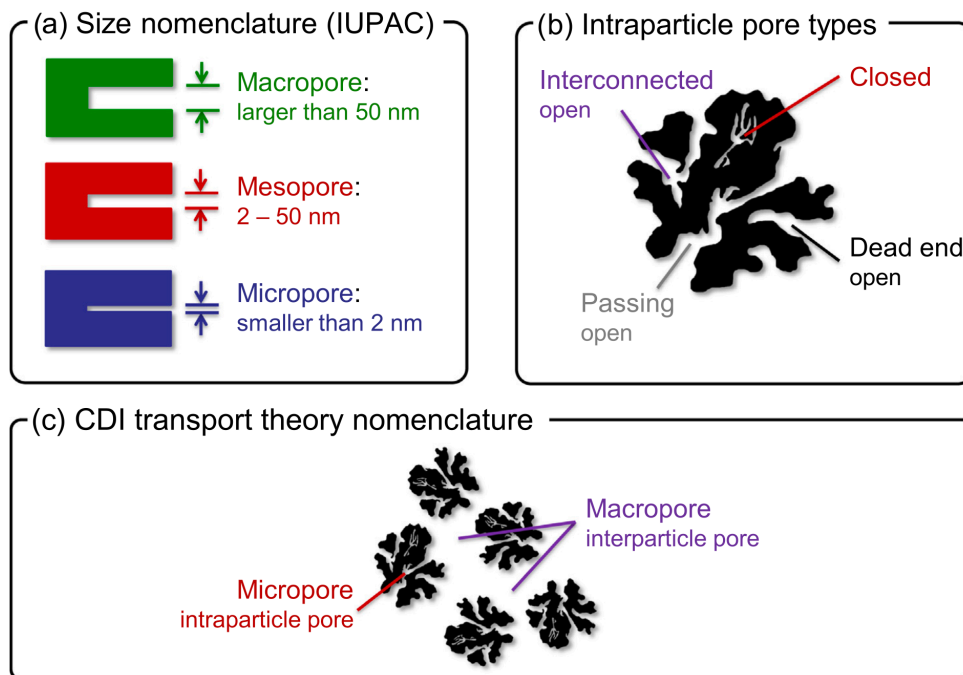
Figure 9. Nomenclatures of pore size according to IUPAC **(a)**, intraparticle pore **(b)**, and porous media transport theory **(c)** [52].

The study and application of carbon-based materials have been distinguished as electrode materials for CDI, considering the main requirements for a good electrode [70]. Carbonaceous

materials from different origins have been used for the preparation of electrodes, such as activated carbons [10,77,78], carbon cloth and felts [62,79,80], nanotubes [81–83], graphene [84–86], carbide-derived carbon [65,87,88], carbon aerogels [72,89,90], and low-cost materials from biomass waste [55,91,92]. In general, these materials offer *SSA* ranging from 600 to 3100 m^2 g^{-1} and high electrical conductivity [93–96]. In addition to the advantages presented, carbon materials allow the customization of textural properties to obtain adequate PSD and surface groups, which will improve the desalination performance [97].

A further important characteristic of the carbon electrodes used in CDI relates to the presence of surface functional groups, which will determine their ability to remove ions from the solution. Depending on the form of carbonization, surface oxidation reactions and the type of activation used (chemical or physical), the material obtained may have a smaller or larger amount of carboxylic, phenolic, carbonyl (quinone-type), anhydride and lactone, among others [13,98,99]. These groups are generally carboxylic (give a negative charge) or amine-based (give a positive charge), as illustrated in Figure 10, when oxygen and nitrogen atoms are present in the carbon structure [37]. These surface functional groups, mainly those of oxygen, in addition to improve the electrode wettability (hydrophilicity) [12,100], also influence the electrochemical activity, such as E_{PZC} [11,54,101]. The E_{PZC}, in turn, will determine the degree of co-ion repulsion and the stability window of the electrodes, which will have a direct influence on the *SAC* values and the number of cycles that the electrode will be able to perform [68].
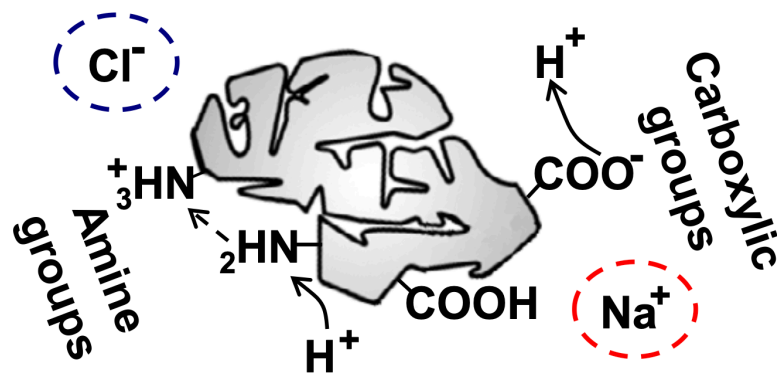
Figure 10. Chemical surface charges on the porous electrode [52].

Low-cost commercial activated carbons, such as carbon felt, carbon veil, carbon foam, and carbon cloth [53], or prepared from practically zero-cost biomass residues, such as sugar cane bagasse fly ash [12,102], lignin [97], and crude glycerol [103], despite the low cost, they presented low values of *SAC* (ranging from 4.3 to 18.2 mg g^{-1}). These materials showed slightly

better results just using MCDI. For this reason, many author have been investigating the use of other types of activated carbons, such as conducting polymers.

Polyaniline (PAni) and polypyrrole (PPy) are two common conducting polymers that have been investigated in depth as electrode materials for the CDI process [8–10,104]. PAni generally has higher mechanical resistance and capacitance than PPy, while the latter exhibits higher electrical conductivity and stable electrochemical properties at a wide range of pH [105]. In addition, PAni can be easily combined with anionic dopants used as model agents to define texture characteristics and electrochemical performance of electrodes [10]. For this reason, it has been used extensively in energy storage applications [106], ion-exchange processes [107], sensor schemes [108], and water desalination [68].

In an effort to increase electrosorption capacity, Zornitta et al. [11] developed an activated carbon derived from polyaniline doped with p-toluenesulfonate (PAC/PTS), achieving very promising results in terms of SAC (22.2 mg g^{-1}) and charge storage capacities (212 F g^{-1}) observed for EDL-based electrodes, without the need to use membranes. This electrode material presented remarkable textural properties, such as high surface area (3600 m^2 g^{-1}) and pore volume (2.3 cm^3 g^{-1}). However, despite the excellent results, the higher cost of this activated carbon is still an obstacle to its use.

2.5 Underlying the background

According Zornitta et al. [10], the activated carbon derived from chloride-doped polyaniline (PAC/Cl), despite having higher SSA (2652 m^2 g^{-1}), showed a lower desalination performance (SAC = 5.8 mg g^{-1}) compared to PAC/PTS, mainly due to its low content of surface oxygen groups. Despite the low SAC value of PAC/Cl, it showed faster removal kinetics than PAC/PTS at 1.2 V [10]. In addition, it is worth noting that the preparing cost of PAC/Cl is much lower than that of PAC/PTS. While PAC/PTS requires large amounts of HPTS in the polymer synthesis, PAC/Cl requires small amounts of HCl, which is cheaper than the previous one, making it economically attractive. Considering all these aspects, PAC/Cl still presents challenges to be overcome regarding improvements in SAC and kinetics, in order to make it technically feasible for application.

In this context, many authors have been investigating the use of different strategies to improve the properties of the electrode material, such as doping with heteroatoms (e.g., N, B, and P atoms) in the carbon frameworks [94,109], composites (e.g., carbon source and reduced graphene oxide) [110,111], or soft templates (e.g., ceramic polymer, sponge and polymer

surfactants) [112–114]. Pluronic (PLR) are triblock copolymers, composed by two hydrophilic chains of polyethylene oxide (PEO) and the central hydrophobic part of polypropylene oxide (PPO). They are commercially available non-ionic surfactants, such as P123 and F127, and have been applied to produce mesoporous carbon due to their customizable morphology. This type of compound has been used as a pore-directing soft template, due to the possible hydrogen/oxygen interactions [18–20,115–117]. The advantages of this approach are low-cost materials, simple operation, and high efficiency.

Figure 11 shows the carbonized PAni/Cl preparation scheme by a F127-mediated self-assembly process. PLR in the contact with aniline forms a micellar system through the bond between its hydrophilic part (PEO) and the aniline monomers. After the addition of the oxidant (ammonium persulfate, for example), the oxidation polymerization of the aniline monomers occurs, forming the polyaniline/PLR composites. Finally, carbonization is carried out to remove the PLR, which modifies the structure of the material. Pluronic F127 decomposition takes place at temperatures between 250 and 430 °C [114,118]. According to Yu et al. [119], mesopores result from the thermal decomposition of PLR. Results obtained by Xin et al. [20] indicated that pore morphologies were clearly changed and there was an increase in the mesoporous surface area by adding F127 during the sample preparation.
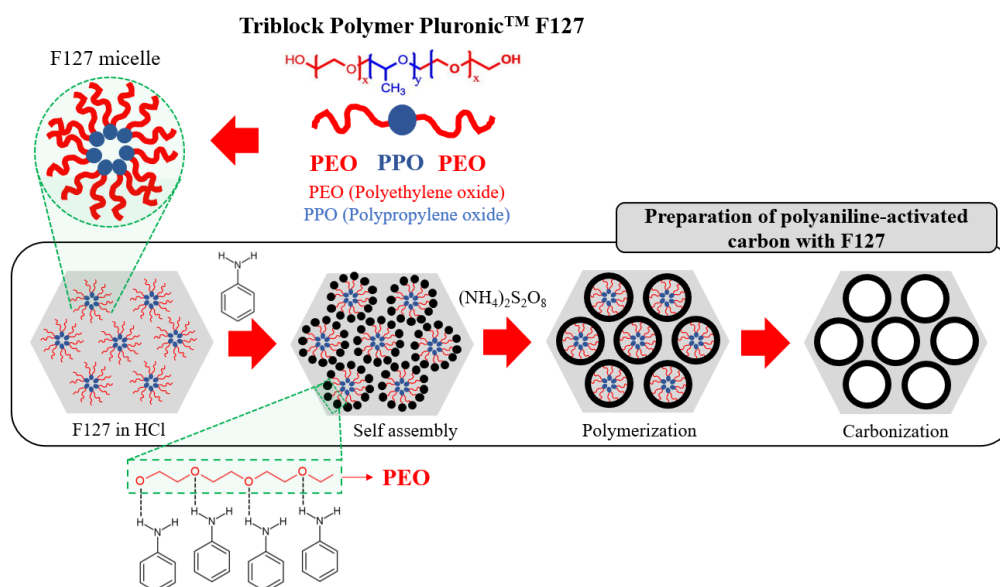
Figure 11. Schematic illustration of the micellar system formed between Pluronic™ F127 and aniline [20]-adapted.

Among the different carbonization processes, thermal and hydrothermal stand out. Thermal carbonization aims to obtain an activated carbon with a high SOG content, while hydrothermal carbonization is usually employed as a modeling technique to obtain a hierarchical pore structure [12,119]. Hydrothermal treatment and solvent-evaporation induced assembly are the most common methods used to prepare mesoporous carbon using F127 template. However, these methods may present some difficulties due to the metastable conditions that make it difficult to control particle size [120].

Hierarchical porosity provides an interconnected porous network that combines large and small mesopores and micropores [119]. The large mesopores serve as ion buffer reservoirs, from which ions can be transported to the small mesopores. So, the ions can diffuse along the mesopore channels to access the micropores. Ordered mesopores (2 to 50 nm), formed within the walls of macropores by removal of the soft template, can improve the ion transport through the pore network [121,122]. Furthermore, it has been reported in the literature that changes in the macrostructure of a conventional electrode improve the effective ionic conductivity, creating a bi-tortuous electrolyte diffusion pathway [123,124]. The tortuosity of the porous electrode is determined by the size of the pores and the shape of the solid particles. In addition to the importance of mesoporosity and wettability in the ion transport, a developed microporosity can provide a large quantity of active electrochemical sites and, consequently, a large capacitance.

Before being applied in CDI, after carbonization of the polymer, the material needs to be converted into activated carbon. Activation of carbon-based materials is usually carried out through chemical activation (using KOH), physical activation (using CO_2), or a combination of both, in order to improve the adsorption capacity [125]. Activation with CO_2 is responsible mainly for the generation of mesopores and low SOG content, due to the low CO_2 reactivity [55]. On the other hand, chemical activation typically provides higher surface area, improved pore development composed mainly by micropores, and high carbon yield. KOH increases *SSA* by intercalating metallic K into carbon networks, causing them to expand. In addition, activation with KOH is responsible for generating SOGs. The knowledge of the surface chemistry, that is, the type and quantity of functional groups, mainly those of oxygen, is essential to propose an adequate electrode configuration (asymmetry) in order to minimize the deleterious effect of co-ion repulsion on the electrosorption capacity.

Another important aspect related to electrode material for CDI is the electrosorption/desorption kinetics. The development of electrodes with high *SAC* and fast kinetics is still a challenge that needs to be solved. Zornitta and Ruotolo [17] demonstrated that

even a material with high *SAC* may have a lower desalination performance than a material with a lower *SAC* and faster kinetics. This means that the latter will be able to perform a higher number of electrosorption/desorption cycles. This methodology, called optimized salt removal (*OSR*), is an important tool for a more careful analysis of the best electrode for desalination, considering both kinetic and *SAC* aspects.

2.6 Objectives

Considering the state of the art on capacitive deionization and hypotheses presented, the main objective of this thesis was to investigate strategies to improve the adsorption capacity and boost the kinetics of chloride-doped polyaniline activated carbon by modifying the synthesis procedure, aiming to obtain a cost-attractive electrode for CDI application. To achieve this objective with a view to furthering knowledge in this area, the following specific objectives were established:

- Elucidate the role of Pluronic^{TM} F127 (PRL) as a soft template material for improving the *SAC*;
- Develop a hierarchical pore structure using hydrothermal carbonization aiming to further improve the electrosorption/desorption kinetics;
- Investigate the use of PRL in combination with hydrothermal carbonization;
- Compare thermal and hydrothermal synthesis for the preparation of activated carbons;
- Evaluate the effect of physical activation on the generation of a 3D framework;
- Evaluate the effect of chemical activation on the generation of SOGs;
- Increase the number of SOGs looking for improvements of the *SAC*;
- Study the effect of the asymmetric configuration of the electrodes in minimizing the effect of co-ions, aiming to maximize the electrosorption capacity;
- Compare the desalination performance between different electrodes considering *SAC* and kinetics, simultaneously.

CHAPTER 3

MATERIALS AND METHODS

In this chapter, the materials and equipment used to perform the experimental procedures this work are presented, especially in the PAC/Cl synthesis, electrode preparation and characterization, and electrosorption experiments. In addition, the analytical methodologies and data treatment employed are presented.

3.1 Materials

For the polyaniline synthesis, distilled aniline (99%, Sigma-Aldrich), hydrochloric acid (37%, J.T. Baker), ammonium persulfate (98%, Synth), and the nonionic surfactant Pluronic™ F127 (12,600 g mol^{-1}, Sigma-Aldrich) were used as monomer, doping anion source, oxidant, and templating agent, respectively. Potassium hydroxide (Sigma-Aldrich) was used as activating agent. For electrode preparation, polyvinylidene fluoride (PVDF, Sigma-Aldrich), *n*-methylpyrrolidone (NMP, 99.5%, Synth), and graphite sheet were used as binder, solvent, and current collector, respectively. Sodium chloride (Synth) was used in the desalination experiments. The commercial YP-80F activated carbon (Kuraray Co.) was used as the counter electrode and anode in the electrochemical characterization and desalination experiments (to provide asymmetry), respectively.

3.2 PAC/Cl synthesis and electrode preparation

Firstly, PAni was chemically synthesized using an adaptation of the procedure proposed by Xin et al. [20], shown schematically in Figure 12. Briefly, 3 g of PLR was dissolved in 1 L of 0.1 M HCl, followed by addition of 55.3 mL of aniline (0.57 mol L^{-1}, previously distilled to prevent oxidation), under constant stirring. The solution was maintained at 3 °C [10,126] and the polymerization was started by slowly dripping 500 mL of the oxidant (2.2 mol L^{-1} (NH$_4$)$_2$S$_2$O$_8$) into the monomer solution. A detailed mechanism of oxidative polymerization of aniline was described elsewhere [127,128]. The reaction was carried out for 11.5 h, under stirring. The chloride-doped PAni was filtered, washed with ethanol and deionized water, and dried in an oven at 75 °C for 36 h. For comparison, the same synthesis was carried out in the absence of PLR.
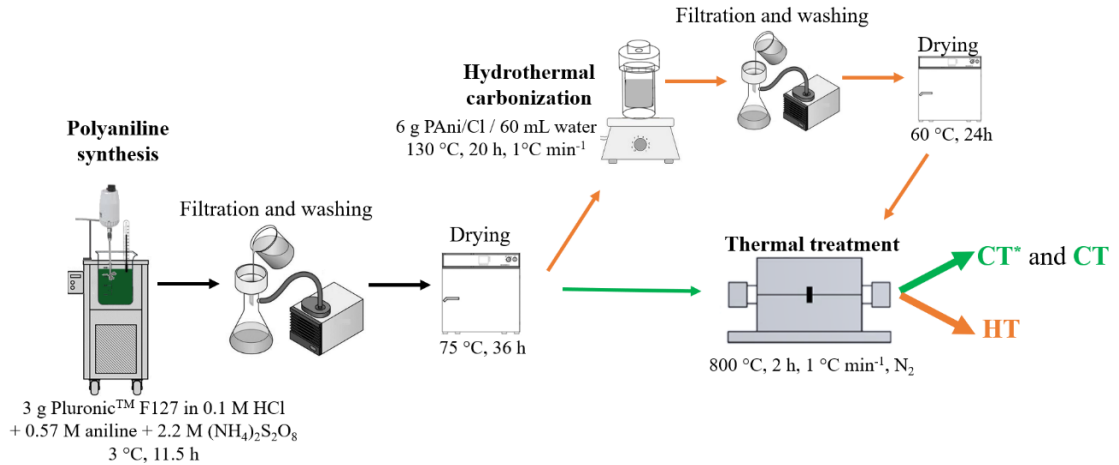
Figure 12. Schematic representation of the polyaniline synthesis and carbonization process.

The PAni/Cl samples were thermally carbonized in a tubular furnace (Lindberg Blue M, Thermo Scientific), using conditions similar to those described by Zornitta et al. [10], with heating at 800 °C for 2 h, under an atmosphere of N_2 (150 mL min^{-1}), but employing a slower heating rate (1 °C min^{-1}), in order to compare with hydrothermally carbonized samples. For hydrothermal carbonization, the samples were firstly left for 20 h at 130 °C (with heating at a rate of 1 °C min^{-1}) [129] in a hermetically closed hydrothermal reactor (with a 100 mL Teflon liner), using 6 g of PAni/Cl in 60 mL of deionized water, under stirring (Figure 12). After filtration and drying at 60 °C for 24 h, the solid was thermally treated in the tubular furnace, following the same procedure described above for carbonization (800 °C, 2 h, 1 °C min^{-1}). The thermally carbonized samples were labeled as CT (using PLR) and CT* (without PLR), while the hydrothermally carbonized material was denoted HT. The asterisk indicates that the PAni/Cl synthesized in the absence of PLR was used for carbonization. Table 1 summarizes the nomenclature of the different samples prepared in the absence and presence of PRL.

After carbonization, the samples were chemically activated with KOH in a proportion of 4:1 (KOH:PAni, w/w), followed by heating at 850 °C (10 °C min^{-1}) for 1.5 h, under an atmosphere of N_2 (150 mL min^{-1}) [10]. The as-obtained activated carbons were washed with 0.5 mol L^{-1} HCl and warm water (60 °C) until constant pH, followed by drying at 100 °C for 24 h (Figure 13(a)). The activated CT and CT* samples were denoted as CTAK (with PLR) and CTAK* (without PLR), respectively, and the activated HT sample as HTAK. For comparison, a sample of HT was physically activated using CO_2 in the tubular furnace (150 min^{-1} CO_2, 800 °C, 10 °C min^{-1}, 2 h) [55]. This activated sample was denoted HTAC. Finally, an additional sample was prepared by chemical activation of HTAC using KOH (850 °C, 10 °C min^{-1}, 1.5 h), which was labeled as HTACK (Figure 13(b)).

Table 1. Nomenclature of samples prepared in the presence and absence of Pluronic

Material	Description
CT	Thermally carbonized sample, followed by thermal treatment
CT*	Thermally carbonized sample without Pluronic, followed by thermal treatment
CTAK*	Thermally carbonized sample without Pluronic, followed by activation using KOH
CTAK	Thermally carbonized sample, followed by activation using KOH
HT	Hydrothermally carbonized sample, followed by thermal treatment
HTAC	Hydrothermally carbonized sample, followed by thermal treatment and activation using CO_2
HTAK	Hydrothermally carbonized sample, followed by thermal treatment and activation using KOH
HTACK	Hydrothermally carbonized sample, followed by thermal treatment and activation using CO_2 and KOH

Note: Asterisk means sample prepared in the absence of Pluronic.
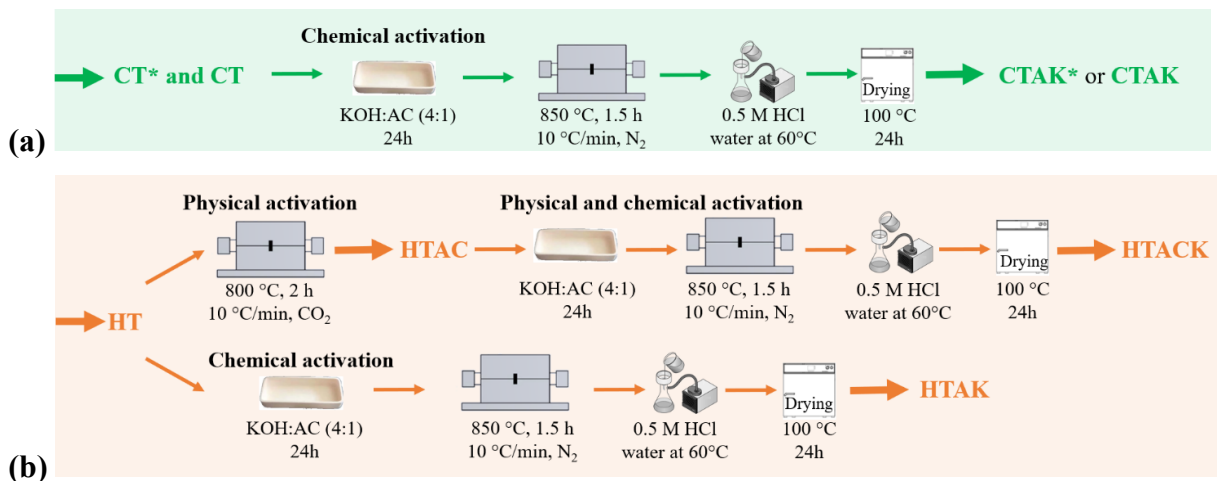
Figure 13. Schematic representation of chemical activation of the CT and CT* samples **(a)**, and chemical and physical activation of the HT samples **(b)**.

All the electrodes were prepared by mixing 13 wt% of PVDF, previously dissolved in NMP, and 87 wt% of activated carbon. The amount of PVDF was optimized in previous tests and was defined as the minimum necessary to ensure the mechanical stability and electrical conductivity of the carbon film electrode. The slurry was spread onto a graphite sheet substrate using a doctor blade machine (Figure 14). The carbon films were formed after evaporating the solvent in an oven at 80 °C for 12 h [16]. The thickness of the electroactive carbon film was 300-350 μm.
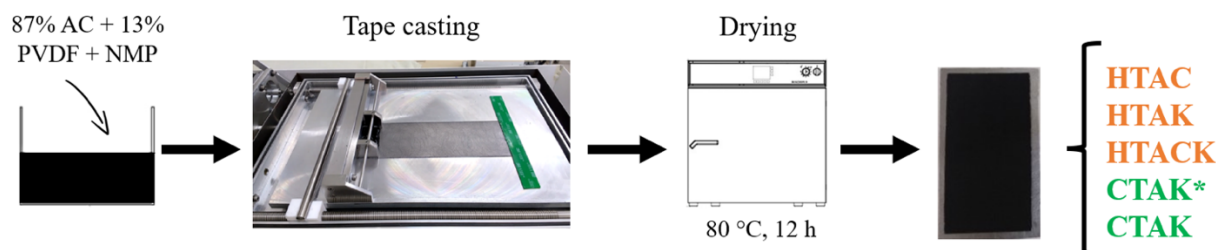
Figure 14. Schematic representation of the electrode preparation procedure.

3.3 PAC/Cl and electrode characterization

High-resolution transmission electron microscopy (HRTEM) images were acquired using a drop of aqueous suspension containing the sample deposited onto a carbon-coated copper grid and dried in air, followed by analysis using an FEI-TECNAI G2 F20 microscope operated at 200 kV.

X-ray diffraction (XRD) data were recorded from 5° to 70° (at 3° min^{-1}), using a Philips Analytical X´Pert-MPD X-ray diffractometer fitted with a Cu Kα source (λ = 1.5406 Å), operated at 40 kV and 40 mA.

Elemental analysis (CHNS) was performed using a Flash 2000 CHNS/O Analyzer (Thermo Scientific) operated at 900 °C and calibrated with BBOT.

The surface chemical groups were first identified by Fourier transform infrared spectroscopy coupled with attenuated total reflection detection (ATR-FTIR), using a Bruker Vertex 70 spectrophotometer fitted with a diamond crystal cell.

X-ray photoelectron spectra were recorded using a laboratory spectrometer (SPECS GmbH, Berlin) with a monochromatic Al Kα source (hν = 1486.6 eV) at 50 W excitation. The X-rays were focused onto a 300 μm spot on the sample, using a μ-FOCUS 600 monochromator. Data were recorded with a PHOIBOS 150 NAP 1D-DLD analyzer, in fixed transmission mode. The energy step was set at 40 eV for survey scans and at 20 eV for high-resolution regions. The binding energy scale was calibrated using Au 4f7/2 (84.01 eV) and Ag 3d5/2 (368.20 eV). Charge compensation was required for data collection and the spectra were further calibrated against the C 1s internal reference. Data interpretation was performed with CasaXPS software. Shirley or two-point linear backgrounds were used, depending on the spectrum shape. Surface chemical analysis was performed based on the high-resolution spectra peak areas and CasaXPS sensitivity factors (where RSF of C 1s = 1.000).

Raman spectra were recorded using a Horiba LabRAM HR Evolution spectrometer fitted with a Nd-YAG laser (532 nm; 600 x 50 grid). The degree of carbon ordering was estimated using the Raman peak intensity ratio (I_D/I_G), where the D mode indicates the presence of a disordered carbon structure, while the G mode is related to sp^2-hybridized carbon atoms [130,131].

The textural properties of the activated carbons were assessed from N_2 adsorption/desorption, measured using an ASAP 2010 instrument (Micromeritics). Prior to the measurements, the samples were first degassed at 90 °C for 18 h and then at 200 °C for 6 h. The specific surface area was calculated using the Brunauer-Emmett-Teller equation (SSA_{BET}), considering relative pressure (P/P_0) between 0.05 and 0.20 (linear region of the isotherm). The PSD and total pore volume (V_T) were calculated using the 2D-NLDFT heterogeneous surface model and SAIEUS software. The micropore (V_{mic}) and mesopore (V_{mes}) volumes were determined from the volume of N_2 adsorbed by pores ≤ 2 nm and by the difference between V_T and V_{mic}, respectively. The average pore diameter (d_{50}) was determined considering the pore diameter for which the volume adsorbed was half of V_T.

The electrode wettability (hydrophobicity/hydrophilicity) was assessed by measuring the contact angle, according to the sessile drop method, with a water droplet deposited onto the surface of the carbon electrode. After 10 s, the angle between the line tangential to the liquid interface of the drop and the baseline was measured.

The electrodes were electrochemically characterized by cyclic voltammetry (CV) and electrochemical impedance spectroscopy (EIS), using an electrochemical workstation (Multi Autolab/M204, Metrohm). A three-electrode Swagelok cell configuration was employed, with Ag/AgCl (KCl$_{sat}$) as the reference electrode, while AC from polyaniline and YP-80F (both 1 cm diameter and 0.78 cm^2 of area) were used as the working (WE) and counter (CE) electrodes, respectively. The WE active mass was 1.4 ± 0.1 mg. The CE mass was 3-fold higher than the WE. The voltammograms were recorded scanning the potential between -0.2 and 0.6 V *vs*. Ag/AgCl (in which only capacitive effects can be considered), at 5 mV s^{-1}, with 1.0 mol L^{-1} NaCl as the electrolyte solution. This potential window was stablished from previous tests varying the cathodic and anodic vertex potentials, considering the potential stability limits of the cathodic and anodic electrodes in order to prevent water splitting (faradaic reactions) at very negative or positive potentials. The specific capacitances (C_S) of the electrodes (F g^{-1}) were calculated using Eq. (1), where I is the current (A), v is the scan rate (V s^{-1}), and m is the mass of activated carbon in the working electrode (g).

$$C_S = \frac{I}{v\,m}$$ (1)

EIS measurements were performed at frequencies ranging from 1 mHz to 100 kHz, at 0.0 V *vs.* Ag/AgCl (0.2 V vs. SHE) and an alternating current amplitude of 10 mV. The ohmic (R_Ω) and charge-transfer (R_{CT}) resistances were estimated by fitting of the semicircle of the Nyquist plots using Metrohm Autolab NOVA v. 2.1 software. The E_{PZC} was also determined by EIS in 0.01 mol L^{-1} NaCl (600 mg L^{-1}), applying 10 mHz (frequency), 30 mV (amplitude), and a potential step of 25 or 100 mV in a pre-established electrode potential range. The E_{PZC} of each sample was defined by the lowest capacitance value when normalized considering the lowest observed capacitance at each potential ($C/C_{min} = 1$). Consequently, it allows to know if the electrode has excess of positive or negative charges on the surface [11,132,133]. The capacitance at each potential was calculated using Eq. (2), where ω is the angular frequency and Z'' is the imaginary component of the impedance spectrum.

$$C_{EIS} = \frac{1}{|\omega Z''|}$$ (2)

3.4 Electrosorption experiments

The electrosorption experiments were performed in recirculating batch mode, using an electrochemical cell described previously [16]. Briefly, the cell was composed by two parallel electrodes (2.0 cm × 2.3 cm, 47.5 ± 5.8 mg active material) contacting graphite current collectors attached to two acrylic plates. In order to avoid short circuit and allow electrolyte flow, the electrodes were separated by a plastic mesh. The cell was assembled using nuts and bolts, with rubber gaskets providing tight sealing (Figure 15(a)).

(a)

(b)
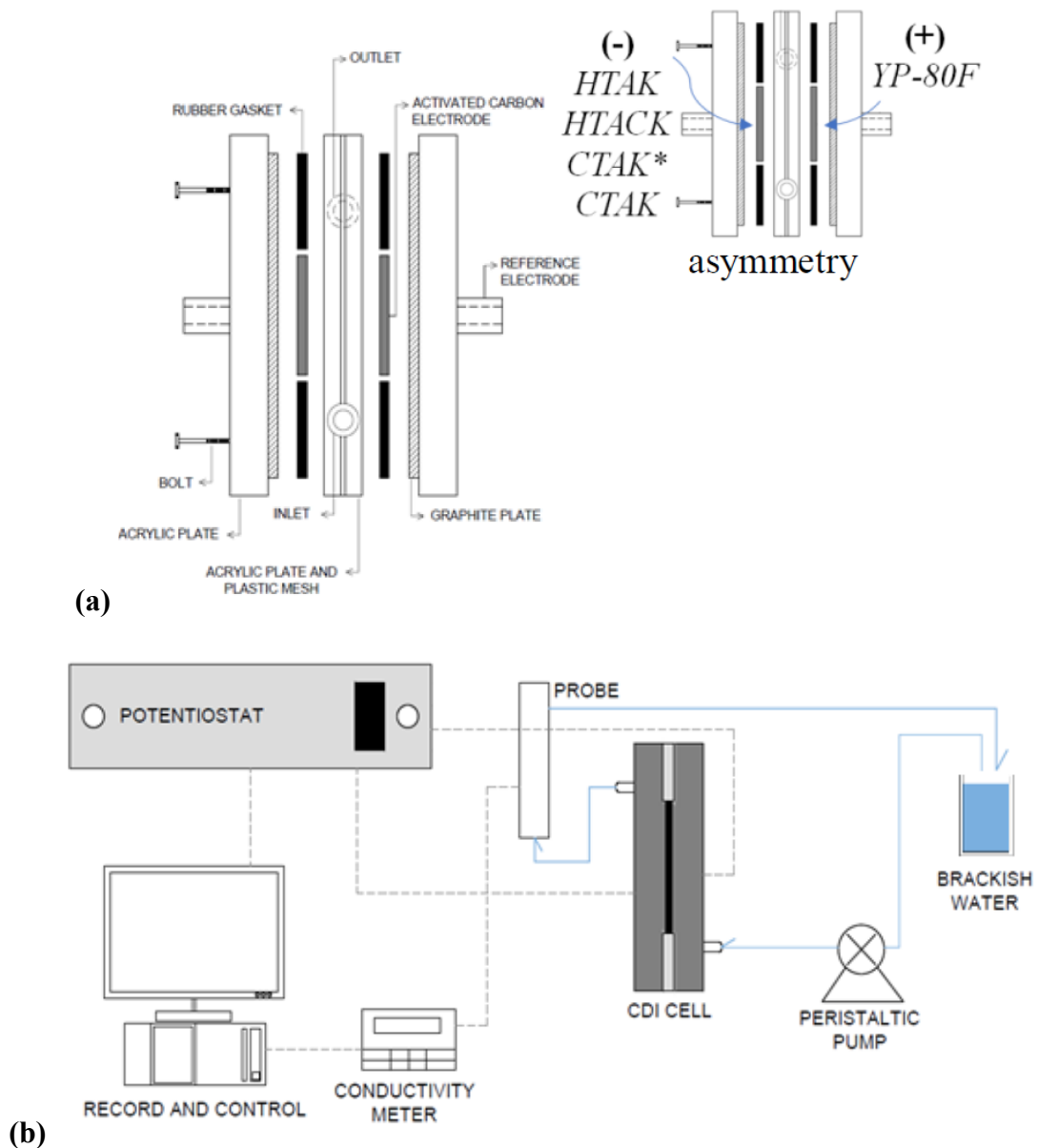
Figure 15. (a) CDI cell used in this work (adapted from Zornitta et al. [71]), indicating the asymmetric configuration, and **(b)** experimental system [16].

The positive and negative electrodes were arranged in symmetric and asymmetric configurations. The asymmetry was established considering the relative position of E_{pzc}. For the desalination assays, a 25 mL volume of 0.01 mol L^{-1} NaCl solution was recirculated through the CDI cell at a constant flow rate (26 mL min^{-1}) [10], using a peristaltic pump (Masterflex L/S, Cole-Parmer) (Figure 15(b)). A potentiostat (PGStat 204, Autolab) was used to apply 1.2 V and 0.0 V during the electrosorption and desorption steps, respectively. The desalination was carried out over 20 electrosorption/desorption cycles, in order to ensure the steady-state

condition, reached after the fifth cycle. Conductivity, pH, and temperature were continuously monitored in the outlet of the cell (Seven Excellence instrument, Mettler-Toledo). The conductivity value was corrected considering the pH and temperature fluctuations during the experiment, according to the methodology described by Lee et al. [134]. The variation in NaCl concentration over time was measured indirectly from the conductivity data using a calibration curve (Figure A1 in the Appendix).

Salt adsorption capacity (SAC), charge efficiency (Q_E), specific energy consumption (η), and average salt adsorption rate (ASAR) calculated using Eqs. (3), (4), (5), and (6), respectively, were used as the metrics to evaluate the desalination performance of the electrode. In these equations, C_0 is the initial salt concentration (mg L^{-1}), C_t is the salt concentration (mg L^{-1}) at time t (s), V is the electrolyte volume (L), m_E is the total mass of the active material in both electrodes (g), z is the ion valence, F is the Faraday constant (96,485 A s mol^{-1}), I is the current (A), M_{NaCl} is the molecular weight of NaCl (58,400 mg mol^{-1}), E_{cell} is the cell potential in the electrosorption step (V), m_{rem} is the mass of ions removed from the solution (mg), and t_c is the charging time (s).

$$SAC = \frac{(C_0 - C_t) \cdot V}{m_E} \tag{3}$$

$$Q_E = 100\frac{z.F.V.(C_0 - C_t)}{M_{NaCl}\int Idt} \tag{4}$$

$$\eta = \frac{E_{cell}\int Idt}{m_{rem}} \tag{5}$$

$$ASAR = \frac{SAC}{t_c} \tag{6}$$

The overall performance of the electrodes in the different configurations was evaluated according to the optimized salt removal (OSR) approach, proposed by Zornitta and Ruotolo [17], for simultaneous analysis of the electrosorption capacity and the adsorption/desorption kinetics. The OSR value (mg g^{-1} day^{-1}) is the amount of salt removed per gram of electrode material considering an operational time (t_{op}) of one day. In brief, the electrosorption (k_e) and desorption (k_d) rate constants were fitted according to a pseudo first-order model (Eqs. (7) and (8), respectively), where $mSAC$ is the maximum value of SAC. The optimized electrosorption time (t_e) was evaluated by deriving the amount of salt removed, m_{sr} (Eq. (9)), and making it

equal to zero. The desorption time (t_d) was calculated considering 99% of the electrode regeneration. The *OSR* value were calculated by replacing t_e in Eq. (9). This analysis is crucial for electrode evaluation, due to the influence on water productivity, since the electrosorption and desorption times affect the number of cycles performed.

$$SAC' = mSAC - SAC(t) = mSAC \cdot \exp(-k_e \cdot t_e) \tag{7}$$

$$SDC' = mSAC - SDC(t) = mSAC \cdot \exp(-k_d \cdot t_d) \tag{8}$$

$$m_{sr} = \frac{t_{op} \cdot m_E \cdot mSAC}{t_e + t_d}[1 - \exp(-k_e \cdot t_e)] \tag{9}$$

CHAPTER 4

RESULTS AND DISCUSSION

This chapter presents and discusses the results obtained for the electrochemical desalination of brackish water using a chloride-doped polyaniline activated carbon electrode modified with Pluronic^{TM}, in an electrochemical flow cell operating in batch mode. In a first step, there is a brief discussion about the yields of polymerization, hydrothermal and thermal carbonization, physical and chemical activations, and overall. In a second step, the results obtained from the structural characterization of activated carbons and the electrochemical characterizations of the electrodes are discussed. Subsequently, the results of desalination performance are discussed, mainly in relation to the salt adsorption capacity, electrosorption/desorption kinetics, charge efficiency and specific energy consumption. Finally, a comparison of desalination performance with works in the literature is provided.

The polymerization yields (Y_{PAni}) in the presence and absence of PLR were very similar (1.1 and 1.2 g PAni/mL aniline, respectively), indicating that PLR only acted as a templating agent and was not incorporated into the polymer. After hydrothermal carbonization, the yield decreased to 0.71 g char/g PAni, due to the release of volatile compounds, which the reduction increased when the thermal treatment was applied, leading to a lower yield (Y_{TC}) of 0.58 g char/g PAni. In the case of the thermally treated samples (CTAK* and CTAK), the Y_{TC} values were very similar (0.50 and 0.48, respectively), reinforcing that the template had not been incorporated into the precursor. The activation yield (g AC/g char) was calculated after physical activation using CO_2 (Y_{Ph}) or chemical activation with KOH (Y_{Ch}). The yields (Table 2) indicated a marked difference in the chemical reactions involved in these two activation processes, since Y_{Ch} was approximately 60% lower than Y_{Ph}. The lower release of volatile compounds during physical activation was expected to have a strong impact on *SSA* and pore formation, which was further evaluated using the N_2 adsorption/desorption isotherms. The decrease in the volatile content during carbonization affects the porosity development, increasing fixed carbon content, and decreasing H/C and O/C ratios. On the other hand, during the activation step, the fixed carbon is consumed widening the pores [135,136] and releasing volatile compounds due to the reaction between the carbonized precursor and KOH, consequently, forming large cavities [11]. Another noteworthy feature was an increase of Y_{Ch} when PLR was used in the polymer synthesis (from 0.16 to 0.37 g AC/g char, for CTAK* and CTAK, respectively). As mentioned previously, the PLR was practically not incorporated into

the polymer, so this trend was an indication that PLR changed the PAni structure and the textural properties of the carbonized samples. Changing in the pore morphology by adding F127 during the N-doped mesoporous carbons preparation was also reported by Xin et al. [20].

Table 2. Mass yields of polymerization (Y_{PAni}), hydrothermal (Y_{HC}) and thermal (Y_{TC}) carbonizations, physical (Y_{Ph}) and chemical (Y_{Ch}) activations, and overall yield (Y_0)

Material	Y_{PAni} (g_{PAni}/mL aniline)	Y_{HC} (g Char/g PAni)	Y_{TC} (g Char/g PAni)	Y_{Ph} (g AC/g char)	Y_{Ch} (g AC/g char)	Y_O (g AC/g PAni)
CTAK*	1.2	-	0.50	-	0.16	0.08
CTAK	1.1	-	0.48	-	0.37	0.18
HTAC	1.1	0.71	0.58	0.93	-	0.38
HTAK	1.1	0.71	0.58	-	0.37	0.15
HTACK	1.1	0.71	0.58	0.93	0.37	0.14

In summary, the polymerization, carbonization, and especially activation significantly influenced the overall yields (Y_O, Table 2), expressed in g of AC produced per g of PAni. The highest Y_O (0.38 g AC/g PAni) was observed for the physically activated sample (HTAC), while the lowest value was observed for CTAK* (0.08 g AC/g PAni). The other chemically activated samples displayed Y_O values varying from 0.14 to 0.18 g AC/g PAni, which were higher than the values observed using the precursor synthesized in the absence of PLR (CTAK*). There was also an influence of the carbonization heating rate on Y_O, reaching 0.08 g AC/g PAni in this work, while Zornitta et al. [10] obtained 0.16 g AC/g PAni for PAC/Cl in the absence of PLR, applying a heating rate (10 °C min^{-1}) 10-fold higher than employed in the present work.

4.1 Activated carbon characterization

4.1.1 Structural characterizations

PLR has been used in previous studies to template different materials, such as carbon molecular sieves [137,138]. The hypothesis adopted here was that by introducing PLR into the synthesis process, it would be possible to induce more organized mesoporous structures using hydrothermal syntheses. Nevertheless, the success of this approach was not evident from the results. The HRTEM micrograph (Figure 16(a)) showed that the HT sample presented a three-dimensional hierarchical pore network, with a graphitic pattern ($I_D/I_G = 0.999$), as indicated by

the Raman spectrum (Figure 16(d)). This structure was maintained even after CO_2 activation (HTAC), although becoming a more organized structure with mesopores (Figure 16(b)). Considering that $I_D/I_{G\ (HT)} > I_D/I_{G\ (HTAC)}$, the structure became more organized after physical activation, in agreement with the HRTEM images (Figures 16(a) and 16(b)). It should also be considered that the lower CO_2 reactivity, despite promoting the high Y_O observed for HTAC, might not promote the occurrence of oxygen groups on the edges of the graphitic basal planes, so a decrease of wettability would be observed. On the other hand, the chemical activations were associated with higher reactivity with carbon, which should lead to a material with a greater quantity of surface functional groups. In this case, lower activation yields and graphitization degrees (for example, $I_D/I_{G\ (HTAK)} > I_D/I_{G\ (HTAC)}$) were detected.
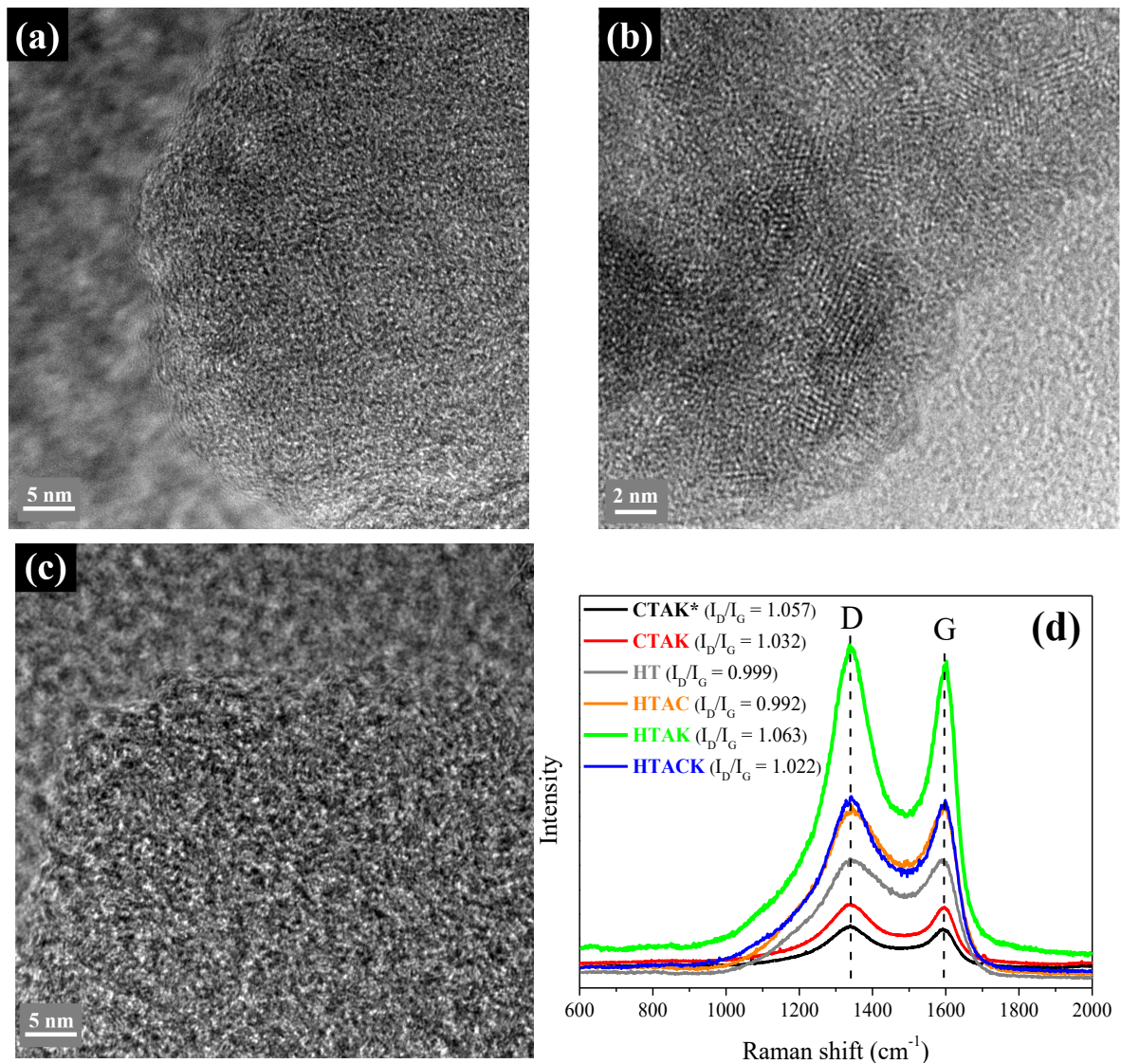
Figure 16. HRTEM images of HT **(a)**, HTAC **(b)**, and HTACK **(c)**; **(d)** Raman spectra of the samples.

As an attempt to introduce more oxygen groups and make the HTAC electrode more hydrophilic, a further activation with KOH was performed, obtaining the HTACK material. As expected, the graphitization degree decreased for HTACK (I_D/I_G = 1.022, Figure 16(d)), since the chemical activation enhanced the content of non-graphitic carbon (D band), probably due to the introduction of surface oxygen groups on the edges of graphitic basal planes. This trend became more evident for HTAK (I_D/I_G = 1.063). Regarding the pore structure, the HRTEM image of HTACK (Figure 16(c)) revealed that the organized structure of HTAC was lost after its chemical activation, with HTACK presenting a 3D structure similar to that of HT, while high mesoporosity was preserved.

The contact angle analyses (Figure 17) revealed that the chemical treatment resulted in the hydrothermally treated carbons presenting a lower contact angle, due to the increased SOG content (discussed below). Hence, the HTACK electrode became more hydrophilic (θ = 76°) than HTAC (θ = 102°), while the difference became even more substantial for HTAK (θ = 47°). This trend is explained by the increase of the surface interactions with hydroxyl groups and the decrease of the interactions with methyl groups [139], along with the improvement of surface area of the char, by reducing the porosity concentration towards the center of particles during carbonization [140]. This higher wettability was expected to improve the desalination performance, which was subsequently confirmed (discussed below).
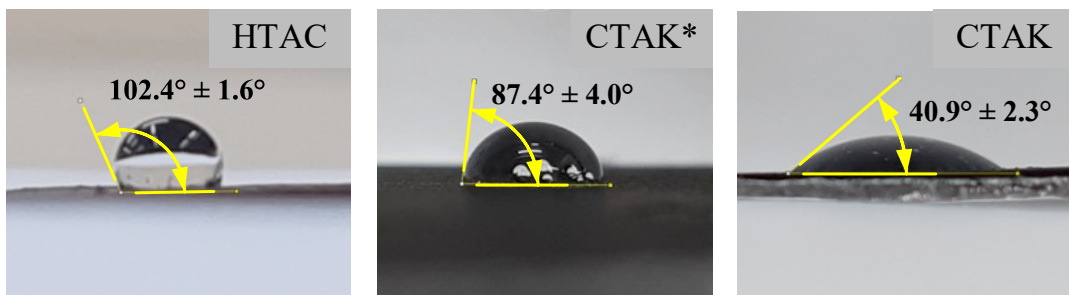
Figure 17. Contact angles of the HTAC, CTAK*, and CTAK electrodes measured by sessile drop method after 10 s.

XRD analyses were performed to obtain additional insights about the activated carbon structure. In previous work using polyaniline activated carbons, it was demonstrated that a turbostratic carbon structure (Figure 18(a)), composed of microcrystalline carbon fragments, was formed at low carbonization temperature (500 °C). This structure provides an open framework with surface groups at the edges of the graphite basal planes, which improved the reactivity during the activation step, when compared with graphitic carbon [11]. In the present

work, the XRD patterns of the HT, CT, and CT* samples (Figure 18(b)) showed no evidence of turbostratic carbon ($2\theta = 20.7°$), as expected, since all the samples were carbonized at 800 °C. For these samples, broad diffraction bands at 24.5° and 44.4° were found, assigned to graphitic structures. It should be noted that after activation, the samples became less crystalline (Figure 18(c)), with the exception of HTAC, for which the XRD pattern was the same as after carbonization (HT). This behavior was further evidence of low CO_2 reactivity leading to lower SOGs content, based on the high hydrophobicity of this material (Figure 17).
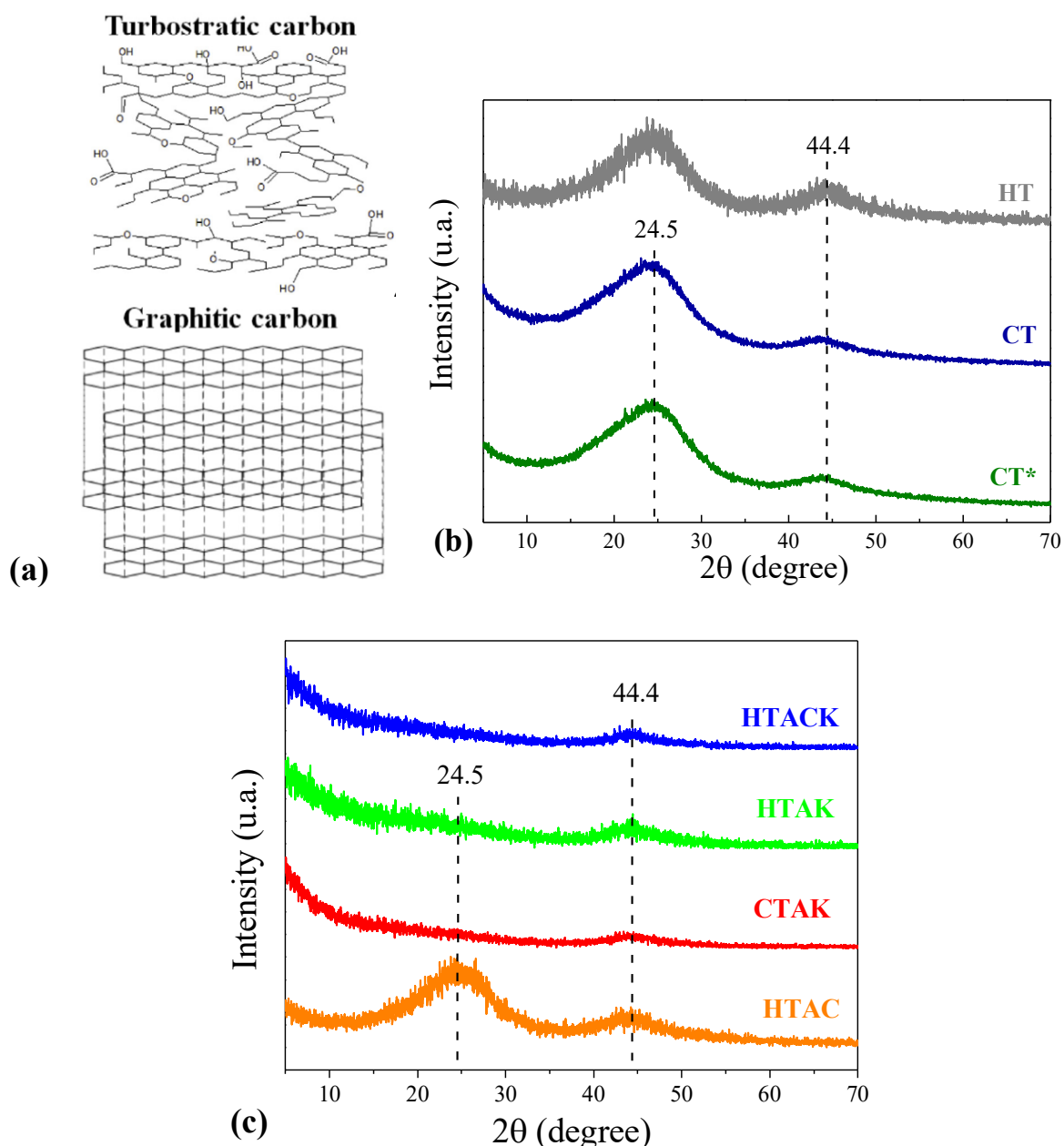
Figure 18. (a) Turbostratic and graphitic carbon structures. XRD patterns of the carbonized **(b)** and activated **(c)** samples.

FTIR analysis was performed to obtain information about the surface groups present. Figure 19(a) shows a comparison of the spectra for HTAK and CTAK, where broad bands in the regions 673-1396 cm^{-1} (HTAK) and 690-1404 cm^{-1} (CTAK) were observed, related to surface oxygen groups [141]. These bands are usually attributed to C-O stretching in ether or carboxylic groups, C-OH stretching in alcohols or phenolic groups (only phenolics in CTAK), carbonates, carboxyl-carbonates, and C=O stretching in carboxylic acids, lactones, or carboxylic anhydrides. These bands may also be attributed to the overlapped signatures of C-C stretching and twisting [142–144], as well as to C-H bonds of aromatic and heteroatomic species [145,146]. In addition, a broad band in the region 1396-1655 cm^{-1} corresponded to the overlapped signatures of C-C bonding in the aromatic ring [146], C=C stretching of the benzenoid and quinoid rings [147], conjugated C=C stretching in olefinic species (C=C-O) [148], ceto-enol groups, carbonates, carboxyl-carbonates, and stretching of carbonyl groups [141]. Carbonyl groups such as carboxylic acids, lactones, or carboxylic anhydrides were present in both materials, associated with C=O stretching at 1655-1971 cm^{-1} [141]. A band at 2366-2590 cm^{-1} indicated the presence of phenolic groups and carboxylic acids, associated with C-OH and C=O stretching, respectively [141]. A band at 2561-2920 cm^{-1} was related to C-H stretching, C-OH stretching in phenolic groups, C=O stretching in carboxylic acids, and CH$_3$-O group vibration [149]. A weak band at 3117-3232 cm^{-1}, which was only detected in the CTAK spectrum, was attributed to stretching of C-OH in alcohols or phenolic groups, C=O stretching in carboxylic acids, or adsorbed water [150]. HTAC presented a similar spectrum (Figure 19(b)), with an additional band at 2471-2851 cm^{-1} corresponding to the C-H stretching vibration mode. These results were a good indication that activation promoted the formation of SOGs, which were expected to improve the electrochemical properties of the electrodes and their desalination performance.

(a)

(b)
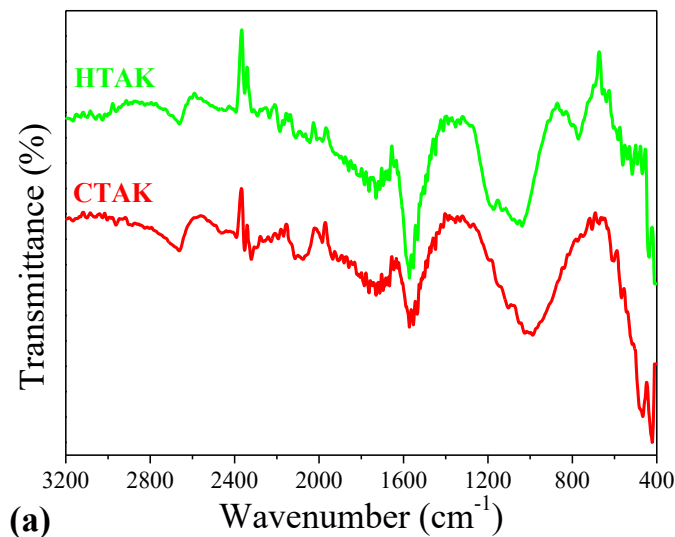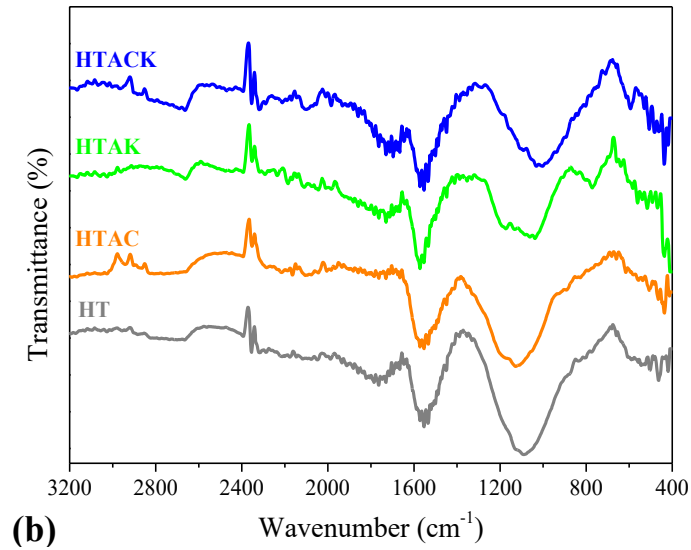
Figure 19. FTIR spectra comparing CTAK and HTAK **(a)** and hydrothermally carbonized/activated **(b)** samples.

The bulk and surface (< 5 nm) elemental compositions of the ACs, determined by elemental microanalysis and quantitative XPS, are shown in Table 3 and Table 4, respectively. All the PAC/Cl samples were mainly composed of carbon and oxygen, with a negligible content of nitrogen in the bulk material. The XPS survey spectra (Figure 20) revealed the presence of only carbon and oxygen surface groups. Nitrogen surface groups were not detected, indicating that the N content from polyaniline was released during the chemical activation at high temperature [10]. According to our previous results [10], practically all chloride is released after carbonization and activation with KOH, as confirmed by XPS analysis (Figure 20).

Table 3. CHNS elemental analysis of the activated carbons

Material	Elemental composition (at.%)				
	C	**H**	**N**	**S**	**O**
CTAK*	93.0	1.1	0.8	0	5.1
CTAK	86.9	3.9	0.3	0	8.9
HTAK	91.1	0.3	0.7	0	7.9
HTACK	93.4	0.3	0.5	0	5.8

Table 4. Elemental composition of the near-surface region, obtained from XPS survey spectra, and surface groups determined from the deconvoluted high resolution XPS C 1s and O 1s spectra

	Material	CTAK*	CTAK	HTAK	HTACK
Surface elemental composition (at.%)	C 1s	95.8	94.7	94.3	94.5
	O 1s	4.2	5.3	5.7	5.5
C 1s surface groups (at.%)	O-C-OH / O-C=O	18.0	19.4	16.3	18.8
	C=O / C-O / C-OH / C-O-C	14.7	14.2	16.8	14.4
	C-H / C-C$_{arom}$	66.0	65.8	66.0	62.0
O 1s surface groups (at.%)	O-C-OH	17.2	26.2	17.6	13.5
	C-O / C-OH / C-O-C / O-C=O	64.1	63.9	56.7	46.9
	C=O	18.7	9.9	25.7	39.6
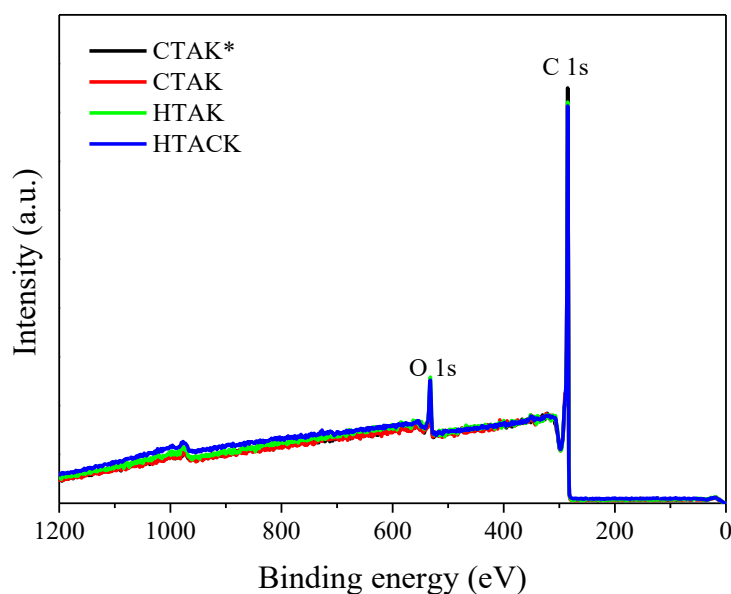
Figure 20. XPS survey spectra for the CTAK*, CTAK, HTAK, and HTACK.

Figure 21 shows the deconvoluted XPS core-level O 1s spectra, where the presence of carbonyl (C=O) groups (531.0 eV [151,152]) can be seen for all the samples, especially HTACK (39.6 at.%, Table 4). The band at 533.0 eV corresponds to the overlapped signatures for alcohol/ether (C-O), phenolic (C-OH), ether (C-O-C), and carboxyl (O-C=O) groups. The binding energy at 536.0 eV could be attributed to carboxylic (O-C-OH) groups [153], where CTAK and HTACK presented the highest (26.2 at.%) and lowest (13.5 at.%) contents, respectively. Compared to CTAK*, CTAK had 1.9-fold less carbonyl groups and 1.5-fold more

carboxylic groups. Although carbonyl groups are reported to be electrochemically inactive, they can shift the E_{pzc} [154]. Acid groups, such as phenolic and carboxylic, give the material its polar character, making the electrode hydrophilic [155]. The same trend was observed from analysis of the C 1s XPS spectra (Figure 22). The peaks were centered at 284.6 eV (C-H / C−C aromatic [156]), 286.3-287.1 eV (C=O [157] / C-O [158] / C-OH / C-O-C [152]), 289.3-290.4 eV ($\pi \rightarrow \pi*$ transitions [159] / O-C-OH [10] / O-C=O [152]), and 292.0-294.7 eV (K $2_{p3/2}/2_{p1/2}$ spin-orbit pair [10], indicating traces of potassium from the chemical activation process). According to the XPS analysis (Table 4), the SOGs content varied from 4.2 to 5.7 at.%. The use of PLR increased the SOGs content in CTAK by 26%, compared to CTAK*, which would be expected to influence the carbon wettability, E_{pzc}, and, consequently, the electrosorption performance.
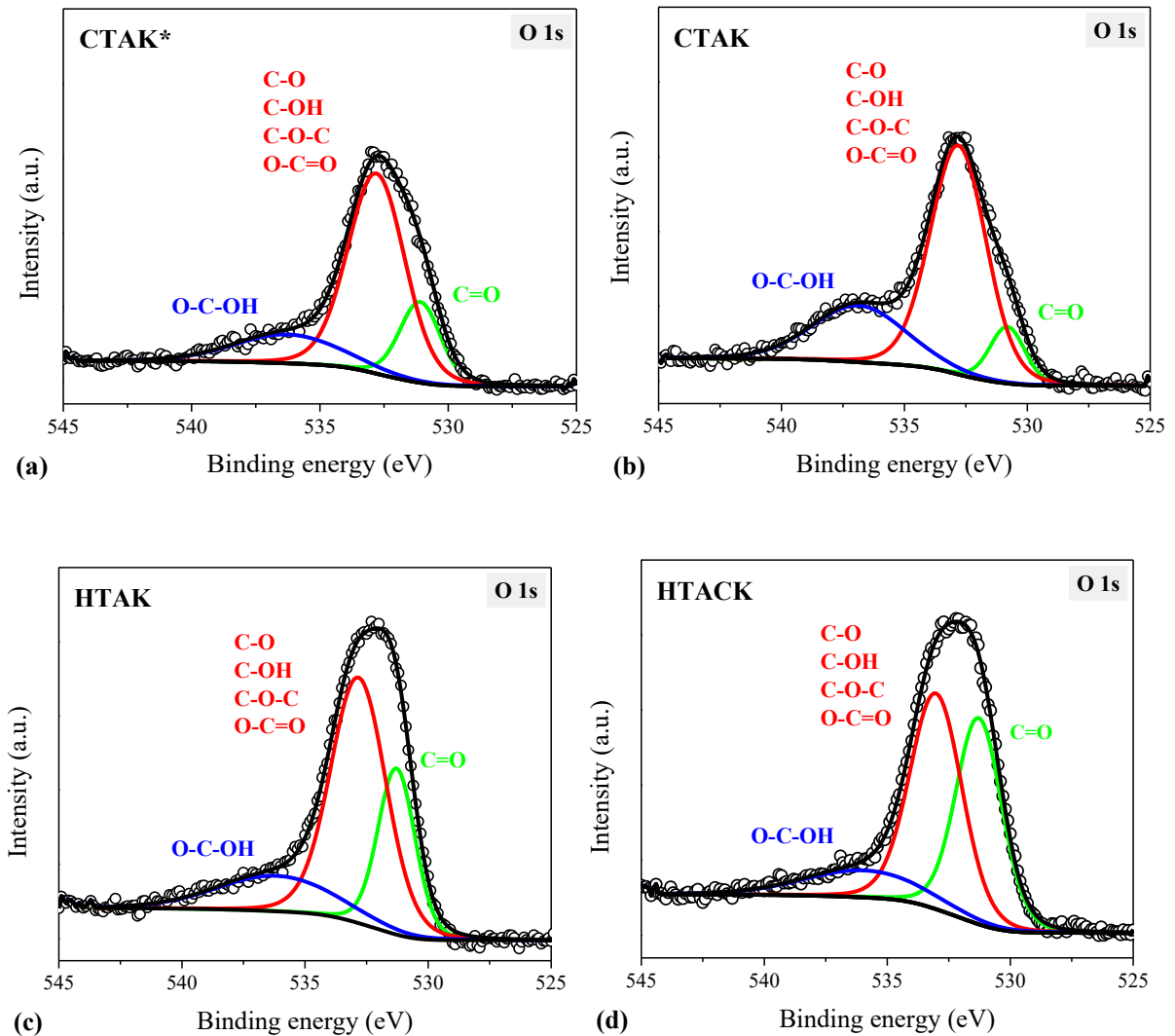
Figure 21. Deconvoluted high resolution XPS O 1s spectra of CTAK* **(a)**, CTAK **(b)**, HTAK **(c)**, and HTACK **(d)**.
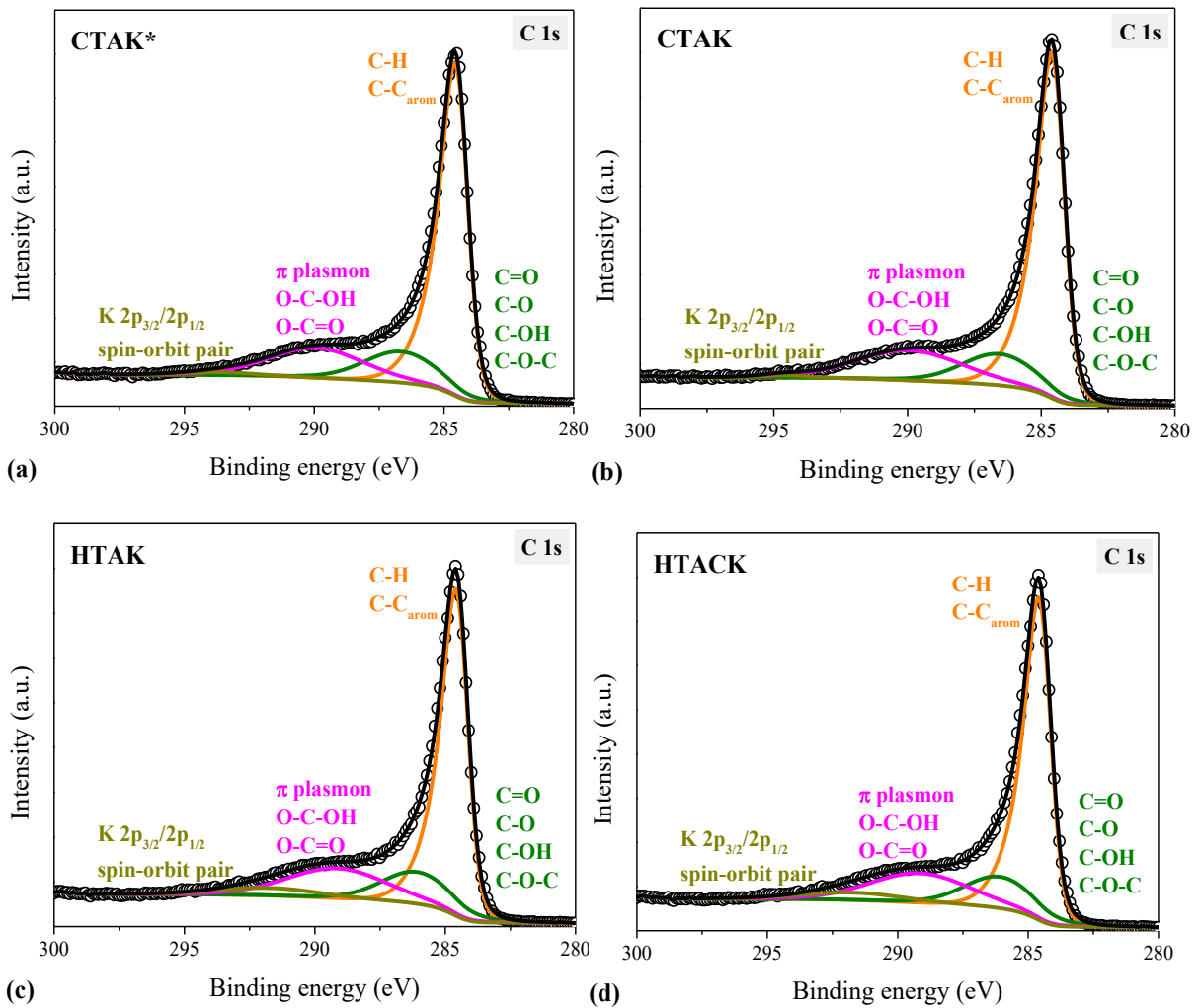
Figure 22. Deconvoluted high resolution XPS C 1s spectra of CTAK* **(a)**, CTAK **(b)**, HTAK **(c)**, and HTACK **(d)**.

In order to understand the influence of PLR on the textural properties of the samples, *SSA* and PSD were determined from the N_2 adsorption/desorption isotherms (Figure 23(a)). The type I isotherms indicated that the ACs were predominantly microporous (< 2 nm), while the type II isotherms with H4-type hysteresis loop could be attributed to mesoporosity (pore width > 2 nm), according to the IUPAC classification [160]. The textural parameters of the samples, calculated from the isotherms, are summarized in Table 5, together with the textural properties of the YP-80F used in asymmetric configurations. The data revealed that the use of PLR promoted a decrease of the mesoporosity from 57.2% (CTAK*) to 43.1% (CTAK), leading to a more microporous carbon, consequently enhancing SSA_{BET} by 10%. The isotherms also showed that the volume adsorbed by the physically activated sample (HTAC) increased significantly after the chemical activation with KOH (HTACK), indicating further development

of the electrode porosity. The *SSA* varied from 489 m^2 g^{-1} for the CO$_2$-activated sample to 3148 m^2 g^{-1} for HTACK. A large increase (6.4-fold) in the *SSA* of the HTAC material was achieved after chemical activation with KOH (HTACK), while the high mesoporosity was preserved (45.3 *%V$_{mes}$*, Table 5), corroborating the HRTEM results.
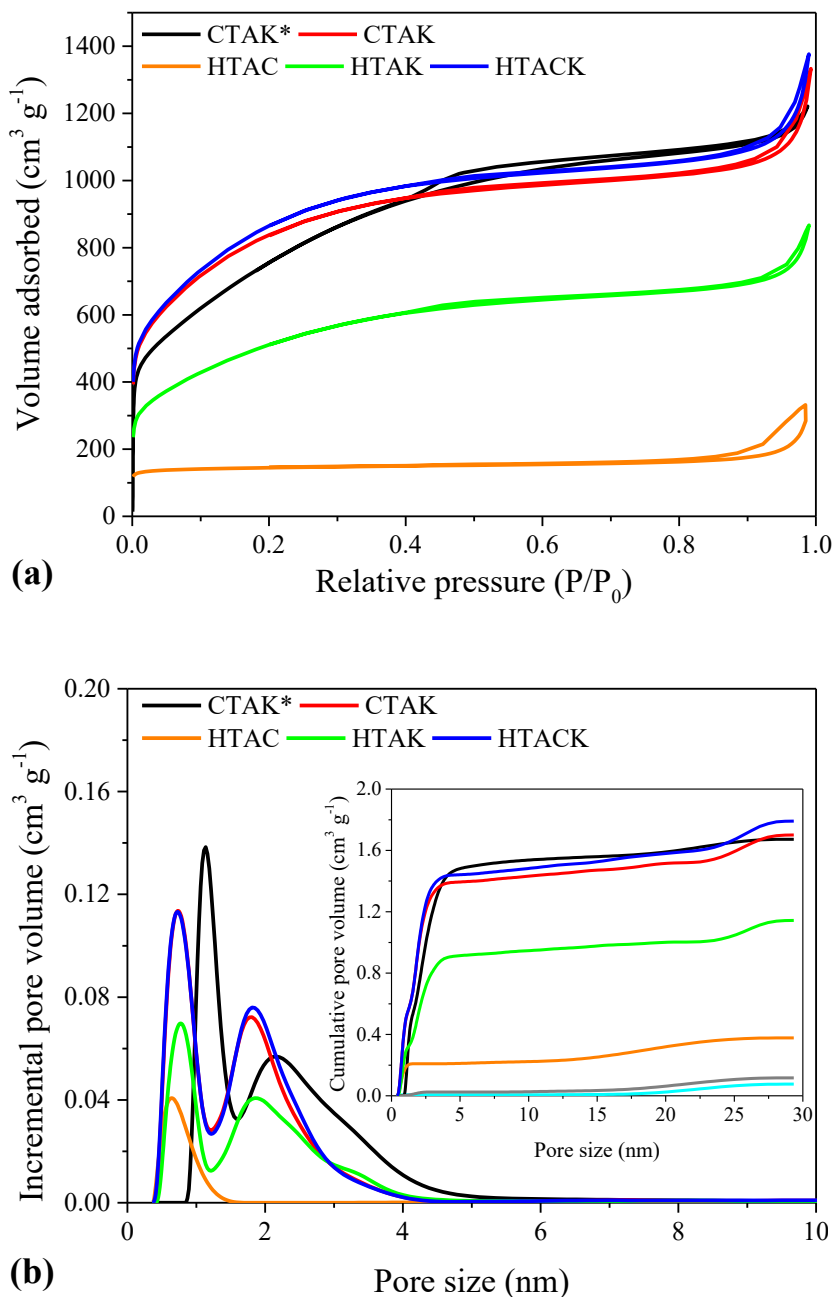
Figure 23. Nitrogen adsorption/desorption isotherms **(a)** and pore size distributions **(b)** of the ACs. Inset: cumulative pore volume.

Table 5. Textural analysis of the electrodes, obtained from the N_2 adsorption/desorption isotherms

Material	SSA_{BET} (m² g⁻¹)	V_T (cm³ g⁻¹)	V_{mic} (cm³ g⁻¹)	V_{mes} (cm³ g⁻¹)	$\%V_{mes}$	d_{50} (nm)
CTAK*	2756	1.71	0.73	0.98	57.2	2.2
CTAK	3035	1.70	0.97	0.73	43.1	1.8
HTAC	489	0.38	0.21	0.17	44.7	1.1
HTAK	1862	1.14	0.54	0.60	52.8	2.1
HTACK	3148	1.79	0.98	0.81	45.3	1.9
YP-80F [68]	2591	1.19	0.81	0.38	31.8	1.58

Notes: Specific surface area (SSA_{BET}); total pore (V_T), micropore (V_{mic}), and mesopore (V_{mes}) volumes; percentage of mesopores ($\%V_{mes}$); average pore diameter (d_{50}).

The type of activation employed is related to the development of pores and *SSA*. Physical activation using CO_2 generates a more mesoporous structure, formed from the fast reaction between carbon and CO_2 at high temperatures, based on the Boudouard equilibrium (Eq. 10), in with the $CO_{(g)}$ produced is responsible for the pore enlargement [161–163]. On the other hand, the chemical activation using KOH leads to a large loss of volatiles, producing microporous activated carbons with higher *SSA* and pore volume [11,12]. According to Eq. 11, the carbon oxidizes to form carbonates and metallic potassium. The porosity is developed during activation due to the mobility of the metallic K within the structure, enlarging the pores, and the reaction between potassium carbonate and the carbon (Eq. 12), increasing the carbon burn off [164]. Concomitantly, the production of larger SOG content is expected [55], impacting the carbon hydrophilicity.

$$C_{(s)} + CO_{2(g)} \leftrightharpoons CO_{(g)}; \ T > 700\,°C \tag{10}$$

$$6KOH_{(s)} + C_{(s)} \rightarrow 2K_{(s)} + 3H_{2(g)} + 2K_2CO_{3(s)}; \ T > 630\,°C \tag{11}$$

$$K_2CO_{3(s)} + 2C_{(s)} \rightarrow 2K_{(s)} + 3CO_{(g)}; \ T = 760\,°C \tag{12}$$
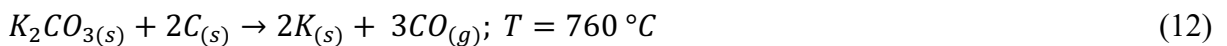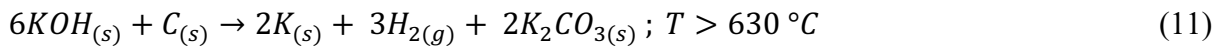
Comparing CTAK and HTACK, the *SSA* increased by only 3.7% when physical and chemical activation were combined, while similar $\%V_{mes}$ and d_{50} were obtained. The *SSA* values for the carbonized samples, CT and HT, were very low (24 and 65 m² g⁻¹, respectively),

confirming that activation was essential for obtaining carbons suitable for CDI. The PSD (Figure 23(b)) confirmed the presence of a large volume of mesopores, occupying between 43.1 and 57.2% of the total pore volume.

Finally, it is worth noting that the PAC/Cl synthesized in the absence of PLR (CTAK*) in this work, despite presenting similar SSA, had a $\%V_{mes}$ 2.5-fold higher than obtained for the same material by Zornitta et al. [10] (2652 m^2 g^{-1} SSA_{BET} and 23% V_{mes}). The increase of $\%V_{mes}$ obtained here could mainly be attributed to the slow carbonization heating rate used in this work (the other synthesis parameters were very similar).

4.1.2 Electrochemical characterizations

The electrochemical properties of the electrodes were characterized using an asymmetric configuration similar to the one subsequently tested in desalination experiments. The synthesized material was used as the working electrode, while the counter and reference electrodes were YP-80F carbon and Ag/AgCl, respectively. Figure 24(a) shows the polarization curve in terms of charge storage capacity, for the different electrodes. The quasi-rectangular shape of the voltammograms indicates the capacitive and conductive behavior of the electrodes, typical of supercapacitors. Deviation from such behavior, with distortion of the rectangular shape, usually indicates a resistive component of one of the electrodes, which here suggested that CTAK was more conductive than CTAK*. Figure 24(b) shows the Nyquist plots from which the ohmic (R_Ω) and charging resistances (R_{CT}) were determined by fitting the semicircle domain. The R_Ω value, attributed to the contact (current collector) and electrolyte resistances, were very similar (~0.4 Ω), as expected, since the same cell was used in all the experiments. The R_{CT} is an intrinsic property of the carbon electrode and was affected by the surface chemistry and polarization resistance of the electrodes. In this sense, the R_{CT} were 0.22, 0.18, 0.15, and 0.11 Ω for HTACK, CTAK*, CTAK, and HTAK, respectively. These values were similar and very low, when compared to other values reported in the literature, e.g., 0.46-1.05 Ω for PAC/PTS [16], 0.34 Ω for micro-meso-macroporous 3D graphene [165], and 0.83-36.7 Ω for polyglycerol activated carbon (PGAC) [6], indicating that the electrodes could be easily charged. The CTAK* electrode presented a significant decrease in the R_{CT} (98.8%), compared to the same material reported by Zornitta et al. [10] (14.7 Ω), which could be ascribed to the modification of the carbonization step, which impacts the AC structure, as previously discussed considering the Raman spectra.
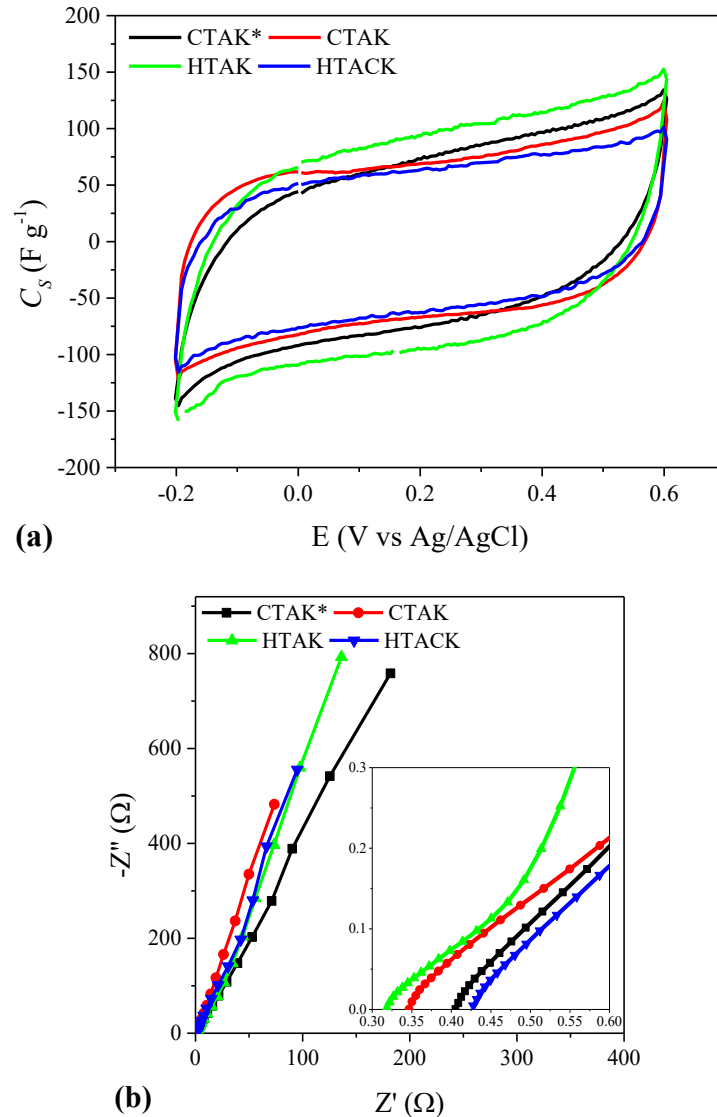
Figure 24. (a) Cyclic voltammograms of the electrodes (at 5 mV s^{-1}), and **(b)** Nyquist plots. Counter electrode: YP-80F. Electrolyte: 1.0 mol L^{-1} NaCl.

4.2 Desalination performance

The desalination performance was evaluated for both symmetric and asymmetric electrode configurations, in an attempt to improve the electrosorption rate by minimizing the effect of co-ion repulsion [103]. To this end, an analysis of E_{pzc} was performed to select the most suitable electrode configuration in the asymmetric CDI cell. The results (Figure 25(a)) indicated that the most appropriate configuration was an asymmetric cell with YP-80F as positive electrode [166] and the synthesized electrodes as cathodes. The reason for this selection was the presence of negative surface charges provided by the SOGs on the synthesized active materials, as confirmed by the XPS analysis, and the more basic character (~4.5-fold more basic

than acidic groups) of YP-80F, as reported in the literature [167]. As an example of this effect, Figure 25(a) shows how the high SOGs content (Table 4) shifted the E_{pzc} of the synthesized materials to higher values. In accordance with its lower SOGs content, CTAK* presented the lowest E_{pzc} (less negative surface charge) of the materials tested. It should also be noted that the HTAC electrode was not included in this analysis, despite its high mesoporosity (44.7%, Table 5) and organized structure (Figure 16(b)), because its significant hydrophobic behavior ($\theta = 102.4°$, Figure 17) meant that it was not considered a suitable candidate for use in the desalination experiments. This high contact angle could be attributed to the low SOGs content observed when physical activation was employed [55].
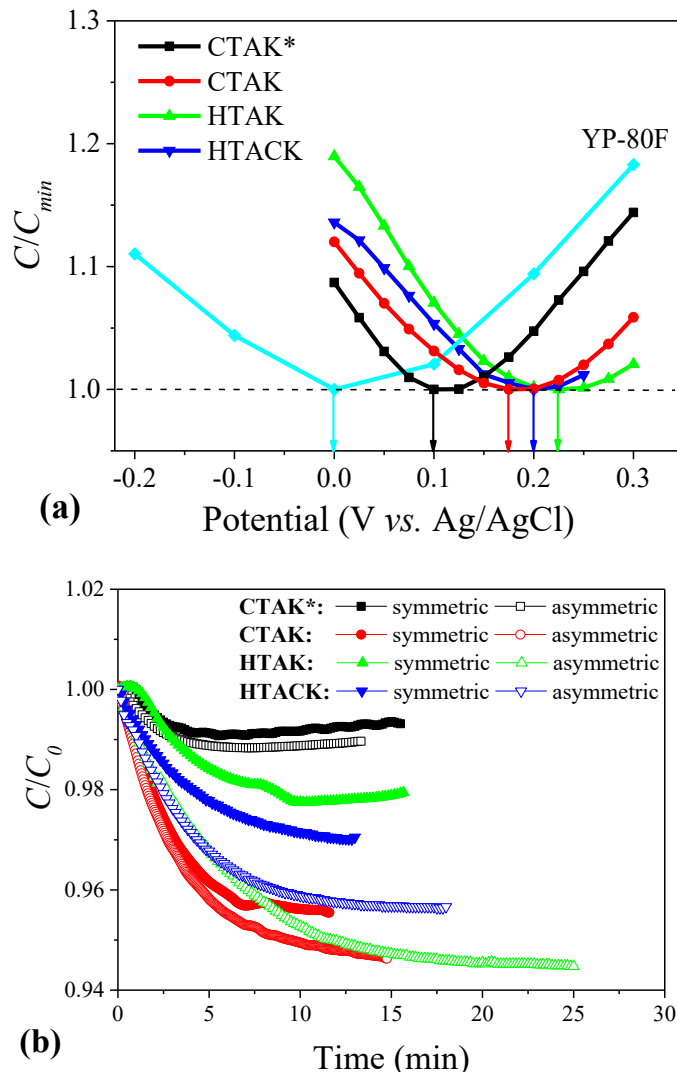
Figure 25. (a) Electrode E_{pzc} values and **(b)** electrosorption profiles of the electrodes in symmetric and asymmetric configurations, in the 5th cycle (constant after 20 cycles). Electrolyte: 600 mg L^{-1} NaCl; E_{cell}: 1.2 V (adsorption) and 0.0 V (desorption).

The results of the desalination experiments (Figure 25(b)), comparing CTAK and CTAK*, clearly demonstrated the positive impact on CDI performance of using PLR during the synthesis process. As a result, the *SAC* increased substantially from 6.7 to 11.4 mg g^{-1}, using the symmetric configuration (Figure 26(a)). Moreover, the use of an asymmetric CTAK|YP-80F configuration not only provided a significant increment of *SAC* (from 11.4 mg g^{-1} to 21.0 mg g^{-1}), but also an increment of 24% for Q_E (Figure 26(b)). This improvement confirmed the efficacy of this configuration for avoiding co-ion repulsion, consequently resulting in higher desalination capacity and lower specific energy consumption (29%, Figure 26(c)). Additionally, the results were in agreement with the XPS analyses (a large quantity of SOGs shifted E_{pzc} to a more positive value, 0.175 V *vs.* Ag/AgCl) and the lower hydrophobicity of this material ($\theta = 40.9°$, Figure 17). The presence of oxygen functional groups prevents the co-ion repulsion, improving the charging efficiency [11].
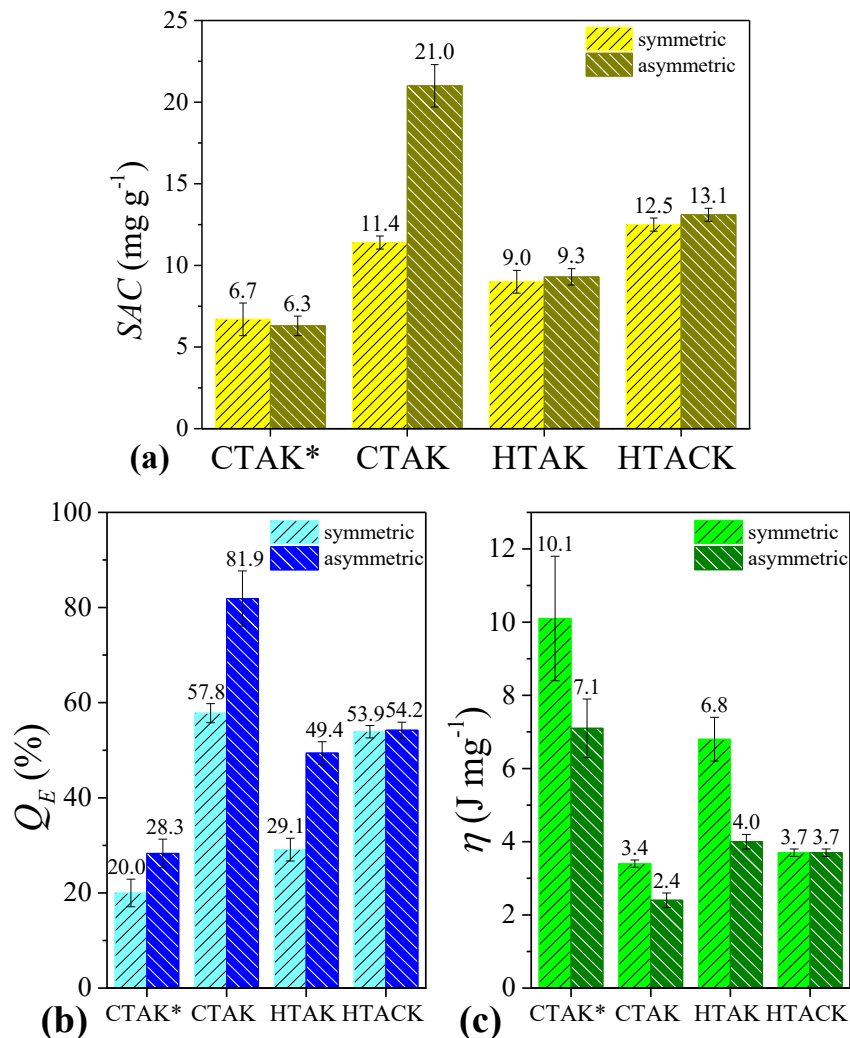
Figure 26. Desalination performance of the electrodes in symmetric and asymmetric configurations: **(a)** *SAC*, **(b)** Q_E, and **(c)** η.

As a contrast with the performance of the material prepared in the absence of PRL (CTAK*), the use of an asymmetric configuration CTAK*|YP-80F did not improve the desalination performance (6.3 mg g^{-1}), keeping the charging efficiency at very low values (a moderate increase from 20 to 28%). This could be attributed to the lower E_{pzc} (0.1 V *vs.* Ag/AgCl, Figure 25(a)), which resulted not only from the lower negative surface charge content of CTAK*, but also the type of functionalities. According to the XPS results, CTAK* had 1.9-fold more carbonyl groups, compared to CTAK, directly affecting the E_{pzc} shift [154]. Additionally, these functionalities contributed to the lower hydrophilicity of CTAK* ($\theta = 87.4°$) than CTACK ($\theta = 40.9°$), leading to the lower electrosorption values obtained for the material prepared in the absence of PRL [155]. It could be concluded from these results that PLR strongly influenced the polyaniline synthesis, by modification of the activation process, producing ACs with distinct surface chemistry that promoted the electrosorption of ions.

In comparison with the activation methodologies, it was found that the hydrothermally synthesized electrodes (HTAK and HTACK) employed in the symmetric configuration did not present any significant improvement, in terms of *SAC* (9.0 and 12.5 mg g^{-1}, respectively), compared to the thermally activated electrode (CTAK, *SAC* = 11.4 mg g^{-1}). As shown in Figure 26(a), use of the asymmetric configuration resulted in only slight increases of the *SAC* values (9.3 and 13.1 mg g^{-1} for HTAK and HTACK, respectively), relative to the symmetric configuration, which were far lower than the value obtained for CTAK (21.0 mg g^{-1}). The lower *SAC* observed for HTAK, compared to CTAK, could be attributed to its lower *SSA*. In the case of HTACK, despite having higher *SSA* (Table 5) and similar SOGs content (Table 4), compared to CTAK, the low content of surface polar groups (phenolic and carboxylic) made the electrode less hydrophilic and limited increase of the *SAC*, even using the asymmetric configuration. In addition to this, the Q_E values were lower, irrespective of the cell configuration, leading to a higher energy demand, compared to the CTAK electrodes.

For evaluation of the kinetics of the processes, the electrosorption and desorption constants were calculated (Figure 27), together with the *OSR* values (Table 6). The thermally activated carbons presented faster electrosorption kinetics, compared to the samples prepared using the hydrothermal method. For the CTAK electrode, a higher value of k_e was obtained for the symmetric configuration than for the asymmetric arrangement. This feature, which contrasted with the *SAC* values, could be ascribed to the lower $\%V_{mes}$ of YP-80F than CTAK (Table 5). The mesopores acted as large avenues for ion diffusion, with a high proportion of mesopores significantly influencing mass transfer. The correspondent ASAR values are also presented in the Table 6, in order to facilitate the comparison with results in the literature.

However, this metric only considers salt removal time, without taking the desorption time into account.
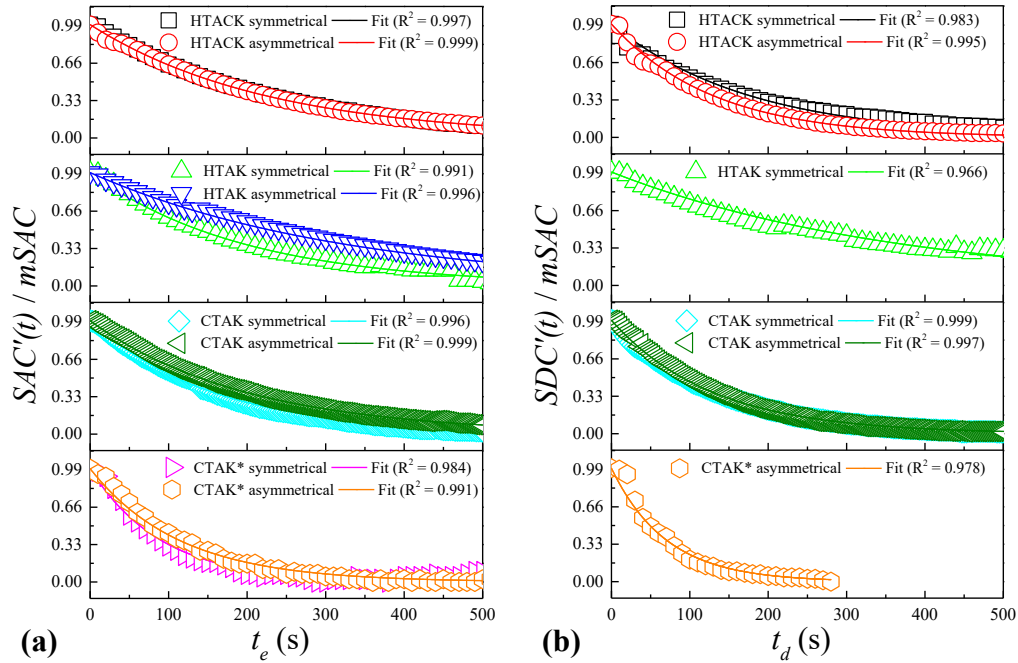
Figure 27. Normalized salt adsorption **(a)** and desorption **(b)** concentrations, as a function of electrosorption and desorption time, respectively. The lines represent the fits of the pseudo-first order models used to determine the kinetic constants of electrosorption (k_e) and desorption (k_d).

Table 6. Kinetics and OSR performances of the electrodes in symmetric and asymmetric configurations

Electrode configurations	$k_e \times 10^3$ (s^{-1})	$k_d \times 10^3$ (s^{-1})	t_e (s)	t_d (s)	N_{cycles}	OSR (mg g^{-1} day^{-1})	ASAR $\times 10^3$ (mg g^{-1} s^{-1})
CTAK* symmetric	11.7	-	369	890	78	479	7.4
CTAK* asymmetric	8.57	16.5	194	279	183	932	7.0
CTAK symmetric	6.28	7.88	299	585	98	945	15.8
CTAK asymmetric	4.90	7.64	361	603	90	1560	23.3
HTAK symmetric	5.12	-	963	1398§	47	378	5.0
HTAK asymmetric	3.19	4.97	525	926	60	450	6.2
HTACK symmetric	4.51	5.72	415	806	71	752	16.0
HTACK asymmetric	4.31	7.26	392	634	85	901	12.1

Notes: Electrosorption (k_e) and desorption (k_d) kinetic constants; optimized electrosorption time (t_e); desorption time (t_d); number of cycles ($N_{cycles} = t_{op}.(t_e + t_d)^{-1}$); optimized salt removal (OSR); and average salt adsorption rate (ASAR). § time considering 99% desorption.

An interesting observation for the CTAK* electrode was that the SAC (6.7 mg g^{-1}) was similar to the value reported earlier [10] for PAC/Cl (5.8 mg g^{-1}, Table 7), even though a slower carbonization heating rate was used for CTAK*. However, the modification appeared to have a strong influence on increasing $\%V_{mes}$ for CTAK* (57.2%), compared to PAC/Cl (23%), resulting in a 3.5-fold enhancement of the electrosorption kinetics.

Contrary to the initial hypothesis, the HTAK and HTACK electrodes presented slower rates of electrosorption and desorption, compared to the thermally carbonized samples (CTAK), for both symmetric and asymmetric configurations (Table 6). This indicated that the use of PLR in combination with hydrothermal carbonization, despite leading to a three-dimensional hierarchical structure with similar textural properties in terms of $\%V_{mes}$ and d_{50}, did not positively affect the process kinetics. Furthermore, these results suggested that the 3D arrangement of the PLR-hydrothermally carbonized samples was probably the most important factor affecting pore tortuosity and the diffusion path into the micropores [168,169]. In summary, the combination of the values of SAC, k_e, and k_d resulted in the HTAK and HTACK electrodes presenting the worst performances in terms of OSR. This outcome evidenced that hydrothermal carbonization, besides being time-consuming and increasing the preparation cost, would not be recommended, since it did not bring any advantage in terms of desalination performance.

Overall, for CTAK, balancing the positive effect on SAC and negative effect on the kinetics, an outstanding OSR value of 1560 mg g^{-1} day^{-1} was obtained, which was even higher than obtained in previous work using PAC/PTS (Table 7). Therefore, it could be considered that the main goal of this work was achieved by introducing PLR into the PAni synthesis, obtaining a cost-effective PAC electrode by replacing PTS$^-$ with chloride as the doping anion during AC preparation. In comparison with other similar ACs reported in the literature (Table 7), the values obtained using CTAK in a membraneless cell revealed the excellent potential of this material for use in capacitive deionization.

Finally, a comparison of the CDI performance using the CTAK with other activated carbon electrodes is shown in Table 8. Although SAC varied from 3.5 to 27.1 mg g^{-1}, a superior OSR value was obtained in this work (1560 mg g^{-1} day^{-1}), except for the value obtained by Choi and Yoon [170] (2072 mg g^{-1} day^{-1}) using membrane CDI, but it is worth mentioning that the use of membrane imposes an additional cost.

Table 7. Comparison of different polyaniline activated carbons (E_{cell} = 1.2 V, 600 mg L^{-1} NaCl)

Material	SSA_{BET} (m^2 g^{-1})	Configuration	SAC (mg g^{-1})	k_e ×10^3 (s^{-1})	OSR (mg g^{-1} day^{-1})	η (J mg^{-1})	Reference
CTAK*	2756	Symmetric	6.7	11.7	479	10.1	This work
CTAK	3035	Asymmetric	21.0	4.9	1560	2.4	This work
PAC/Cl	2652	Symmetric	5.8	3.3	-	6.9	[10]
PAC/PTS	3649	Symmetric	22.2	6.4	1517	4.2	[11]
PAC/PTS§	3444	Asymmetric	20.7	2.9	791	2.7	[68]
PAC/S§	2630	Asymmetric	16.4	3.1	683	3.4	[68]

Notes: PAC/Cl: AC from chloride-doped polyaniline; PAC/PTS: AC from p-toluenesulfonate-doped polyaniline; PAC/S: AC from sulfate-doped polyaniline. § NaCl concentration = 1080 mg L^{-1}.

Table 8. CDI performance using different carbon electrodes

Activated carbon	SSA_{BET} (m^2 g^{-1})	NaCl (mg L^{-1})	Applied voltage (V) or density current (mA cm^2)	SAC (mg g^{-1})	OSR (mg g^{-1} day^{-1})	η (J mg^{-1})	Reference
Filtrasorb 400[a]	700	585	0.4 mA cm^2	3.5	100	4.3	Chen et al. [171]
Nanoporous 3D-graphene	445	500	1.6 V	17.1	163	-	Shi et al. [85]
Sugar cane biowaste-derived	1172	600	1.2 V	22.8	607	-	Lado et al. [55]
Cotton-derived carbon sponge	2680	500	1.2 V	16.1	939	-	Li et al. [172]
Polyglycerol	1684	600	1.6 V	27.1	1070	2.6	Juchen et al. [103]
MSP20[b]	2272	585	2.5 mA cm^2	11.2	1401	1.6	Kang et al. [173]
CEP-21K[c]	2050	1000	1.4 mA cm^2	15.7	2072§	1.2	Choi and Yoon [174]
CTAK	3035	600	1.2 V	21.0	1560	2.4	This work

Notes: AC = activated carbon. Providers of commercial activated carbons: [a] Calgon Carbon, USA; [b] Kansai Coke & Chemicals, Japan; [c] PCT Co., Korea. §Membrane CDI.

CHAPTER 5

CONCLUSIONS AND SUGGESTIONS FOR FUTURE WORKS

In this work, it was demonstrated that tuning the synthesis of PAC/Cl is essential for improving CDI performance. Despite presenting similar *SSA*, a 10-fold reduction of the carbonization heating rate applied in the CTAK* synthesis (1 °C min^{-1}) led to a 2.5-fold increase in *%V$_{mes}$* (from 23.0 to 57.2 %), increasing the electrosorption kinetics 3.5-fold (from 3.3 x 10^{-3} to 11.7 x 10^{-3} s^{-1}), compared to PAC/Cl. However, CTAK* maintained low desalination performance, even in the asymmetric configuration (6.3 mg g^{-1}), which could be attributed to the lower SOGs content (4.2 at.%) that shifted *E$_{pzc}$* to lower values (0.1 vs Ag/AgCl), leading to less negative surface charge. On the other hand, the higher SOG content (5.3 at.%) and the increase of surface polar groups (phenolic and carboxylic groups) in CTAK, improved the electrode hydrophilicity (the contact angle dropped from 87.4 to 40.9º) and shifted *E$_{pzc}$* to more positive values (0.175 V vs Ag/AgCl), compared to CTAK*. These results confirmed the role of PLR in modifying the PAni structure, which altered the activation process with KOH, leading to higher *SAC*. Overall, the surface chemistry seemed to be the most important factor affecting desalination performance. Using the asymmetric configuration, *SAC* increased from 11.4 to 21.0 mg g^{-1}, which was similar to the value obtained using PAC/PTS (22.2 mg g^{-1}). At the same time, *Q$_E$* increased by 24%, mitigating the deleterious effect of co-ion repulsion, improving desalination performance and providing a 29% reduction in specific energy consumption. Although the low *%V$_{mes}$* of YP-80F (31.8%) could have limited the electrosorption/desorption kinetics of CTAK, a high *OSR* value (1560 mg g^{-1} day^{-1}) was achieved, which was even higher than obtained using PAC/PTS (1517 mg g^{-1} day^{-1}). The cost of producing 1 kg of PAC/Cl was estimated to be ~3-fold lower than the cost of producing the same quantity of PAC/PTS. Therefore, the findings of this work revealed the benefits of introducing PLR as a PAni template, in order to obtain a cost-effective activated carbon for application in CDI.

A high-performance chloride-doped polyaniline activated carbon was obtained by simply tuning the synthesis method. New insights about the importance of structure drivers, surface chemistry, and controlled operation conditions on the electrosorption performance have been achieved in this thesis. However, further studies must be carried out to make the electrode technically feasible for large-scale applications. In this regard, the following suggestions are proposed for future works:

- Access the electrode stability and desalination performance in long-term operation;

- Evaluate the desalination performance in more concentrated solutions;

- Evaluate the desalination performance in multicomponent solutions in order to understanding the behavior of the electrode on a real system;

- Explore other applications for CTAK electrodes, such as water softening, heavy metal removal, and nutrient recovery;

- Scale the CTAK electrode and CDI process from the laboratory to pilot plant level, using cell with different stacks, for pre-commercial application and evaluate the performance in terms of *SAC*, kinetics, water recovery (%), water production (L h^{-1} m^{-2}) and energy consumption (kW h m^{-3});

- Study the technical-economic feasibility of CTAK in CDI desalination, linking the lab-scale experimental performance to capital and operating costs of full-scale water production.

- Study the feasibility of using the material in portable and affordable desalinators to be used at home, especially in desert lands and rural areas with lack of freshwater resources.

> *"No matter which technologies are going to be dominant in the future, we can see that desalination is destined to play a vital role in future water production. Desalination is destiny."*
>
> J. Nordstrand [175]

CHAPTER 6

SCIENTIFIC PRODUCTION

6.1 Journals

[1]   **K.S.G.C. Oliveira**, K.M. Barcelos, J.J. Lado, J. Palma, L.A.M. Ruotolo, Improving the electrochemical desalination performance of chloride-doped polyaniline activated carbon electrode by tuning the synthesis method, Chemical Engineering Journal. 457 (2023) 141059. https://doi.org/10.1016/j.cej.2022.141059.

[2]   P.T. Juchen, K.M. Barcelos, **K.S.G.C. Oliveira**, L.A.M. Ruotolo, Using crude residual glycerol as precursor of sustainable activated carbon electrodes for capacitive deionization desalination, Chemical Engineering Journal. 429 (2022) 132209. https://doi.org/10.1016/j.cej.2021.132209.

[3]   K.M. Barcelos, **K.S.G.C. Oliveira**, D.S.A. Silva, E.A. Urquieta-González, L.A.M. Ruotolo, Efficient and stable operation of capacitive deionization assessed by electrode and membrane asymmetry, Electrochim Acta. 388 (2021) 138631. https://doi.org/10.1016/j.electacta.2021.138631.

[4]   K.M. Barcelos, **K.S.G.C. Oliveira**, L.A.M. Ruotolo, Insights on the role of interparticle porosity and electrode thickness on capacitive deionization performance for desalination, Desalination. 492 (2020) 114594. https://doi.org/10.1016/j.desal.2020.114594.

6.2 Conferences

[1]   **K.S.G.C. Oliveira**, K.M. Barcelos, J.J. Lado, J. Palma, L.A.M. Ruotolo, Desempeño superior en desalinización usando carbón activado de polianilina dopada con cloruro y modificada con un modelo F127. In: XLII Reunión del Grupo Especializado de Electroquímica de la RSEQ, Santander, Spain, 2022.

[2]   **K.S.G.C. Oliveira**, Insights into the lithium recovery using GF-LMO electrodes in a flow-through rocking-chair cell. In: XLII Reunión del Grupo Especializado de Electroquímica de la RSEQ, Santander, Spain, 2022.

[3]   **K.S.G.C. Oliveira**, J. Palma, J.J. Lado, L.A.M. Ruotolo, Electrochemical lithium recovery using GF-LMO electrodes: insights and perspectives. In: 9th European Summer School of Electrochemical Engineering, Southampton, England, 2022.

[4]   P.T. Juchen, K.M. Barcelos, **K.S.G.C. Oliveira**, L.A.M. Ruotolo, Asymmetric electrochemical desalination using activated carbon electrodes produced with residual glycerol of biodiesel. In: XXIII Simpósio Brasileiro de Eletroquímica e Eletroanalítica, Mato Grosso do Sul, Brazil, 2021.

[5]   K.M. Barcelos, **K.S.G.C. Oliveira**, L.A.M. Ruotolo, Effect of Interparticle Porosity and Electrode Thickness on the Desalination Performance by Capacitive Deionization. In: 71th Annual Meeting of the International Society of Electrochemistry, Belgrade, Serbia, 2020.

REFERENCES

[1] United Nations, The United Nations World Water Development Report. Groundwater: Making the invisible visible, UNESCO, Paris, 2022.

[2] J.J. Lado, V. Cartolano, E. García-Quismondo, G. García, I. Almonacid, V. Senatore, V. Naddeo, J. Palma, M.A. Anderson, Performance analysis of a capacitive deionization stack for brackish water desalination, Desalination. 501 (2021) 114912. https://doi.org/10.1016/j.desal.2020.114912.

[3] M.E. Suss, S. Porada, X. Sun, P.M. Biesheuvel, J. Yoon, V. Presser, Water desalination via capacitive deionization: what is it and what can we expect from it?, Energy Environ Sci. 8 (2015) 2296–2319. https://doi.org/10.1039/C5EE00519A.

[4] M.A. Anderson, A.L. Cudero, J. Palma, Capacitive deionization as an electrochemical means of saving energy and delivering clean water. Comparison to present desalination practices: Will it compete?, Electrochim Acta. 55 (2010) 3845–3856. https://doi.org/10.1016/j.electacta.2010.02.012.

[5] J.J. Lado, E. García-Quismondo, I. Almonacid, G. García, G. Castro, J. Palma, A successful transition from a vanadium redox flow battery stack to an energy efficient electrochemical desalination module, J Environ Chem Eng. 9 (2021) 106875. https://doi.org/10.1016/j.jece.2021.106875.

[6] P.T. Juchen, L.A.M. Ruotolo, Roles of mass transfer and cell architecture in electrochemical desalination performance using polyglycerol activated carbon electrodes, Chemical Engineering Journal. 452 (2023) 139226. https://doi.org/10.1016/j.cej.2022.139226.

[7] R.L. Zornitta, L.A.M. Ruotolo, L.C.P.M. de Smet, High-Performance Carbon Electrodes Modified with Polyaniline for Stable and Selective Anion Separation, Sep Purif Technol. 290 (2022) 120807. https://doi.org/10.1016/j.seppur.2022.120807.

[8] S.F. Evans, M.R. Ivancevic, D.J. Wilson, Z.D. Hood, S.P. Adhikari, A.K. Naskar, C. Tsouris, M.P. Paranthaman, Carbon polyaniline capacitive deionization electrodes with stable cycle life, Desalination. 464 (2019) 25–32. https://doi.org/10.1016/j.desal.2019.04.002.

[9] C. Yan, L. Zou, R. Short, Polyaniline-modified activated carbon electrodes for capacitive deionisation, Desalination. 333 (2014) 101–106. https://doi.org/10.1016/j.desal.2013.11.032.

[10] R.L. Zornitta, F.J. García-Mateos, J.J. Lado, J. Rodríguez-Mirasol, T. Cordero, P. Hammer, L.A.M. Ruotolo, High-performance activated carbon from polyaniline for capacitive deionization, Carbon N Y. 123 (2017) 318–333. https://doi.org/10.1016/j.carbon.2017.07.071.

[11] R.L. Zornitta, K.M. Barcelos, F.G.E.E. Nogueira, L.A.M.L.A.M. Ruotolo, Understanding the mechanism of carbonization and KOH activation of polyaniline leading to enhanced electrosorption performance, Carbon N Y. 156 (2020) 346–358. https://doi.org/10.1016/j.carbon.2019.09.058.

[12] J.J. Lado, R.L. Zornitta, F.A. Calvi, M. Martins, M.A. Anderson, F.G.E. Nogueira, L.A.M. Ruotolo, Enhanced capacitive deionization desalination provided by chemical activation of sugar cane bagasse fly ash electrodes, J Anal Appl Pyrolysis. 126 (2017) 143–153. https://doi.org/10.1016/j.jaap.2017.06.014.

[13] Q. Liu, X. Li, Y. Wu, M. Qing, G. Tan, D. Xiao, Pine pollen derived porous carbon with efficient capacitive deionization performance, Electrochim Acta. 298 (2019) 360–371.

[14] C.-T. Hsieh, H. Teng, Influence of oxygen treatment on electric double-layer capacitance of activated carbon fabrics, Carbon N Y. 40 (2002) 667–674. https://doi.org/10.1016/S0008-6223(01)00182-8.

[15] E. Bayram, E. Ayranci, A systematic study on the changes in properties of an activated carbon cloth upon polarization, Electrochim Acta. 56 (2011) 2184–2189. https://doi.org/10.1016/j.electacta.2010.12.018.

[16] K.M. Barcelos, K.S.G.C. Oliveira, L.A.M. Ruotolo, Insights on the role of interparticle porosity and electrode thickness on capacitive deionization performance for desalination, Desalination. 492 (2020) 114594. https://doi.org/10.1016/j.desal.2020.114594.

[17] R.L. Zornitta, L.A.M. Ruotolo, Simultaneous analysis of electrosorption capacity and kinetics for CDI desalination using different electrode configurations, Chemical Engineering Journal. 332 (2018) 33–41. https://doi.org/10.1016/j.cej.2017.09.067.

[18] F. Zhang, Y. Meng, D. Gu, Yan, C. Yu, B. Tu, D. Zhao, A Facile Aqueous Route to Synthesize Highly Ordered Mesoporous Polymers and Carbon Frameworks with *Ia 3̄ d* Bicontinuous Cubic Structure, J Am Chem Soc. 127 (2005) 13508–13509. https://doi.org/10.1021/ja0545721.

[19] J.T. Cai, A.N. Zhou, X.Y. Li, J.Y. Yan, L.J. Wang, J.X. Jiang, Preparation of Hierarchical and Ordered Porous Nanostructured Carbons, Adv Mat Res. 912–914 (2014) 273–276. https://doi.org/10.4028/www.scientific.net/AMR.912-914.273.

[20] G. Xin, Y. Wang, S. Jia, P. Tian, S. Zhou, J. Zang, Synthesis of nitrogen-doped mesoporous carbon from polyaniline with an F127 template for high-performance supercapacitors, Appl Surf Sci. 422 (2017) 654–660. https://doi.org/10.1016/j.apsusc.2017.06.084.

[21] J. Castro-Gutiérrez, A. Sanchez-Sanchez, J. Ghanbaja, N. Díez, M. Sevilla, A. Celzard, V. Fierro, Synthesis of perfectly ordered mesoporous carbons by water-assisted mechanochemical self-assembly of tannin, Green Chemistry. 20 (2018) 5123–5132.

[22] H. Qin, R. Jian, J. Bai, J. Tang, Y. Zhou, B. Zhu, D. Zhao, Z. Ni, L. Wang, W. Liu, Q. Zhou, X. Li, Influence of Molecular Weight on Structure and Catalytic Characteristics of Ordered Mesoporous Carbon Derived from Lignin, ACS Omega. 3 (2018) 1350–1356. https://doi.org/10.1021/acsomega.7b01870.

[23] K.C. Leonard, J.R. Genthe, J.L. Sanfilippo, W.A. Zeltner, M.A. Anderson, Synthesis and characterization of asymmetric electrochemical capacitive deionization materials using nanoporous silicon dioxide and magnesium doped aluminum oxide, Electrochim Acta. 54 (2009) 5286–5291. https://doi.org/10.1016/j.electacta.2009.01.082.

[24] United Nations, Transforming our world: the 2030 Agenda for Sustainable Development, (2015) 35. https://sdgs.un.org/goals (accessed January 9, 2023).

[25] N. Herold, 5 Facts About Water Scarcity, MECO Company. (2022). https://www.meco.com/facts-about-water-scarcity/ (accessed January 9, 2023).

[26] National Geographic, Earth's Freshwater: A Guide for Teaching Freshwater in Grades 3 to 8, Washington, DC, 2022.

[27] UNESCO, The United Nations world water development report 2018: nature-based solutions for water, United Nations Educational, Scientific and Cultural Organization, Paris, France, 2018.

[28] T.M. Soares, I.J.O. da Silva, S.N. Duarte, Ê.F. de F. e Silva, Destinação de águas residuárias provenientes do processo de dessalinização por osmose reversa, Revista Brasileira de Engenharia Agrícola e Ambiental. 10 (2006) 730–737. https://doi.org/10.1590/S1415-43662006000300028.

[29] S. Porada, Preparation of Carbon Electrodes for Water Desalination Using Capacitive Deionization, Wrocław University of Technology, 2013.

[30] Aquatech, Does Size Matter? Meet Ten of The World's Largest Desalination Plants, (2021). https://www.aquatechtrade.com/news/desalination/worlds-largest-desalination-plants/ (accessed January 9, 2023).

[31] F. Virgili, T. Pankratz, IDA Desalination Yearbook 2016-2017, International Desalination Association, 2016.

[32] A.P. Bhat, Capacitive deionization performance of bi-tortuous activated carbon electrodes coated with asymmetrically charged polyelectrolytes, University of Illinois Urbana-Champaign, 2019.

[33] T. Mezher, H. Fath, Z. Abbas, A. Khaled, Techno-economic assessment and environmental impacts of desalination technologies, Desalination. 266 (2011) 263–273. https://doi.org/10.1016/j.desal.2010.08.035.

[34] J. Miller, Review of water resources and desalination technologies, Albuquerque, NM, and Livermore, CA (United States), 2003. https://doi.org/10.2172/809106.

[35] N. Ghaffour, T.M. Missimer, G.L. Amy, Technical review and evaluation of the economics of water desalination: Current and future challenges for better water supply sustainability, Desalination. 309 (2013) 197–207. https://doi.org/10.1016/j.desal.2012.10.015.

[36] Flowserve, Desalination: Multistage flash distillation (MSF) and multi-effect distillation (MED), Flowserve Company. (2022). https://www.flowserve.com/en/industries/water/desalination/ (accessed January 13, 2023).

[37] A.C. Orbezo, Optimization of Capacitive Deionization Systems: An Electrochemical Approach, University of Manchester, 2020.

[38] M.S. Islam, A. Sultana, A.H.M. Saadat, M.S. Islam, M. Shammi, M.K. Uddin, Desalination Technologies for Developing Countries: A Review, Journal of Scientific Research. 10 (2018) 77–97. https://doi.org/10.3329/jsr.v10i1.33179.

[39] CONFAP, Conselho Nacional das Fundações Estaduais de Amparo à Pesquisa, (2016). https://confap.org.br/news/pesquisador-da-ufcg-defende-a-dessalinizacao-da-agua-como-reaproveitamento/ (accessed January 13, 2023).

[40] Aqua Safe Mine, Brackish Water Reverse Osmosis (BWRO), ASM The Treater Wastewater Treatment Organization. (2021). https://www.aquasafemine.com/brackish-water-reverse-osmosis/ (accessed January 13, 2023).

[41] BUR-USA, Yuma Desalting Plant Operations: Reverse Osmosis, Department of the Interior-Bureau of Reclamation, USA. (2015). https://www.usbr.gov/lc/yuma/facilities/ydp/yao_ydp_operations_ro.html (accessed January 13, 2023).

[42] S. Al-Amshawee, M.Y.B.M. Yunus, A.A.M. Azoddein, D.G. Hassell, I.H. Dakhil, H.A. Hasan, Electrodialysis desalination for water and wastewater: A review, Chemical Engineering Journal. 380 (2020) 122231. https://doi.org/10.1016/j.cej.2019.122231.

[43] H. Zhu, B. Yang, C. Gao, Y. Wu, Ion transfer modeling based on Nernst–Planck theory for saline water desalination during electrodialysis process, Asia-Pacific Journal of Chemical Engineering. 15 (2020). https://doi.org/10.1002/apj.2410.

[44] P. Nie, B. Hu, X. Shang, Z. Xie, M. Huang, J. Liu, Highly efficient water softening by mordenite modified cathode in asymmetric capacitive deionization, Sep Purif Technol. 250 (2020) 117240. https://doi.org/10.1016/j.seppur.2020.117240.

[45] L. Wang, S. Lin, Mechanism of Selective Ion Removal in Membrane Capacitive Deionization for Water Softening, Environ Sci Technol. 53 (2019) 5797–5804. https://doi.org/10.1021/acs.est.9b00655.

[46] Z. Du, W. Tian, K. Qiao, J. Zhao, L. Wang, W. Xie, M. Chu, T. Song, Improved chlorine and chromium ion removal from leather processing wastewater by biocharcoal-based

capacitive deionization, Sep Purif Technol. 233 (2020) 116024. https://doi.org/10.1016/j.seppur.2019.116024.

[47] X. Su, A. Kushima, C. Halliday, J. Zhou, J. Li, T.A. Hatton, Electrochemically-mediated selective capture of heavy metal chromium and arsenic oxyanions from water, Nat Commun. 9 (2018) 4701. https://doi.org/10.1038/s41467-018-07159-0.

[48] Y. Bian, X. Chen, L. Lu, P. Liang, Z.J. Ren, Concurrent Nitrogen and Phosphorus Recovery Using Flow-Electrode Capacitive Deionization, ACS Sustain Chem Eng. 7 (2019) 7844–7850. https://doi.org/10.1021/acssuschemeng.9b00065.

[49] F. Gao, L. Wang, J. Wang, H. Zhang, S. Lin, Nutrient recovery from treated wastewater by a hybrid electrochemical sequence integrating bipolar membrane electrodialysis and membrane capacitive deionization, Environ Sci (Camb). 6 (2020) 383–391. https://doi.org/10.1039/C9EW00981G.

[50] J. Choi, P. Dorji, H.K. Shon, S. Hong, Applications of capacitive deionization: Desalination, softening, selective removal, and energy efficiency, Desalination. 449 (2019) 118–130. https://doi.org/10.1016/j.desal.2018.10.013.

[51] H.O. Stern, Theorie der Elektrolytischen Doppelschicht, Elektrochem Angew Phys Chem. 30 (1924) 508–516.

[52] S. Porada, R. Zhao, A. van der Wal, V. Presser, P.M. Biesheuvel, Review on the science and technology of water desalination by capacitive deionization, Prog Mater Sci. 58 (2013) 1388–1442. https://doi.org/10.1016/j.pmatsci.2013.03.005.

[53] R.L. Zornitta, J.J. Lado, M.A. Anderson, L.A.M. Ruotolo, Effect of electrode properties and operational parameters on capacitive deionization using low-cost commercial carbons, Sep Purif Technol. 158 (2016) 39–52. https://doi.org/10.1016/j.seppur.2015.11.043.

[54] X. Gao, S. Porada, A. Omosebi, K.-L. Liu, P.M. Biesheuvel, J. Landon, Complementary surface charge for enhanced capacitive deionization, Water Res. 92 (2016) 275–282. https://doi.org/10.1016/j.watres.2016.01.048.

[55] J.J. Lado, R.L. Zornitta, I. Vázquez Rodríguez, K. Malverdi Barcelos, L.A.M. Ruotolo, Sugarcane Biowaste-Derived Biochars as Capacitive Deionization Electrodes for Brackish Water Desalination and Water-Softening Applications, ACS Sustain Chem Eng. 7 (2019) 18992–19004. https://doi.org/10.1021/acssuschemeng.9b04504.

[56] S. Porada, L. Zhang, J.E. Dykstra, Energy consumption in membrane capacitive deionization and comparison with reverse osmosis, Desalination. 488 (2020) 114383. https://doi.org/10.1016/j.desal.2020.114383.

[57] M. Qin, A. Deshmukh, R. Epsztein, S.K. Patel, O.M. Owoseni, W.S. Walker, M. Elimelech, Comparison of energy consumption in desalination by capacitive deionization and reverse osmosis, Desalination. 455 (2019) 100–114. https://doi.org/10.1016/j.desal.2019.01.003.

[58] W. Zhang, M. Mossad, L. Zou, A study of the long-term operation of capacitive deionisation in inland brackish water desalination, Desalination. 320 (2013) 80–85. https://doi.org/10.1016/j.desal.2013.04.010.

[59] E. García-Quismondo, C. Santos, J. Lado, J. Palma, M.A. Anderson, Optimizing the energy efficiency of capacitive deionization reactors working under real-world conditions, Environ Sci Technol. 47 (2013) 11866–11872. https://doi.org/10.1021/es4021603.

[60] C. Tan, C. He, J. Fletcher, T.D. Waite, Energy recovery in pilot scale membrane CDI treatment of brackish waters, Water Res. 168 (2020) 115146. https://doi.org/10.1016/j.watres.2019.115146.

[61] J.W. Blair, G.W. Murphy, Electrochemical Demineralization of Water with Porous Electrodes of Large Surface Area, in: 1960: pp. 206–223. https://doi.org/10.1021/ba-1960-0027.ch020.

[62] Y. Wang, I. Vázquez-Rodríguez, C. Santos, E. García-Quismondo, J. Palma, M.A. Anderson, J.J. Lado, Graphite felt 3D framework composites as an easy to scale capacitive deionization electrode for brackish water desalination, Chemical Engineering Journal. 392 (2020) 123698. https://doi.org/10.1016/j.cej.2019.123698.

[63] C. Tan, C. He, W. Tang, P. Kovalsky, J. Fletcher, T.D. Waite, Integration of photovoltaic energy supply with membrane capacitive deionization (MCDI) for salt removal from brackish waters, Water Res. 147 (2018) 276–286. https://doi.org/10.1016/j.watres.2018.09.056.

[64] P. Srimuk, M. Zeiger, N. Jäckel, A. Tolosa, B. Krüner, S. Fleischmann, I. Grobelsek, M. Aslan, B. Shvartsev, M.E. Suss, V. Presser, Enhanced performance stability of carbon/titania hybrid electrodes during capacitive deionization of oxygen saturated saline water, Electrochim Acta. 224 (2017) 314–328. https://doi.org/10.1016/j.electacta.2016.12.060.

[65] S. Porada, L. Weinstein, R. Dash, A. van der Wal, M. Bryjak, Y. Gogotsi, P.M. Biesheuvel, Water Desalination Using Capacitive Deionization with Microporous Carbon Electrodes, ACS Appl Mater Interfaces. 4 (2012) 1194–1199. https://doi.org/10.1021/am201683j.

[66] X. Gao, A. Omosebi, J. Landon, K. Liu, Surface charge enhanced carbon electrodes for stable and efficient capacitive deionization using inverted adsorption-desorption behavior, Energy Environ Sci. 8 (2015) 897–909. https://doi.org/10.1039/C4EE03172E.

[67] J.-H. Choi, Determination of the electrode potential causing Faradaic reactions in membrane capacitive deionization, Desalination. 347 (2014) 224–229. https://doi.org/10.1016/j.desal.2014.06.004.

[68] K.M. Barcelos, K.S.G.C. Oliveira, D.S.A. Silva, E.A. Urquieta-González, L.A.M. Ruotolo, Efficient and stable operation of capacitive deionization assessed by electrode and membrane asymmetry, Electrochim Acta. 388 (2021) 138631. https://doi.org/10.1016/j.electacta.2021.138631.

[69] S. Hand, J.S. Guest, R.D. Cusick, Technoeconomic Analysis of Brackish Water Capacitive Deionization: Navigating Tradeoffs between Performance, Lifetime, and Material Costs, Environ Sci Technol. 53 (2019) 13353–13363. https://doi.org/10.1021/acs.est.9b04347.

[70] Y. Oren, Capacitive deionization (CDI) for desalination and water treatment — past, present and future (a review), Desalination. 228 (2008) 10–29. https://doi.org/10.1016/j.desal.2007.08.005.

[71] R.L. Zornitta, P. Srimuk, J. Lee, B. Krüner, M. Aslan, L.A.M. Ruotolo, V. Presser, Charge and Potential Balancing for Optimized Capacitive Deionization Using Lignin-Derived, Low-Cost Activated Carbon Electrodes, ChemSusChem. 11 (2018) 2101–2113. https://doi.org/10.1002/cssc.201800689.

[72] C.J. Gabelich, T.D. Tran, I.H. "Mel" Suffet, Electrosorption of Inorganic Salts from Aqueous Solution Using Carbon Aerogels, Environ Sci Technol. 36 (2002) 3010–3019. https://doi.org/10.1021/es0112745.

[73] S. Bi, Y. Zhang, L. Cervini, T. Mo, J.M. Griffin, V. Presser, G. Feng, Permselective ion electrosorption of subnanometer pores at high molar strength enables capacitive deionization of saline water, Sustain Energy Fuels. 4 (2020) 1285–1295. https://doi.org/10.1039/C9SE00996E.

[74] C. Tsouris, R. Mayes, J. Kiggans, K. Sharma, S. Yiacoumi, D. DePaoli, S. Dai, Mesoporous Carbon for Capacitive Deionization of Saline Water, Environ Sci Technol. 45 (2011) 10243–10249. https://doi.org/10.1021/es201551e.

[75] C.-L. Yeh, H.-C. Hsi, K.-C. Li, C.-H. Hou, Improved performance in capacitive deionization of activated carbon electrodes with a tunable mesopore and micropore ratio, Desalination. 367 (2015) 60–68. https://doi.org/10.1016/j.desal.2015.03.035.

[76] S. Porada, L. Borchardt, M. Oschatz, M. Bryjak, J.S. Atchison, K.J. Keesman, S. Kaskel, P.M. Biesheuvel, V. Presser, Direct prediction of the desalination performance of porous carbon electrodes for capacitive deionization, Energy Environ Sci. 6 (2013) 3700. https://doi.org/10.1039/c3ee42209g.

[77] G. Shen, J. Ma, J. Niu, R. Zhang, J. Zhang, X. Wang, J. Liu, J. Gu, R. Chen, X. Li, C. Liu, Mechanism of ball milled activated carbon in improving the desalination performance of flow- and fixed-electrode in capacitive deionization desalination, Front Environ Sci Eng. 17 (2023) 64. https://doi.org/10.1007/s11783-023-1664-6.

[78] S. Tian, Z. Zhang, X. Zhang, K. (Ken) Ostrikov, Capacitative deionization using commercial activated carbon fiber decorated with polyaniline, J Colloid Interface Sci. 537 (2019) 247–255. https://doi.org/10.1016/j.jcis.2018.11.025.

[79] J.M.A. Freire, J.J. Lado, E. García-Quismondo, G.C. Burillo, J. Palma, A.R. Loiola, E. Longhinotti, M.A. Anderson, Strategies to boost capacitive deionization performance of 3D electrodes, Sep Purif Technol. 273 (2021) 118977. https://doi.org/10.1016/j.seppur.2021.118977.

[80] J.-J. Huang, Y.-X. Zhang, K.-C. Cheng, Y.-W. Wang, D.-S. Wuu, Preparation of stacked CoxNiyOz/TiO2 thin film structure on carbon cloth for flow-through capacitive deionization device, J Mater Res. 37 (2022) 4222–4231. https://doi.org/10.1557/s43578-022-00788-8.

[81] L. Wang, M. Wang, Z.-H. Huang, T. Cui, X. Gui, F. Kang, K. Wang, D. Wu, Capacitive deionization of NaCl solutions using carbon nanotube sponge electrodes, J Mater Chem. 21 (2011) 18295. https://doi.org/10.1039/c1jm13105b.

[82] S. Zhang, Y. Wang, X. Han, Y. Cai, S. Xu, Optimizing the fabrication of carbon nanotube electrode for effective capacitive deionization via electrophoretic deposition strategy, Progress in Natural Science: Materials International. 28 (2018) 251–257. https://doi.org/10.1016/j.pnsc.2018.02.010.

[83] F. Saffarimiandoab, R. Sabetvand, X. Zhang, Molecular insights into capacitive deionization mechanisms inside hydrophobic and hydrophilic carbon nanotube channel electrodes, J Mater Chem A Mater. 10 (2022) 23332–23340. https://doi.org/10.1039/D2TA06006J.

[84] H. Wang, T. Yan, P. Liu, G. Chen, L. Shi, J. Zhang, Q. Zhong, D. Zhang, In situ creating interconnected pores across 3D graphene architectures and their application as high performance electrodes for flow-through deionization capacitors, J Mater Chem A Mater. 4 (2016) 4908–4919. https://doi.org/10.1039/C5TA10703B.

[85] W. Shi, H. Li, X. Cao, Z.Y. Leong, J. Zhang, T. Chen, H. Zhang, H.Y. Yang, Ultrahigh Performance of Novel Capacitive Deionization Electrodes based on A Three-Dimensional Graphene Architecture with Nanopores, Sci Rep. 6 (2016) 18966. https://doi.org/10.1038/srep18966.

[86] C. Chen, L. Men, A. Liu, S. Yu, J. Zhou, Z. Wei, D. Ju, Enhanced electrochemical and capacitive deionization performances of single-layer graphene oxide/nitrogen-doped porous carbon/activated carbon fiber composite electrodes, J Environ Chem Eng. 10 (2022) 108696. https://doi.org/10.1016/j.jece.2022.108696.

[87] H. Xu, M. Li, S. Gong, F. Zhao, Y. Zhao, C. Li, J. Qi, Z. Wang, H. Wang, X. Fan, W. Peng, J. Liu, Constructing titanium carbide MXene/reduced graphene oxide superlattice

heterostructure via electrostatic self-assembly for high-performance capacitive deionization, J Colloid Interface Sci. 624 (2022) 233–241. https://doi.org/10.1016/j.jcis.2022.05.131.

[88]   P. Srimuk, J. Halim, J. Lee, Q. Tao, J. Rosen, V. Presser, Two-Dimensional Molybdenum Carbide (MXene) with Divacancy Ordering for Brackish and Seawater Desalination via Cation and Anion Intercalation, ACS Sustain Chem Eng. 6 (2018) 3739–3747. https://doi.org/10.1021/acssuschemeng.7b04095.

[89]   X. Liu, H. Liu, M. Mi, W. Kong, Y. Ge, J. Hu, Nitrogen-doped hierarchical porous carbon aerogel for high-performance capacitive deionization, Sep Purif Technol. 224 (2019) 44–50. https://doi.org/10.1016/j.seppur.2019.05.010.

[90]   T.H. Nguyen, V.V. Nguyen, N.T. Nguyen, T. Nguyen, T.V.T. Nguyen, H.L. Ngo, L.T.N. Huynh, T.N. Tran, T.T.N. Ho, T.T. Nguyen, V.H. Le, Preparation, characterization and CDI application of KOH-activated porous waste-corn-stalk-based carbon aerogel, Journal of Porous Materials. (2022). https://doi.org/10.1007/s10934-022-01411-1.

[91]   A.P. Silva, A. Argondizo, P.T. Juchen, L.A.M. Ruotolo, Ultrafast capacitive deionization using rice husk activated carbon electrodes, Sep Purif Technol. 271 (2021) 118872. https://doi.org/10.1016/j.seppur.2021.118872.

[92]   Z. Xie, X. Shang, J. Yan, T. Hussain, P. Nie, J. Liu, Biomass-derived porous carbon anode for high-performance capacitive deionization, Electrochim Acta. 290 (2018) 666–675. https://doi.org/10.1016/j.electacta.2018.09.104.

[93]   P. Ratajczak, M.E. Suss, F. Kaasik, F. Béguin, Carbon electrodes for capacitive technologies, Energy Storage Mater. 16 (2019) 126–145. https://doi.org/10.1016/j.ensm.2018.04.031.

[94]   S. Porada, F. Schipper, M. Aslan, M. Antonietti, V. Presser, T. Fellinger, Capacitive Deionization using Biomass-based Microporous Salt-Templated Heteroatom-Doped Carbons, ChemSusChem. 8 (2015) 1867–1874. https://doi.org/10.1002/cssc.201500166.

[95]   F.A. AlMarzooqi, A.A. al Ghaferi, I. Saadat, N. Hilal, Application of Capacitive Deionisation in water desalination: A review, Desalination. 342 (2014) 3–15. https://doi.org/10.1016/j.desal.2014.02.031.

[96]   E. Frackowiak, F. Béguin, Carbon materials for the electrochemical storage of energy in capacitors, Carbon N Y. 39 (2001) 937–950. https://doi.org/10.1016/S0008-6223(00)00183-4.

[97]   R.L. Zornitta, P. Srimuk, J. Lee, B. Krüner, M. Aslan, L.A.M. Ruotolo, V. Presser, Charge and Potential Balancing for Optimized Capacitive Deionization Using Lignin-Derived, Low-Cost Activated Carbon Electrodes, ChemSusChem. 11 (2018) 2101–2113.

[98]   T. Wu, G. Wang, F. Zhan, Q. Dong, Q. Ren, J. Wang, J. Qiu, Surface-treated carbon electrodes with modified potential of zero charge for capacitive deionization, Water Res. 93 (2016) 30–37. https://doi.org/10.1016/j.watres.2016.02.004.

[99]   C. Dou, S. Zhai, Y. Liu, P. Chen, D. Yin, G. Huang, L. Zhang, Chemical modification of carbon particles to enhance the electrosorption of capacitive deionization process, Journal of Water Reuse and Desalination. 10 (2020) 57–69. https://doi.org/10.2166/wrd.2020.052.

[100]   B. Viswanathan, P. Indra Nee, T.K. Varadarajan, Methods of Activation and Specific Applications of Carbon Materials, NCCR, Indian Institute of Technology Madras , Chennai, India, 2009.

[101]   M. Vujković, N. Gavrilov, I. Pašti, J. Krstić, J. Travas-Sejdic, G. Ćirić-Marjanović, S. Mentus, Superior capacitive and electrocatalytic properties of carbonized nanostructured polyaniline upon a low-temperature hydrothermal treatment, Carbon N Y. 64 (2013) 472–486. https://doi.org/10.1016/j.carbon.2013.07.100.

[102] J.J. Lado, R.L. Zornitta, F.A. Calvi, M.I. Tejedor-Tejedor, M.A. Anderson, L.A.M. Ruotolo, Study of sugar cane bagasse fly ash as electrode material for capacitive deionization, J Anal Appl Pyrolysis. 120 (2016) 389–398. https://doi.org/10.1016/j.jaap.2016.06.009.

[103] P.T. Juchen, K.M. Barcelos, K.S.G.C. Oliveira, L.A.M. Ruotolo, Using crude residual glycerol as precursor of sustainable activated carbon electrodes for capacitive deionization desalination, Chemical Engineering Journal. 429 (2022) 132209. https://doi.org/10.1016/j.cej.2021.132209.

[104] Y. Wang, L. Zhang, Y. Wu, S. Xu, J. Wang, Polypyrrole/carbon nanotube composites as cathode material for performance enhancing of capacitive deionization technology, Desalination. 354 (2014) 62–67. https://doi.org/10.1016/j.desal.2014.09.021.

[105] S. Özkul, Investigation of desalination performance of capacitive deionization technology, Middle East Technical University, 2019.

[106] E. Frackowiak, V. Khomenko, K. Jurewicz, K. Lota, F. Béguin, Supercapacitors based on conducting polymers/nanotubes composites, J Power Sources. 153 (2006) 413–418. https://doi.org/10.1016/j.jpowsour.2005.05.030.

[107] R.L. Zornitta, G. Pincelli, L.A.M. Ruotolo, Modification of the conducting polymer polyaniline for enabling cation exchange, Quim Nova. (2014). https://doi.org/10.5935/0100-4042.20140227.

[108] E. Song, J.-W. Choi, Conducting Polyaniline Nanowire and Its Applications in Chemiresistive Sensing, Nanomaterials. 3 (2013) 498–523. https://doi.org/10.3390/nano3030498.

[109] Y. Liu, X. Zhang, X. Gu, N. Wu, R. Zhang, Y. Shen, B. Zheng, J. Wu, W. Zhang, S. Li, F. Huo, One-step turning leather wastes into heteroatom doped carbon aerogel for performance enhanced capacitive deionization, Microporous and Mesoporous Materials. 303 (2020) 110303. https://doi.org/10.1016/j.micromeso.2020.110303.

[110] Y. Liu, C. Nie, X. Liu, X. Xu, Z. Sun, L. Pan, Review on carbon-based composite materials for capacitive deionization, RSC Adv. 5 (2015) 15205–15225. https://doi.org/10.1039/c4ra14447c.

[111] H. Younes, M.M. Rahman, H. Hong, M. AlNahyan, F. Ravaux, Capacitive deionization performance of asymmetric nanoengineered CoFe2O4 carbon nanomaterials composite, Environmental Science and Pollution Research. (2022). https://doi.org/10.1007/s11356-022-24516-1.

[112] M. Oschatz, M. Zeiger, N. Jäckel, P. Strubel, L. Borchardt, R. Reinhold, W. Nickel, J. Eckert, V. Presser, S. Kaskel, Emulsion soft templating of carbide-derived carbon nanospheres with controllable porosity for capacitive electrochemical energy storage, J Mater Chem A Mater. 3 (2015) 17983–17990. https://doi.org/10.1039/C5TA03730A.

[113] Z.-Y. Yang, L.-J. Jin, G.-Q. Lu, Q.-Q. Xiao, Y.-X. Zhang, L. Jing, X.-X. Zhang, Y.-M. Yan, K.-N. Sun, Sponge-Templated Preparation of High Surface Area Graphene with Ultrahigh Capacitive Deionization Performance, Adv Funct Mater. 24 (2014) 3917–3925. https://doi.org/10.1002/adfm.201304091.

[114] X. Yang, W. Chen, H. Bian, T. Sun, Y. Du, Z. Zhang, W. Zhang, Y. Li, X. Chen, F. Wang, Synthesis of Mesoporous ZIF-8 Nanoribbons and their Conversion into Carbon Nanoribbons for High-Performance Supercapacitors, Chemistry - A European Journal. 24 (2018) 11185–11192. https://doi.org/10.1002/chem.201801869.

[115] Y. Zhao, Y. Cai, Y. Wang, S. Xu, A win-win strategy of β-cyclodextrin and ion-doped polypyrrole composite nanomaterials for asymmetric capacitive deionization, Sep Purif Technol. 259 (2021) 118175. https://doi.org/10.1016/j.seppur.2020.118175.

[116] Y. Duan, F. Pan, Q. Liu, Y. Zhou, A. Liang, J. Zhang, Salt-Induced Phase Separation to Synthesize Ordered Mesoporous Carbon by pH-Controlled Self-Assembly, The Journal

of Physical Chemistry C. 121 (2017) 1243–1248. https://doi.org/10.1021/acs.jpcc.6b11056.

[117] T. Wang, P. Zhang, Y. Sun, B. Liu, Y. Liu, Z.-A. Qiao, Q. Huo, S. Dai, New Polymer Colloidal and Carbon Nanospheres: Stabilizing Ultrasmall Metal Nanoparticles for Solvent-Free Catalysis, Chemistry of Materials. 29 (2017) 4044–4051. https://doi.org/10.1021/acs.chemmater.7b00710.

[118] W. Zhou, Z. Lin, G. Tong, S.D. Stoyanov, D. Yan, Y. Mai, X. Zhu, Multi-template synthesis of hierarchically porous carbon spheres with potential application in supercapacitors, RSC Adv. 6 (2016) 111406–111414. https://doi.org/10.1039/C6RA24524B.

[119] X. Yu, J. Lu, C. Zhan, R. Lv, Q. Liang, Z.-H. Huang, W. Shen, F. Kang, Synthesis of activated carbon nanospheres with hierarchical porous structure for high volumetric performance supercapacitors, Electrochim Acta. 182 (2015) 908–916. https://doi.org/10.1016/j.electacta.2015.10.016.

[120] S. Xiong, J. Fan, Y. Wang, J. Zhu, J. Yu, Z. Hu, A facile template approach to nitrogen-doped hierarchical porous carbon nanospheres from polydopamine for high-performance supercapacitors, J Mater Chem A Mater. 5 (2017) 18242–18252. https://doi.org/10.1039/C7TA05880B.

[121] L. Zou, L. Li, H. Song, G. Morris, Using mesoporous carbon electrodes for brackish water desalination, Water Res. 42 (2008) 2340–2348. https://doi.org/10.1016/j.watres.2007.12.022.

[122] Y. Deng, C. Liu, T. Yu, F. Liu, F. Zhang, Y. Wan, L. Zhang, C. Wang, B. Tu, P.A. Webley, H. Wang, D. Zhao, Facile Synthesis of Hierarchically Porous Carbons from Dual Colloidal Crystal/Block Copolymer Template Approach, Chemistry of Materials. 19 (2007) 3271–3277. https://doi.org/10.1021/cm070600y.

[123] V.P. Nemani, S.J. Harris, K.C. Smith, Design of Bi-Tortuous, Anisotropic Graphite Anodes for Fast Ion-Transport in Li-Ion Batteries, J Electrochem Soc. 162 (2015) A1415–A1423. https://doi.org/10.1149/2.0151508jes.

[124] C.L. Cobb, M. Blanco, Modeling mass and density distribution effects on the performance of co-extruded electrodes for high energy density lithium-ion batteries, J Power Sources. 249 (2014) 357–366. https://doi.org/10.1016/j.jpowsour.2013.10.084.

[125] T.S. Hui, M.A.A. Zaini, Potassium hydroxide activation of activated carbon: a commentary, Carbon Letters. 16 (2015) 275–280. https://doi.org/10.5714/CL.2015.16.4.275.

[126] E.J. Jelmy, S. Ramakrishnan, S. Devanathan, M. Rangarajan, N.K. Kothurkar, Optimization of the conductivity and yield of chemically synthesized polyaniline using a design of experiments, J Appl Polym Sci. 130 (2013) 1047–1057. https://doi.org/10.1002/app.39268.

[127] H. Higashimura, S. Kobayashi, Oxidative Polymerization, in: Encyclopedia of Polymer Science and Technology, Wiley, 2016: pp. 1–37. https://doi.org/10.1002/0471440264.pst226.pub2.

[128] W.-S. Huang, B.D. Humphrey, A.G. MacDiarmid, Polyaniline, a novel conducting polymer. Morphology and chemistry of its oxidation and reduction in aqueous electrolytes, Journal of the Chemical Society, Faraday Transactions 1: Physical Chemistry in Condensed Phases. 82 (1986) 2385. https://doi.org/10.1039/f19868202385.

[129] X. Xu, H. Tan, Z. Wang, C. Wang, L. Pan, Y.V. Kaneti, T. Yang, Y. Yamauchi, Extraordinary capacitive deionization performance of highly-ordered mesoporous carbon nano-polyhedra for brackish water desalination, Environ Sci Nano. 6 (2019) 981–989. https://doi.org/10.1039/C9EN00017H.

[130] M.A. Pimenta, G. Dresselhaus, M.S. Dresselhaus, L.G. Cançado, A. Jorio, R. Saito, Studying disorder in graphite-based systems by Raman spectroscopy, Phys. Chem. Chem. Phys. 9 (2007) 1276–1290. https://doi.org/10.1039/B613962K.

[131] K.S. Munir, M. Qian, Y. Li, D.T. Oldfield, P. Kingshott, D.M. Zhu, C. Wen, Quantitative Analyses of MWCNT-Ti Powder Mixtures using Raman Spectroscopy: The Influence of Milling Parameters on Nanostructural Evolution, Adv Eng Mater. 17 (2015) 1660–1669. https://doi.org/10.1002/adem.201500142.

[132] A.J. Bard, L.R. Faulkner, Electrochemical methods: fundamentals and applications, 2nd ed., John Wiley & Sons Inc, New York, 2001.

[133] S. Duan, Y. Zhao, S. Jiang, Z. Yang, Y. Ju, C. Chen, L. Huang, F. Chen, Potential of zero charge regulating highly selective removal of nitrate anions through capacitive deionization, Chemical Engineering Journal. 442 (2022) 136287. https://doi.org/10.1016/j.cej.2022.136287.

[134] J. Lee, P. Srimuk, S. Carpier, J. Choi, R.L. Zornitta, C. Kim, M. Aslan, V. Presser, Confined Redox Reactions of Iodide in Carbon Nanopores for Fast and Energy-Efficient Desalination of Brackish Water and Seawater, ChemSusChem. 11 (2018) 3460–3472. https://doi.org/10.1002/cssc.201801538.

[135] K.L. Martínez-Mendoza, J.M. Barraza-Burgos, N. Marriaga-Cabrales, F. Machuca-Martinez, M. Barajas, M. Romero, Production and characterization of activated carbon from coal for gold adsorption in cyanide solutions, Ingenieria e Investigacion. 40 (2020) 34–44. https://doi.org/10.15446/ing.investig.v40n1.80126.

[136] E. Danso-Boateng, A.B. Ross, T. Mariner, J. Hammerton, M. Fitzsimmons, Hydrochars produced by hydrothermal carbonisation of seaweed, coconut shell and oak: effect of processing temperature on physicochemical adsorbent characteristics, SN Appl Sci. 4 (2022). https://doi.org/10.1007/s42452-022-05085-x.

[137] E. Rodriguez Acevedo, C.A. Franco, F. Carrasco-Marín, A.F. Pérez-Cadenas, F.B. Cortés, Biomass-Derived Carbon Molecular Sieves Applied to an Enhanced Carbon Capture and Storage Process (e-CCS) for Flue Gas Streams in Shallow Reservoirs, Nanomaterials. 10 (2020) 980.

[138] J. Zhao, Y. Yin, Y. Li, W. Chen, B. Liu, Synthesis and characterization of mesoporous zeolite Y by using block copolymers as templates, Chemical Engineering Journal. 284 (2016) 405–411.

[139] M.R. Barr, L. Forster, C. D'Agostino, R. Volpe, Alkaline pretreatment of walnut shells increases pore surface hydrophilicity of derived biochars, Appl Surf Sci. 571 (2022) 151253. https://doi.org/10.1016/j.apsusc.2021.151253.

[140] M.R. Barr, R. Jervis, Y. Zhang, A.J. Bodey, C. Rau, P.R. Shearing, D.J.L. Brett, M. Titirici, R. Volpe, Towards a mechanistic understanding of particle shrinkage during biomass pyrolysis via synchrotron X-ray microtomography and in-situ radiography, Sci Rep. 11 (2021) 2656. https://doi.org/10.1038/s41598-020-80228-x.

[141] J.L. Figueiredo, M.F.R. Pereira, M.M.A. Freitas, J.J.M. Órfão, Modification of the surface chemistry of activated carbons, Carbon N Y. 37 (1999) 1379–1389. https://doi.org/10.1016/S0008-6223(98)00333-9.

[142] A. John, P.J.P. Yadav, S. Palaniappan, Clean synthesis of 1,8-dioxo-dodecahydroxanthene derivatives catalyzed by polyaniline-p-toluenesulfonate salt in aqueous media, J Mol Catal A Chem. 248 (2006) 121–125. https://doi.org/10.1016/j.molcata.2005.12.017.

[143] A.M.P. Hussain, A. Kumar, Electrochemical synthesis and characterization of chloride doped polyaniline, Bulletin of Materials Science. 26 (2003) 329–334. https://doi.org/10.1007/BF02707455.

[144] R.C. Rathod, V.K. Didolkar, S.S. Umare, B.H. Shambharkar, Synthesis of Processable Polyaniline and its Anticorrosion Performance on 316LN Stainless Steel, Transactions of the Indian Institute of Metals. 64 (2011) 431–438. https://doi.org/10.1007/s12666-011-0099-0.

[145] C.E. Brewer, K. Schmidt-Rohr, J.A. Satrio, R.C. Brown, Characterization of biochar from fast pyrolysis and gasification systems, Environ Prog Sustain Energy. 28 (2009) 386–396. https://doi.org/10.1002/ep.10378.

[146] F.A. Settle, Handbook of instrumental techniques for analytical chemistry, Prentice Hall PTR, Upper Saddle River, New Jersey, USA, 1997.

[147] G. Neetika, K. D., T. S. K., Thermal Behaviour of Chemically Synthesized Polyanilines/Polystyrene Sulphonic Acid Composites, International Journal of Materials and Chemistry. 2 (2012) 79–85. https://doi.org/10.5923/j.ijmc.20120202.07.

[148] S. Kubo, R.J. White, N. Yoshizawa, M. Antonietti, M.-M. Titirici, Ordered Carbohydrate-Derived Porous Carbons, Chemistry of Materials. 23 (2011) 4882–4885. https://doi.org/10.1021/cm2020077.

[149] K. Le Van, T.T. Luong Thi, Activated carbon derived from rice husk by NaOH activation and its application in supercapacitor, Progress in Natural Science: Materials International. 24 (2014) 191–198. https://doi.org/10.1016/j.pnsc.2014.05.012.

[150] T.-H. Liou, S.-J. Wu, Characteristics of microporous/mesoporous carbons prepared from rice husk under base- and acid-treated conditions, J Hazard Mater. 171 (2009) 693–703. https://doi.org/10.1016/j.jhazmat.2009.06.056.

[151] N. Gavrilov, I.A. Pašti, M. Vujković, J. Travas-Sejdic, G. Ćirić-Marjanović, S. V. Mentus, High-performance charge storage by N-containing nanostructured carbon derived from polyaniline, Carbon N Y. 50 (2012) 3915–3927. https://doi.org/10.1016/j.carbon.2012.04.045.

[152] L. Li, E. Liu, J. Li, Y. Yang, H. Shen, Z. Huang, X. Xiang, W. Li, A doped activated carbon prepared from polyaniline for high performance supercapacitors, J Power Sources. 195 (2010) 1516–1521. https://doi.org/10.1016/j.jpowsour.2009.09.016.

[153] Z. Zhang, Z. Zhou, H. Peng, Y. Qin, G. Li, Nitrogen- and oxygen-containing hierarchical porous carbon frameworks for high-performance supercapacitors, Electrochim Acta. 134 (2014) 471–477. https://doi.org/10.1016/j.electacta.2014.04.107.

[154] L. Wei, G. Yushin, Nanostructured activated carbons from natural precursors for electrical double layer capacitors, Nano Energy. 1 (2012) 552–565. https://doi.org/10.1016/j.nanoen.2012.05.002.

[155] R.C. Bansal, M. Goyal, Activated Carbon Adsorption, CRC Press, 2005. https://doi.org/10.1201/9781420028812.

[156] J. Li, B. Ji, R. Jiang, P. Zhang, N. Chen, G. Zhang, L. Qu, Hierarchical hole-enhanced 3D graphene assembly for highly efficient capacitive deionization, Carbon N Y. 129 (2018) 95–103. https://doi.org/10.1016/j.carbon.2017.11.095.

[157] C. Macías, P. Lavela, G. Rasines, M.C. Zafra, J.L. Tirado, C.O. Ania, Improved electro-assisted removal of phosphates and nitrates using mesoporous carbon aerogels with controlled porosity, J Appl Electrochem. 44 (2014) 963–976. https://doi.org/10.1007/s10800-014-0705-z.

[158] H. Wang, D. Zhang, T. Yan, X. Wen, J. Zhang, L. Shi, Q. Zhong, Three-dimensional macroporous graphene architectures as high performance electrodes for capacitive deionization, J Mater Chem A Mater. 1 (2013) 11778. https://doi.org/10.1039/c3ta11926b.

[159] A. Sanchez-Sanchez, M.T. Izquierdo, S. Mathieu, J. González-Álvarez, A. Celzard, V. Fierro, Outstanding electrochemical performance of highly N- and O-doped carbons

derived from pine tannin, Green Chemistry. 19 (2017) 2653–2665. https://doi.org/10.1039/C7GC00491E.

[160] M. Thommes, K. Kaneko, A. V. Neimark, J.P. Olivier, F. Rodriguez-Reinoso, J. Rouquerol, K.S.W. Sing, Physisorption of gases, with special reference to the evaluation of surface area and pore size distribution (IUPAC Technical Report), Pure and Applied Chemistry. 87 (2015) 1051–1069. https://doi.org/10.1515/pac-2014-1117.

[161] C.W. Purnomo, C. Salim, H. Hinode, Effect of the activation method on the properties and adsorption behavior of bagasse fly ash-based activated carbon, Fuel Processing Technology. 102 (2012) 132–139. https://doi.org/10.1016/j.fuproc.2012.04.037.

[162] S.-H. Jung, J.-S. Kim, Production of biochars by intermediate pyrolysis and activated carbons from oak by three activation methods using CO2, J Anal Appl Pyrolysis. 107 (2014) 116–122. https://doi.org/10.1016/j.jaap.2014.02.011.

[163] S. Guo, J. Peng, W. Li, K. Yang, L. Zhang, S. Zhang, H. Xia, Effects of CO2 activation on porous structures of coconut shell-based activated carbons, Appl Surf Sci. 255 (2009) 8443–8449. https://doi.org/10.1016/j.apsusc.2009.05.150.

[164] A.M. Dehkhoda, E. Gyenge, N. Ellis, A novel method to tailor the porous structure of KOH-activated biochar and its application in capacitive deionization and energy storage, Biomass Bioenergy. 87 (2016) 107–121. https://doi.org/10.1016/j.biombioe.2016.02.023.

[165] J. Kang, J. Min, S.-I. Kim, S.-W. Kim, J.-H. Jang, Three-level micro–meso–macroporous three-dimensional graphene for highly fast capacitive deionization, Mater Today Energy. 18 (2020) 100502. https://doi.org/10.1016/j.mtener.2020.100502.

[166] A. Tolosa, B. Krüner, S. Fleischmann, N. Jäckel, M. Zeiger, M. Aslan, I. Grobelsek, V. Presser, Niobium carbide nanofibers as a versatile precursor for high power supercapacitor and high energy battery electrodes, J Mater Chem A Mater. 4 (2016) 16003–16016. https://doi.org/10.1039/C6TA06224E.

[167] B. Karamanova, A. Stoyanova, M. Shipochka, C. Girginov, R. Stoyanova, On the cycling stability of biomass-derived carbons as electrodes in supercapacitors, J Alloys Compd. 803 (2019) 882–890. https://doi.org/10.1016/j.jallcom.2019.06.334.

[168] L. Forster, M. Lutecki, H. Fordsmand, L. Yu, C. D'Agostino, Tailoring morphology of hierarchical catalysts for tuning pore diffusion behaviour: a rational guideline exploiting bench-top pulsed-field gradient (PFG) nuclear magnetic resonance (NMR), Mol Syst Des Eng. 5 (2020) 1193–1204. https://doi.org/10.1039/D0ME00036A.

[169] M.A. Isaacs, N. Robinson, B. Barbero, L.J. Durndell, J.C. Manayil, C.M.A. Parlett, C. D'Agostino, K. Wilson, A.F. Lee, Unravelling mass transport in hierarchically porous catalysts, J Mater Chem A Mater. 7 (2019) 11814–11825. https://doi.org/10.1039/C9TA01867K.

[170] J.-H. Choi, D.-J. Yoon, A stable operation method for membrane capacitive deionization systems without electrode reactions at high cell potentials, Water Res. 157 (2019) 167–174. https://doi.org/10.1016/j.watres.2019.03.083.

[171] Y.-A. Chen, C.-S. Fan, C.-H. Hou, Optimizing the energetic performance of capacitive deionization devices with unipolar and bipolar connections under constant current charging, J Taiwan Inst Chem Eng. 93 (2018) 201–210. https://doi.org/10.1016/j.jtice.2018.06.039.

[172] G.-X. Li, P.-X. Hou, S.-Y. Zhao, C. Liu, H.-M. Cheng, A flexible cotton-derived carbon sponge for high-performance capacitive deionization, Carbon N Y. 101 (2016) 1–8. https://doi.org/10.1016/j.carbon.2015.12.095.

[173] J. Kang, T. Kim, K. Jo, J. Yoon, Comparison of salt adsorption capacity and energy consumption between constant current and constant voltage operation in capacitive

deionization, Desalination. 352 (2014) 52–57. https://doi.org/10.1016/j.desal.2014.08.009.

[174] J.H. Choi, D.J. Yoon, A stable operation method for membrane capacitive deionization systems without electrode reactions at high cell potentials, Water Res. 157 (2019) 167–174. https://doi.org/10.1016/j.watres.2019.03.083.

[175] J. Nordstrand, At the Mountains of Modeling: Multiscale Simulations of Desalination by Capacitive Deionization , KTH Royal Institute of Technology, 2022.

APPENDIX
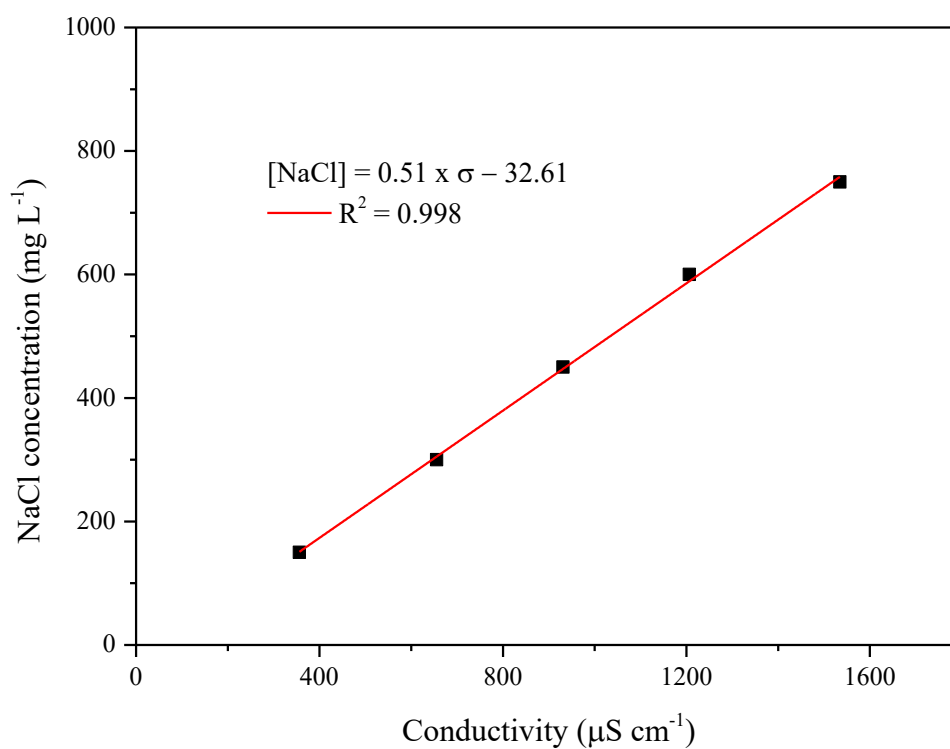
Figure A1. Analytical curve used to calculate NaCl concentration as a function of conductivity. The red line represents the linear fit of the data.